Synthesis of Metal Nanoparticles by Transferred Arc Discharge

Von der Fakultät für Ingenieurwissenschaften,
Abteilung Elektrotechnik und Informationstechnik
der Universität Duisburg-Essen

zur Erlangung des akademischen Grades

Doktor der Ingenieurwissenschaften

genehmigte Dissertation

von

Matthias Stein

aus

Mülheim an der Ruhr

1. Gutachter: Prof. Dr.-Ing. Einar Kruis
2. Gutachter: Prof. Dr. Andreas Schmidt-Ott
Tag der mündlichen Prüfung: 21.09.2015

"What I want to talk about is the problem of manipulating and controlling things on a small scale. As soon as I mention this, people tell me about miniaturization, and how far it has progressed today. They tell me about electric motors that are the size of the nail on your small finger. And there is a device on the market, they tell me, by which you can write the Lord's Prayer on the head of a pin. But that's nothing; that's the most primitive, halting step in the direction I intend to discuss. It is a staggeringly small world that is below. In the year 2000, when they look back at this age, they will wonder why it was not until the year 1960 that anybody began seriously to move in this direction. Why cannot we write the entire 24 volumes of the Encyclopedia Brittanica on the head of a pin? "

Richard P. Feynman

Preface

This thesis is the result of an amazing and very instructive research time I had during the period between 2011 and 2015 at the Institute of Technology for Nanostructures (NST) of the University of Duisburg-Essen. My work during this time has been part of the European project "BUONAPART-E" . It has received funding from the European Union's Seventh Framework Program under grant agreement No: 280765. I greatly enjoyed the challenge and tasks of this project, the collaboration with researchers all over Europe on different topics, the fruitful discussions with all the partners and the interesting and instructive journeys to conferences as well as research visits.

The very first I want to express my deepest gratitude to professor Einar Kruis, who gave me the opportunity to work in his group. His persistent support and broad scientific experience made my research work possible. He highly contributed to the outcome of this work. Thank you for the fruitful discussions, the trust and the scientific freedom you showed me.

I want to thank professor Roland Schmechel for the help in experimental or theoretical questions, chapter corrections, discussions and for his support in his function as head of the institute.

I thank Anssi Arffman from the University of Tampere for the CFD model of the OSU, on which my particle formation model bases and Maria Messing from the University of Lund for all the high resolution TEM images.

I wish to thank all the people of the NST, who made the time here highly enjoyable and supported me during this work. Especially Dennis Kiesler, who gave me essential support with his expertize in all kinds of technical questions. This thesis would not have been possible without Felix Bensel and Christoph Kleinert, who helped me setting up the production facility and assembling an apparently endless number of vacuum clamps.

I appreciated the collaboration with the group of Hartmut Wiggers, who welcomed me and the production facility in their lab. I also want to thank the workshops of the university for manufacturing the technical devices, even on short notice.

Furthermore, I appreciated working with many students, who all contributed to this work: Jeremias Geiss, Mohammed Bishady, Janis Heldmann, Matthias Masuhr, Yannick Beckmann, David Pawlak and Mustafa Demir.

Finally I want to express my heartiest gratitude to my parents Ute and Wolfgang Stein, my family, friends and of course Tanja, who always support me.

Abstract

Metal nanoparticles are already used in various applications and products, with rising tendency. Scaled-up production facilities are needed to answer the demand of the industry, but are very challenging to realize. A production process should generally be energy efficient and sustainable, however the production of metal nanoparticles requires further attributes. In order to produce pure metal nanoparticles, the process needs to be free from oxygen. Also, it has to be ensured that the mass output of nanoparticles is scaled up without increasing the particle size. Detailed information about particle formation and dedicated measurement systems are of importance.

This work reports about the development of a scaled-up production facility of pure metal nanoparticles. The scale-up approach is the parallelization of multiple transferred arcs. The basic idea is thereby, to first optimize the particle formation of a single transferred arc process (lab-scale) in terms of production rate, particle size and electricity consumption and then use it in parallel (production facility), in order to multiply the production rate and minimize the energy consumption. Optimization of the lab-scale process is achieved by adjusting the electrode and gas flow adjustment or by varying the carrier gas composition. The influence of the carrier gas composition on production rate, specific electricity consumption and particle size is investigated. Furthermore, the influence of gas flow and power input are investigated. Optimal process parameters for metal nanoparticle synthesis by transferred arc discharge are found. Long-term production is achieved by the development and adaption of a suitable feeding mechanism. The optimization of the lab-scale process results in an optimal single unit (OSU) for metal nanoparticle production, which is used for the scale-up approach.

A dedicated measurement system based on parallel aerodynamic and mobility diameter measurement with a novel analysis method is applied in order to determine the primary particle size of the synthesized particles online. An equation is found, which allows calculating the mass mobility exponent directly on the basis of the effective density of a particle, hence allowing the direct determination of primary particle size. Also, a thermophoretic proximity sampler is used to determine the particle size evolution during formation. It is found that a thermophoretic proximity sampler can be used to determine particle size evolution in arc discharge synthesis. Particles are successfully sampled at three different characteristic moments during primary particle growth; shortly after nucleation, during common growth processes and when growth of primary particles has already been finished.

In order to understand the particle formation and the influence of different process parameters on the particle size, a simple particle formation model including nucleation, coagulation and sintering is introduced. To include sintering

in the model, specific sintering parameters of the modeled material system are needed. The sintering parameters are determined experimentally by a tandem differential mobility analyzer setup including a sintering furnace. The sintering parameters are obtained by a fitting procedure of the experimental data to a sintering model. The particle formation model including the sintering parameters describes the particle formation accurately.

The production facility applying the scale-up approach is assembled considering intense safety requirements. It contains 16 OSUs in two reactor chambers, each consisting of 8 electrode pairs (mOSU), a gas recirculation system and a filtration unit. The filtration unit is built with a novel, valve-less bagging system. Also, a particle passivation system is added. It is shown that the production rate of the process scales successfully with the number of transferred arcs, while the primary particle size stays constant on the nanoscale. It appears however that the scaled-up process favors the formation of larger agglomerates, which is found not be a result of the residence time, but apparently the increased heat development of the mOSU.

In order to show an application of the produced particles, a copper nanopowder is used to produce a copper ink. The ink is printed on glass substrate by spin or hand coating. It is found that the electrical resistivity is dependent of the printed film thickness, which might be consequence of film inhomogeneities. Applied sintering to the printed films improved the conductivity significantly.

Contents

Chapter 1

Introduction

1.1 General introduction

The quotation at the beginning of this work is part of Richard P. Feynman's famous talk "There's plenty of room at the bottom", which he held at the American Physical Society meeting at Caltech on December 29, 1959. It is often quoted as the starting point of nanotechnology.

Nanotechnology is expected to be one of the key technologies of the century. It is an interdisciplinary technology aiming at applying phenomena of structures in the nanometer range. The field of potential applications is immense and ranges over a broad spectrum of industrial sectors, e.g. from medical applications [111] to the automotive industry [112]. Nanotechnology has the potential to deliver important contributions to solve societal challenges like energy supply, agricultural productivity enhancement or water treatment [25] and has amongst others been chosen by the German federal ministry of education and research as key technology to secure and strengthen Germany as an important technology supplier.

The core of nanotechnology are the nanostructures and their potential to impact basic science and technology. Nanostructures can be subdivided by their dimension. There are 2D nanometer thick layers, 1D nanorods and 0D nanoparticles [55, 62]. This work concentrates on the synthesis of nanoparticles. The synthesis of nanoparticles is generally separated in two production approaches, which are the "Top-down" and the "Bottom-up" approach. Top-down means thereby, to reach a nanostructure by size-reducing a bulk material e.g. by milling [78]. Bottom-up is the formation of nanostructures starting with atoms e.g. by evaporation and condensation processes. Nanoparticles are not only formed synthetically in laboratories, but also in the environment. They are found in ambient air due to combustion (e.g. engines in vehicles, fireplaces, cigarettes), wear-out (e.g. tire wear, construction dust), chemical processes in

the atmosphere and so on [51, 56, 135]. Ambient aerosols are usually residual products and not utilizable or even wanted, as they might have noxious effects on the human body and the environment [9, 58, 88].

Synthetic nanoparticles on the other hand are used in a broad field of applications. Silicon nanoparticles e.g. are used for electronic applications [4,108], titanium dioxide particles are used for photovoltaic or electrochemical [17], zinc oxide particles for thermoelectric applications [44]. Beside semi-conductive or ceramic nanoparticles, especially metal nanoparticles are investigated intensively with the goal to enhance products and applications. They are used in applications ranging from bio-diagnostics [66,97] to catalysis [110]. Silver nanoparticles are e.g. used due to their antibacterial effects [67], copper nanoparticles are used to increase the thermal conductivity of nanofluids [96], nickel particles are used for catalytic purposes [76]. The field of application for metal nanoparticles is enormous. All these applications and products base on metal nanoparticles with a specific particle size. The demand for those particles is rapidly increasing.

The production of pure metal nanoparticles on a larger scale is however very challenging. The general problem of nanoparticle production up-scaling is that the desired particle properties found on a smaller scale can not be conserved after scaling up. The production of metal nanoparticles needs furthermore to be oxygen free. Hence, well developed nanoparticle production facilities e.g. flame reactors [162], cannot be used for metal nanoparticles, at least not without the usage of reactive additives. The usage of those additives is often avoided by the industry due to their hazardous potential. The current state of the art does not offer a method to produce pure metal nanoparticles on larger scale in terms of mass in an economic and sustainable way.

1.2 Nanometals

In this study a particle synthesis setup is developed, which can be used to form particles of various material systems. However, the focus has been laid on the fabrication of metal nanoparticles, namely gold, silver, copper, zinc, chrome iron and aluminum. These materials have been chosen due to the expectation to improve attributes or the performance of specific products or processes.

Noble metal nanoparticles such as gold and silver have a rich history in science [36]. They have already been used for centuries. The Lycurgus cup (figure 1.1) is the oldest known example, in which colloidal gold and silver nanoparticles have been used to color glass due to the dichroic effect, most probably not on purpose. The green cup changes its color to a glowing red depending on the direction of the light source. Nowadays, both metals are applied in a broad field of applications, e.g. for medical or electrical purposes [27, 126]. But also the other metals mentioned above are used widely in the

Figure 1.1: *Lycurgus cup in the British Museum [91]*

fields of electronics, medicine, catalysis etc. Caution is needed when working with these metals due to their strong tendency of oxidization. The goal of this study is to produce metals and not metal oxides, so that only a thin metal-oxide layer protects the metal core.

Metal nanoparticles produced during this thesis have been used for specific products and processes. Copper nanoparticles e.g. are used by a steel manufacturer to improve the cooling of a blast furnace. The particles are known to increase the thermal conductivity significantly [30]. Gold particles are used to produce GaAs nanowires in the gas phase, which can be used for solar cells [55]. Silver particles are used to produce textiles with antimicrobial attributes, without changing other properties like color etc. Nickel particles are used to enhance catalytic membrane reactor performance.

1.3 Arc discharge synthesis

The electric arc is a very important discovery, which is used in a large number of applications from light source, over welding to nanoparticle production. The importance of this invention becomes clear, when one notices that researchers still discuss, whom to credit for this invention [3]. Humphry Davy [28] as well as Vasilli Petrov [122] discovered independently arc discharges in the early 19th century, while working on new powerful batteries. However, Petrov was proba-

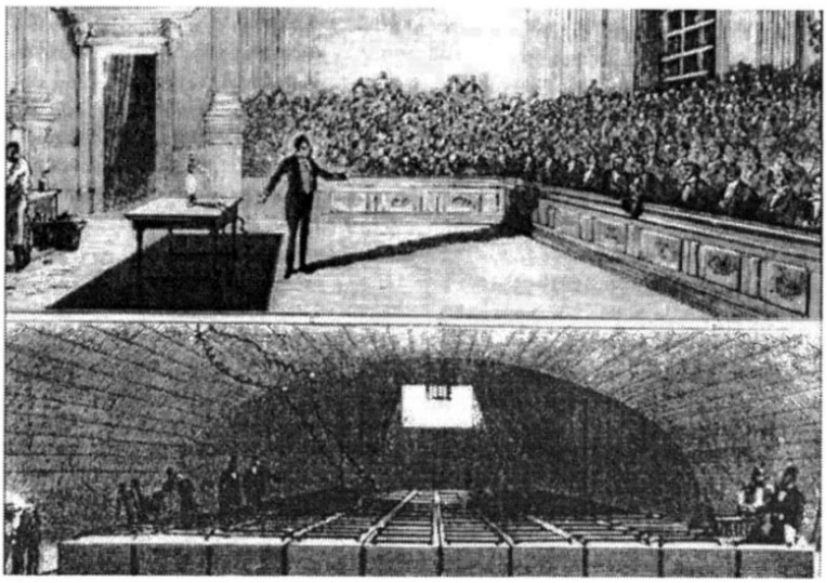

Figure 1.2: *Demonstration of a carbon arc discharge probably by Davy [3]*

bly the first to describe the continuous electric arc, by separating carbon electrodes, to which a high current was applied:

"If two or three charcoal pieces are placed on a glass plate or on a bench with glass legs, and if the charcoal is connected to both ends of an enormous battery using metallic but isolated conductors, and if the two pieces are brought in close distance of one to three lines (2.5–7.5 mm), then a very bright cloud of light or flame shines, burning the charcoal more or less fast, and one may illuminate a dark room as bright as one wants to." [122] [3].

The discovery of the arc with its bright light must have been imposing at that time, there are several pictorial records of Davy presenting an arc to an audience (Figure 1.2). The bright light of the arc is depicted by the large shadow of the man (probably Davy). The figure also depicts the huge battery (Cu-Zn) in the basement, which has been used to ignite the arc. Andres estimated the power of the battery to roughly 3000 W [3], which is in the range of modern power supplies used for arc ignition today. The invention of the arc has eventually led to first applications, e.g. the first electrical lamps (Figure 1.3).

Figure 1.3: *Arc-lamp of the lighthouse of South Foreland close to Dover in 1858 [8]*

The name "arc" results from the shape it adopts between two horizontal arranged electrodes due to buoyancy. The arc discharge occurs, when a high current applied between two electrodes forms a plasma in between them. The plasma, a highly ionized gas, is formed, when the energy given by the current is high enough to ionize and dissociate the gas atoms (or molecules). The amount of energy depends mostly on the gas and its ionization energy (also dissociation energy for molecular gases). But also other factors such as the gap distance, shape and material (work of emission) of the electrodes matter. The arc discharge is a self-preserving discharge, as the electric current maintains the arc stable as long as the parameters mentioned above do not change significantly. The electric arc is usually classified as an arc discharge due to a relatively high current (10-200 A), but low voltage (5-30 V) [127]. The voltage between cathode and anode however differs especially in small space charge regions in front of the electrodes, which is called cathode or anode drop. The cathode drop favors a field emission, which in combination with the more relevant thermionic emission leads to the release of electrons from the cathode, if the work function of the cathode's material is exceeded. The thermionic emission of the cathode bases on the heating of the cathode due to the heat of the plasma, the collision of ions which are accelerated by the cathode drop and the heat due to the recombination of ions and electrodes in front of the cathode. The work function of the cathode (usually tungsten) is additionally decreased by doping with a

rare-earth oxide. Hence, due to the emission of electrons a current is formed between the electrodes, which eventually results in an arc plasma.

Arc plasmas can be classified by their electron density and temperature [151]. The electron density is rather high ($> 10^{21}\mathrm{m}^{-3}$). Overall however, the arc plasma can be seen as electrically quasi-neutral. The electric arc is classified as a thermal plasma as the electron temperature is similar to the one of the ions in the plasma. Temperatures of up to 25000 K have been measured. The temperature depends thereby on the applied electric current, the gas atmosphere, electrode shape, etc. The anode temperature is usually higher than the cathode temperature, which is a result of the nascent work-function of the electrons, when they enter the anode.

Due to its high thermal energy, the electric arc can be used to produce nanoparticles in different ways (see chapter 2). In this study the energy of the arc is used to evaporate the anode and form particles from the anode vapor. Since the anode is the consumed electrode, it has to consist of at least two different materials. First, the feedstock material which is to be evaporated. Second, since this material probably melts during the synthesis procedure, a carrier or crucible is needed. This crucible can be formed out of graphite, which has a high sublimation temperature, while being a good electric conductor. Due to this "two material" anode, conductive feedstock material can be evaporated, when the arc strikes directly on the material (transferred arc, direct heating). But also non conductive materials can be evaporated, when the arc strikes the crucible and indirectly heats the feedstock material. The nanoparticles created by this method consist principally of the feedstock material, however more complex material composition can easily be formed by using different reactive process gases, e.g. aluminium nitride particles can be formed by evaporating aluminium in a nitrogen plasma.

Figure 1.4 shows an example of one of the arrangements of the two electrodes, as used during this thesis. The tungsten rod cathode is coming from the side. The crucible anode has been manufactured in a way, that it does not only serve as a melt carrier, but also a guidance for the gas flow out of the reactor.

An electric arc is usually ignited by contact ignition or high frequency ignition. In contact ignition the two electrodes are brought together and a high current is applied. When the electrodes are removed with the applied current an arc is formed. This procedure however is not very applicable for the arc synthesis. Practically the disconnection of the two electrodes has to be done very fast to prevent a weld, which is difficult to do through the vacuum connections such a process is typically performed through. Also impurities can result from the contact ignition. An arc results from the high frequency ignition when a breakdown between the electrodes created by a high voltage (>20 kV) is maintained by a high current. This method is easy to perform when the electrodes

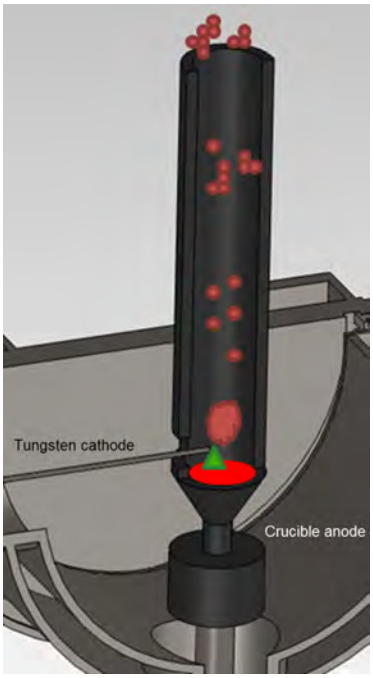

Figure 1.4: *Example of electrode arrangement as used during this work*

are brought at close distance. Most of the commercially available welding machines provide this ignition mode. Anode impurities are expected to be minor due to the very short duration of the ignition spark.

A large amount of work has been done to describe and model electric arcs, its formation and use of applications [34, 38, 48, 52, 114].

1.4 This work

This work describes the development of a production process for metal nanoparticles in the order of kilograms per day based on arc discharge synthesis. It contains the development and optimization of the synthesis process as well as appropriate methods of process validation and product characterization. Figure 1.5 depicts the structure of this work and the connections between the single chapters.

In chapter 2 a state of the art is given including previous research on arc discharge synthesis. Fundamentals of arc discharge and gas phase synthesis of metal nanoparticles are discussed and an overview over the characterization and measurement techniques used in this study is given in chapter 3. In chapter 4, the basic process used to form metal nanoparticles in this work is described: the transferred arc synthesis. The general setup is described and in the following optimized in terms of particle properties, production rate and energy

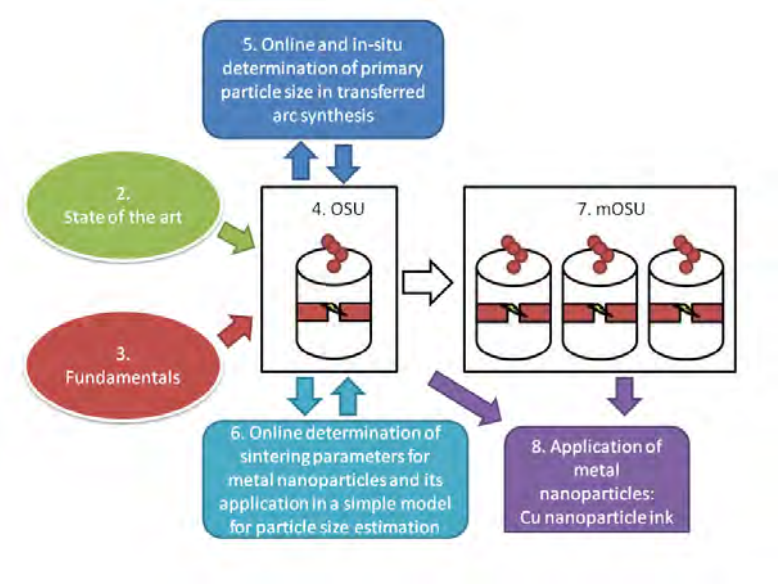

Figure 1.5: *Structure of this work*

consumption. All the development and optimization done on this "single electrode" process results in an "optimized single unit" (OSU). A novel measurement procedure to determine primary particle sizes online in the gas phase formed by the OSU is presented in chapter 5. This chapter discusses also the ex-situ sampling of particles during growth inside the reactor by a thermophoretic proximity sampler. In order to understand the formation of nanoparticles in the arc process, a simple model is used to estimate primary particle sizes and extent of agglomeration. The model is described in chapter 6 together with an experimental approach to determine the sintering parameters of metals online via a tandem-DMA (Differential Mobility Analyzer) setup. The sintering parameters of the metals are required for the model, but are also relevant for other studies. The OSU is used in the following to scale up the production rate of metal nanoparticles further, by the parallelization of multiple OSUs. Eight OSUs are placed in a single reactor housing (multiple OSU (mOSU)). The use of many single production units in parallel, which have been thoroughly optimized and tested on a lab-scale for a given metal, ensures that a highly effective scale-up of the synthesis process in terms of cost and energy consumption is possible. Further equipment, such as pumps and filters, are scaled up as single units leading to additional cost benefits. The development of the production facility and its description containing the mOSU, filtration unit, gas recirculation, etc. is presented in chapter 7. Chapter 8 shows an application of particles produced by the developed process, as copper nanoparticles are used to prepare a conductive nanoink.

Chapter 2

State of the art in arc discharge synthesis

Excerpts of this chapter have been published [145, 146]. The interest in pure metal nanoparticles has increased significantly over the past years, as well as their number of applications. Due to their characteristic attributes, metal nanoparticles are used in e.g. optoelectronic applications, medicine, sensor technology, information storage and catalysis [36]. The increasing demand from the industry for metal particles therefore challenges scientists and engineers around the world to develop processes, which are easily scalable and produce a product with adequate purity. Numerous methods to synthesize metal nanoparticles are known, but especially plasma synthesis has the potential to produce high-quality nanoparticles economically and in large quantities.

The term plasma synthesis comprises a great variety of processes and applications, which differ already in their approach. Figure 2.1 depicts a classification of plasma synthesis processes. Generally one can divide plasmas into thermal plasmas (in Local Thermal Equilibrium, LTE) and non-thermal plasmas (not in LTE), based on the temperature ratio between electrons and ions as well as their number densities [47, 151]. Both systems are widely used to produce nanoparticles. Non-thermal plasma synthesis has been used e.g. by Kortshagen [84] or Mariotti and Sankaran [104]. But especially in terms of the process economy of scaling-up, thermal plasmas appear more promising.

Thermal plasmas have been studied intensively [34, 52, 123, 151]. They are used under atmospheric or reduced pressure to produce nanoparticles and can be subdivided into radio-frequency (RF) plasmas [10, 80], thermal microwave plasmas [11, 121, 156], spark discharges [131, 148, 161], glow discharges [60] or DC discharges. DC discharges are used in non-transferred arc processes also known as plasma jets or plasma sprays [33, 41, 53, 138, 140] or in transferred

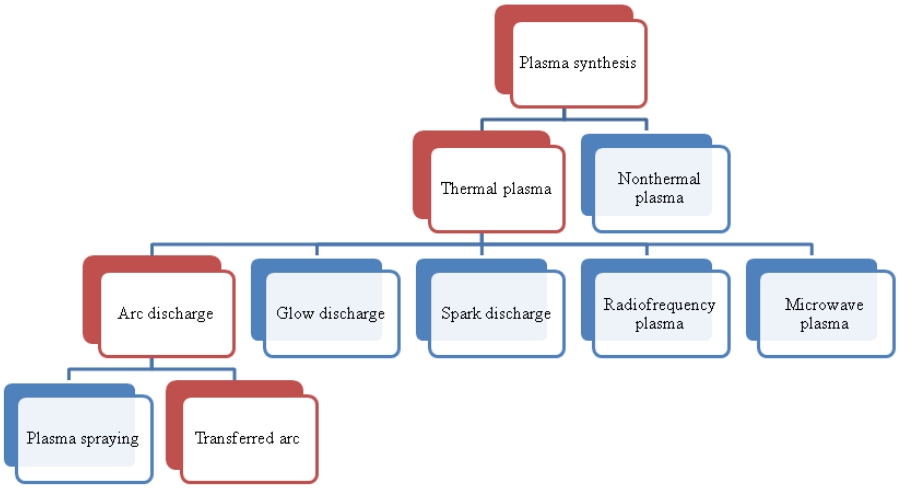

Figure 2.1: *Classification of plasma synthesis*

arc processes [16, 101], where the direct striking of the arc on the anode is fundamental.

However, only few plasma synthesis methods are suitable for scaling-up the production rate. Some processes have a low energy efficiency, demand a too large investment or are unsuitable simply because the produced particles are not any more nanoscaled when increasing the production rate. A promising method to increase the production rate of metal nanoparticles economically is the transferred arc synthesis. Mahoney et al. [101,102] have developed a transferred arc process synthesizing nanoparticles of metals, metal oxides, nitrides or carbides. The material evaporation is realized by arc evaporation, which is ignited by contacting of the electrodes and separating them to an arc gap of approximately 0.5 cm. It is found that the evaporation rate can be controlled by the applied current (10 A - 70 A), which on the other hand affects the voltage (8 V - 13 V) and thereby the energy input. Evaporation rates up to 50 g/h are reported, but no actual production rates presented. In this study, evaporation rates are referred to as the mass amount of material per time, which is given into the formation process (into the gas phase) and production rate as the mass amount of product which results at the end of the process. Depending on the gas flow rate in the arc- and quench region, particle sizes of 1 to 100 nm have been achieved. Chen et al. [16] have presented a simple and versatile mini-arc plasma source for nanocrystal synthesis. The arc is ignited by contact between a tungsten cathode and a graphite crucible anode via a commercial TIG welder. Due to the design of the crucible, the arc parameters (power etc.) are independent from the feedstock material. At an electrode distance of 0.5 mm, the arc is fed by 30 to 40 A at approximately 3 V. Silver nanoparticles of up to 60

nm with a mass production rate of up to 10 mg/h were synthesized. Celik et al. [14] have described a transferred arc method for the production of ultra-fine powder of any conductive material, such as metals, alloys, etc. They achieved a process with high evaporation rates (0.5 kg/h) to synthesize pure particles mostly of 1 µm. While the production rate of particles is not mentioned, a novel cooling process is developed to control the particle growth, reduce particle losses and increase the production efficiency. Wei et al. [163] have generated copper nanoparticles by a transferred arc process, which shows high purity, single phase and spherical shape. Haidar [49] has used a transferred arc to produce aluminum and aluminum oxide nanoparticles in a low pressure system. Cole et al. [24] have synthesized positively charged gold or zinc oxide nanoparticles by arc discharge to build well-positioned three-dimensional nanostructures. Uda et al. [152] have increased the production rate of fine metal particles via transferred arc by adding hydrogen to the carrier gas (argon). Among others, silver and aluminium particles smaller than 1 µm are synthesized by using 25 vol.% hydrogen and 75 vol.% argon as carrier gas. With an energy input of ca. 4500 W, 0.04 g/h aluminium and 42 g/h silver are generated. Förster et al. [39] have presented an experimental study on the production of copper nanoparticles with a transferred arc. In a slightly sub-atmospheric argon system, a 70 to 120 A transferred arc is ignited between a tungsten rod cathode and a graphite crucible anode, filled with copper to be evaporated. Copper particles in the size range of 4 to 50 nm are synthesized, depending on arc current, arc length, gas flows and hydrogen addition to the sheath gas. Especially the stability of the process over 8 hours is notable.

Table 2.1 summarizes the applied power, evaporation rate and particle size of particles produced by the transferred arc method for different metals (data from literature). Actual production rates from an arc synthesis process are almost not existing in the literature. As presented, the evaporation rates differ strongly for each metal and the applied power. The vapor pressure of the material plays a key role in the evaporation process, as of course does the applied power. It can be assumed that independent from the material a higher power input leads to higher evaporation rate and bigger particles. A scale-up of evaporation rate by increasing the input power is hence not applicable.

Beside the experimental investigations, a lot of modeling efforts have been directed towards the understanding of different process parameters. Especially the following publications have helped to understand the influence of different parameters on the arc and accordingly the production rate, which is one of the main goals of this work. Murphy et al. [116] have investigated the influence of the gas composition in TIG welding. It is found that adding hydrogen, nitrogen or helium to argon leads to an increase in the heat flux density to the anode and therefore the weld pool depth and size. The temperature increase

Table 2.1: *Applied power, evaporation rate and particle size of particles produced by the transferred arc method for different metals*

Material	Power (W)	Evap. Rate (g/h)	d_P(nm)
Ag [16]	< 120	> 0.01	60
Al [152]	< 3600	0.04	< 1000
Cu [14, 39, 142, 163]	24500	1000	< 1000
	< 1300	0.6	4-50
	13500	-	< 200
	-	-	67
Fe [152]	< 3600	17	< 1000
In [101]	< 500	30	1-100

is explained by the greater arc constriction due to the thermal pinch effect and also by the increase of the thermal conductivity. Lim et al. [93] have shown that the removal of impurities in copper by plasma arc melting is improved when adding 20 vol.% hydrogen to argon. This is explained by an increased surface temperature of the copper, because of the hydrogen presence. Ramirez-Argaez et al. [128] have performed mathematical modeling to study the influence of different gases on high-intensity electric arcs. It is shown that nitrogen has a high arc power, because of its small electric conductivity and hence increased electric resistance. It is observed to be almost the opposite for argon arcs, where the good electric conductivity leads to low power arcs. A review of the effects of metal vapor in arc welding is given by Murphy [115]. It is concluded that even low metal concentrations strongly affect two thermophysical properties: the net radiative emission coefficient and the electrical conductivity. Generally, the presence of metal vapor increases the electrical conductivity, the current density and thereby the heat flux density of the plasma. Metal vapor also increases the radiative emission coefficient across the full range of temperatures in the arc, which leads to a cooling of this region. Both effects lead to a decrease in the arc temperature. Furukawa et al. [43] have investigated the effect of copper vapor on the heat transfer in a nitrogen plasma. The heat transfer, generally caused by convection, impact electrons on the anode and radiation is found to decrease with increasing concentration of metal vapor. Their simulations show that the metal vapor increases the electrical conductivity in the plasma and therefore decreases the thermal conductivity and temperature of the plasma. The heating efficiency of a molten anode is 20% smaller than that of a solid anode. Li et al. [92] have calculated that silver vapor in an arc with air as carrier gas has a stronger cooling effect than copper vapor at the arc center and a clearer restriction effect on the arc motion. Cressault et al. [26] have concluded from their numerical solutions that the low ionization potential of metals modifies the charged particle densities of the plasma composition and therefore increases

the electrical conductivity and net emission coefficient. Copper and silver show almost the same influence.

As the state of the art shows, a lot of work has been done to understand the transferred arc synthesis. The literature data indicates that this synthesis method is suitable for the large scale synthesis of metal nanoparticles by the procedure of this study. The next step in this development is to apply this knowledge and build a large-scale production facility of nanoparticles by overcoming engineering problems, such as instability of the process, scale-up or product validation.

Chapter 3

Fundamentals of transferred arc nanoparticle synthesis and nanoparticle characterization

In this chapter, theoretical fundamentals of this thesis are described. It is separated in two parts; the fundamentals about the synthesis of metal nanoparticles by arc discharge and the fundamentals of characterization of the synthesized particles. Since on both topics, the synthesis as well as the characterization of nanoparticles there exists an enormous amount of knowledge and information, here only some major parts, relevant for this thesis are selected and described.

3.1 Synthesis of metal nanopowder by arc discharge

The synthesis of metal nanoparticles by arc discharge bases on the principles of gas phase synthesis: creation of supersaturated vapor, nucleation, condensation, coagulation, agglomeration and sintering. Their detailed discussion would surely go beyond the scope of this thesis. Further information about the formation of nanoparticles in the gas phase can be found in the literature [36, 40, 57].

3.1.1 Nanoparticle formation by arc discharge

The formation of nanoparticles by the transferred arc synthesis bases on the evaporation-condensation method. The feedstock material is evaporated by the thermal arc and forms metal vapor which condenses into nanoparticles, when it reaches a cooler area. Figure 3.1 shows a schematic of the nanoparticle formation process [87]. Monomers (feedstock atoms) nucleate and form particles, which tend to grow further and agglomerate with increasing reaction time. In the

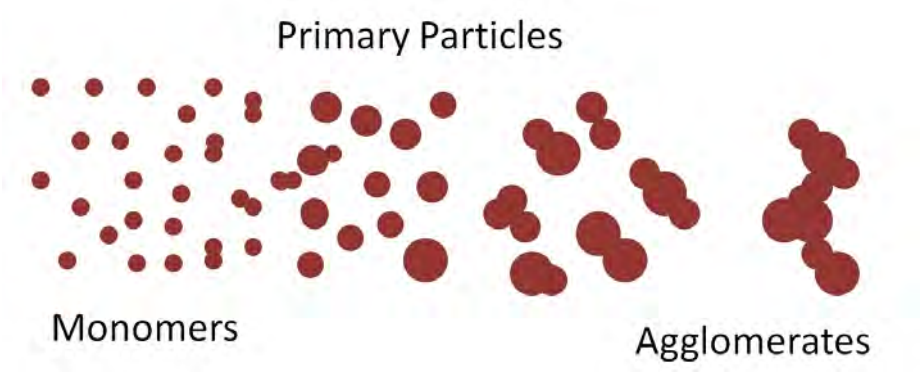

Figure 3.1: *Schematic of a nanoparticle formation process [87]*

following, some equations are given to describe the formation of nanoparticles in the gas phase briefly.

The nanoparticle formation in the gas phase of evaporated material (monomer), e.g. by a transferred arc, is a phase transformation, which is forced by a change of the free energy G of the system. The change of the free energy ΔG is the sum of the change of the free energy due to the formation of a new volume $\Delta G_{\mathrm{V}} = \frac{4}{3}\pi r^3(-kT\ln(S))$ and a new surface $\Delta G_{\mathrm{S}} = 4\pi r^2\sigma$, when a cluster is formed:

$$\Delta G = \Delta G_{\mathrm{V}} + \Delta G_{\mathrm{S}} \tag{3.1}$$

with r the radius of a formed cluster, k the Boltzmann constant, T the temperature, σ the surface tension and $S = \exp(\frac{2\sigma V_m}{rkT})$ the supersaturation ratio (Kelvin relation), with V_{m} being the molar volume.

If $S > 1$, the change of the free energy ΔG has a positive maximum ($\frac{\mathrm{d}\Delta G}{\mathrm{d}r} = 0$) at a critical cluster radius r^*_{n}, which can be understood as the activation energy for nucleation. Cluster with a size larger than r^*_{n} tend to decrease their free energy further and grow to stable particles.

$$r^*_{\mathrm{n}} = \frac{2\sigma V_{\mathrm{m}}}{kT\ln(S)} \tag{3.2}$$

Is a system supersaturated ($S > 1$) and therefore no longer in an equilibrium state of condensation and evaporation, a nucleation rate I for homogeneous nucleation can be derived [40]:

$$I = 2\left[\frac{p_1}{(2\pi M_{\mathrm{m}}kT)^{\frac{1}{2}}}\right](n_1 V_{\mathrm{m}}^{\frac{2}{3}})\left[\frac{\sigma V_{\mathrm{m}}^{\frac{2}{3}}}{kT}\right]^{\frac{1}{2}}\exp\left[\frac{-16\pi\sigma^3 V_{\mathrm{m}}^2}{3(kT)^3(\ln S)^2}\right] \tag{3.3}$$

with p_1 being the partial pressure of the condensing species, M_m the molar mass and n_1 the concentration of monomers.

Are clusters/ particles formed and present in the gas phase, heterogeneous nucleation can occur simultaneously with the homogenous nucleation, but also at lower supersaturation ratios. Heterogeneous nucleation means that the monomers condensate on a solid surface (existing particles) from the gas phase. Hence, the particles grow further due to collisions of particles and condensing species. To describe the growth of the particles ($\frac{\mathrm{d}_v}{\mathrm{d}t}$) (here only transport limited growth) one has to distinguish, if the heterogeneous nucleation appears in the continuum range ($d_\mathrm{p} > \lambda$) (equation 3.4), with λ the mean free path of the gas or in the free molecular range ($d_\mathrm{p} < \lambda$) (equation 3.5).

$$\frac{\mathrm{d}v}{\mathrm{d}t} = \frac{2\pi D d_\mathrm{p} V_\mathrm{m}}{kT}(p_1 - p_\mathrm{d}) \tag{3.4}$$

$$\frac{\mathrm{d}v}{\mathrm{d}t} = \frac{\pi d_\mathrm{p}^2 V_\mathrm{m}(p_1 - p_\mathrm{d})}{(2\pi M_\mathrm{m} kT)^{\frac{1}{2}}} \tag{3.5}$$

D is the diffusion coefficient of the condensing species and p_d the equilibrium vapor pressure above a drop of diameter d_p.

Modeling of the homogeneous nucleation of particles formed in thermal plasma synthesis on basis of the equations shown above indicates rapid formation of clusters and particles due to condensation (Figure 3.2) [46]. It shows the strong temperature dependency of the saturation ratio (Figure 3.2 a) as well as the critical size for stable cluster formation (here k^*) (Figure 3.2 b). The size of the formed particles appear to be strongly dependent on the cooling rate (Figure 3.2 c), which the particles experience due to the carrier gas flow and the monomer concentration (Figure 3.2 d), which depends on the amount of evaporated material due to the transferred arc.

Particles formed by nucleation can coagulate and form agglomerates due to collision. The change of particle number concentration N can be calculated by the following equation [87]:

$$\frac{\mathrm{d}N}{\mathrm{d}t} = -\frac{\beta}{2}N^2 \tag{3.6}$$

in which β expresses the collision frequency between two particles or agglomerates described by a fractal structure, strongly depending on the regime (continuum (equation 3.7) or free molecular (equation 3.8)) the collision takes place in:

$$\beta(v_i, v_j) = \frac{2kT}{3\eta}\left(\frac{1}{v_i^{\frac{1}{D_f}}} + \frac{1}{v_j^{\frac{1}{D_f}}}\right)\left(v_i^{\frac{1}{D_f}} + v_j^{\frac{1}{D_f}}\right) \tag{3.7}$$

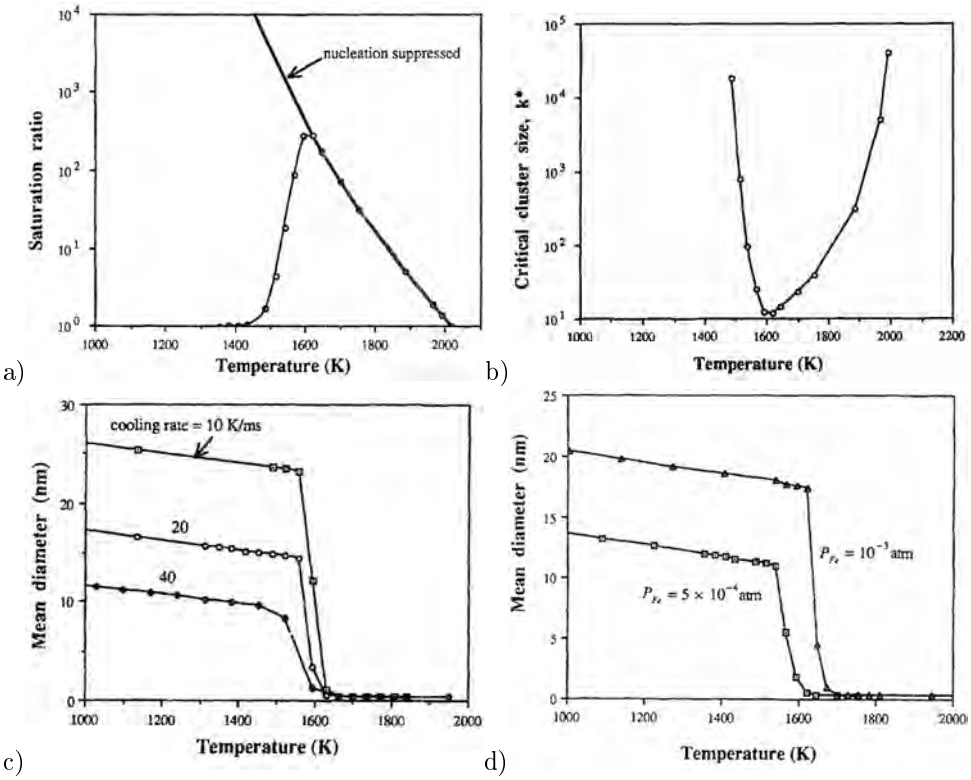

Figure 3.2: *Modeled supersaturation ratio a) and critical cluster size b) depending on temperature as well as calculated mean diameter of formed particles depending on cooling rate (c) and starting monomer concentration (d). Figures taken from Girshick and Chiu with permission of Springer Science + Business Media [46]*

$$\beta(v_i, v_j) = (\frac{3}{4\pi})^{\lambda}(\frac{6kT}{\rho_\mathrm{p}})^{\frac{1}{2}} a_{\mathrm{p}_0}^{2-\frac{6}{D_f}} (\frac{1}{v_i} + \frac{1}{v_j})^{\frac{1}{2}} (v_i^{\frac{1}{D_f}} + v_j^{\frac{1}{D_f}})^2 \tag{3.8}$$

η is the gas viscosity, v_i and v_j the volume of the two colliding particles/ agglomerates and D_f the fractal dimension of the agglomerate. For a spherical particle the fractal dimension D_f is 3 by definition, which simplifies equation 3.8 significantly.

Especially in the highly thermal transferred arc synthesis, it is likely that formed agglomerates sinter partially. Sintering is an irreversible process, in which coalescence and rearrangement of primary particles form an aggregate, finally leading to a compact sphere [117]. The driving force for sintering is considered to be the minimization of surface energy. The change of the surface over time can be calculated by [82]:

$$\frac{\mathrm{d}a}{\mathrm{d}t} = -\frac{1}{\tau_\mathrm{s}}(a - a_\mathrm{f}) \tag{3.9}$$

with a being the surface of the agglomerate, a_f the surface of the completely sintered spherical particle and τ_s the characteristic sintering time depending on an activation energy E_a and a sintering parameter c. The sintering of metal agglomerates especially the determination of E_a and c is part of this study and discussed in chapter 6.2.

3.1.2 Collection of nanoparticles

Particle collection is a major part in nanoparticle synthesis. Whether a powder or dispersion is wanted as a product, particles have to be collected and somehow separated from the gas phase. For nanopowders typically membrane or fibrous filters are used for collection. Samples of the product can also be collected by an impactor or an electrostatic precipitator (ESP). A cyclone can be used to get rid of unwanted larger particles.

Membrane filter consist of complex structures of pore-layers, in which the particles are collected. The efficiency of those filters is typically expressed in a penetration factor P:

$$P = \frac{N_\mathrm{out}}{N_\mathrm{in}} = e^{-\gamma g} \tag{3.10}$$

with N being the number concentration that enter and leave the filter, γ the fraction of particles that are collected in one layer and g the thickness of one layer. The penetration decreases significantly with increasing thickness g.

The penetration or collection factor $(1 - P)$ of particles in a filter medium depends on several processes, e.g. impaction or diffusion. Figure 3.3 depicts the impact of the different collection mechanisms [57]. Depending on the particle size, different kind of collection mechanisms appear, so in total almost all particles are collected. A minimum of the total collection efficiency appears at about 200 nm, where the particles are to big to be collected by diffusion, but too small to be collected by impaction or interception.

For a synthesis process as it is developed in this study, the pressure drop over a filter unit (Δp) is a crucial parameter. An increased pressure drop requires stronger pumps to maintain a stable flow. It is also the parameter to monitor the filter loading. The quality of a filter is hence defined by the collection efficiency per pressure drop [57]:

$$q_\mathrm{f} = \frac{\gamma t}{\Delta p} \tag{3.11}$$

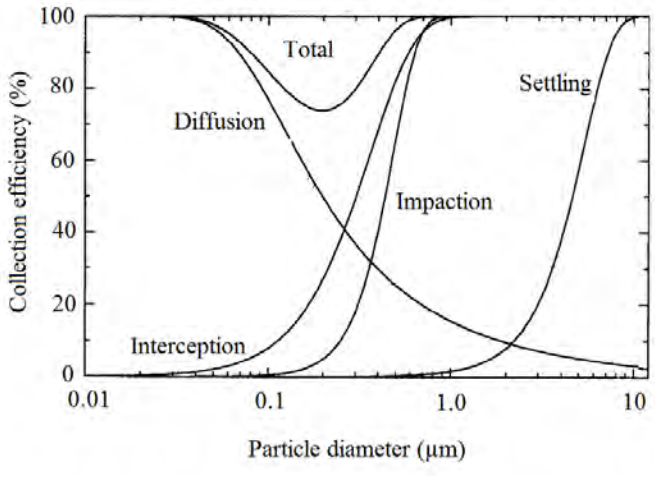

Figure 3.3: *Filter efficiency versus particle size, data taken from Hinds [57]*

3.2 Nanoparticle characterization

Characterization tools are fundamental in process development. The ability to obtain product information from a process is as valuable as the process itself. Especially in the field of nanoparticle synthesis, there are many characterization tools available to measure nanopowders, dispersions, aerosols etc.. In this chapter only a few of those characterization devices are described, which are used in this work. Generally, one can separate the devices used in this work in offline or online characterization devices, whether they obtain product information after synthesis on collected nanopowder (offline) or directly during synthesis in the gas phase (online). A general review of aerosol measurement with further information is e.g. given by McMurry or Hinds [57, 107].

3.2.1 Particle diameter and size statistics

As this thesis discusses a formation process of nanoparticles, a parameter will arise several times, which is the particle size. This parameter however has multiple definitions and depends strongly on the measurement technique and its weighting.

The motion of nanoparticles through the gas is thereby very important to understand the characterization processes described in the upcoming sections. The drag force F_d describes the resisting force a particle experiences by the gas molecules, when moving through the gas [57]. The effect of gas resistance has been investigated first by Newton (on cannonballs), resulting in Newton's law:

$$F_\mathrm{d} = C_\mathrm{d} \frac{\pi}{8} \rho_\mathrm{g} d^2 x^2 \tag{3.12}$$

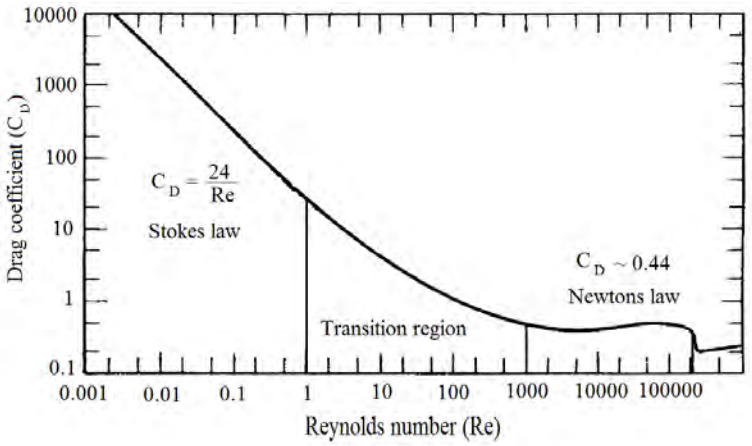

Figure 3.4: *Drag coefficient in dependence of the Reynolds number [57]*

with the drag coefficient C_d, the density of the gas ρ_g, the sphere diameter d, and the velocity of the sphere x. Newton assumed that the drag coefficient is constant for a given shape, which is true however only for Reynolds numbers $Re > 1000$ [57]. As small particles range typically in much smaller Reynolds numbers (viscous forces are increased in comparison to inertial forces), Stokes defined the drag force for small Reynolds numbers by the law:

$$F_\mathrm{d} = 3\pi\eta x d \tag{3.13}$$

Comparing equation 3.12 with equation 3.13 a drag coefficient for small Reynolds number is found to be:

$$C_\mathrm{d} = \frac{24\eta}{\rho_\mathrm{g} x d} = \frac{24}{Re} \tag{3.14}$$

Figure 3.4 depicts the drag coefficient in dependence of the Reynolds number. At high Reynolds number the drag coefficient behaves constant (Newtons law), at smaller Reynolds number it behaves as predicted by Stokes.

To describe the drag force of nanoparticles in more detail, a slip correction factor has to be added to equation 3.13. For small particles the particle size is in the same range as the mean free path λ and the relative velocity of the gas at the particles surface is not zero, as it has been assumed by Stokes. The drag force is overestimated due to the "slip" at the surface and can be corrected by the Cunningham-slip-correction factor $C_c = 1 + \frac{\lambda}{d}(2.34 + 1.05\exp(-0.39\frac{d}{\lambda}))$ [2]:

$$F_\mathrm{d} = \frac{3\pi\eta x d}{C_C} \tag{3.15}$$

All of these equations consider well shaped particles, such as droplets. However in most cases they are not shaped as a sphere, but cubic, cylindrical

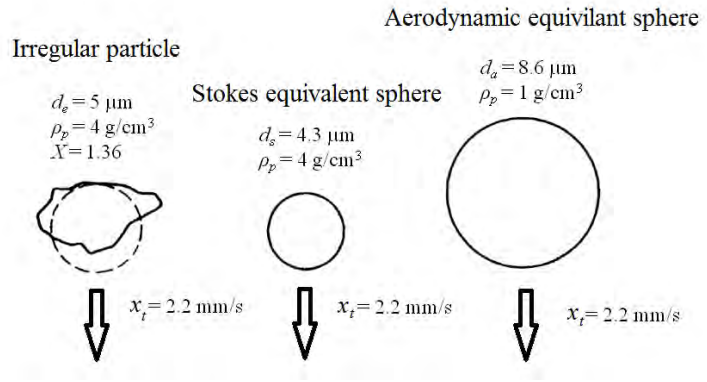

Figure 3.5: *Equivalent diameters in comparison to an irregular shaped particle [57]*

(nanorods) or irregular (unsintered particles or agglomerates). The drag force of such particles differs strongly of the one of a sphere. Hence, a dynamic shape factor X is introduced to correct the Stokes law [57]. X is basically the drag force of a non-spherical particle divided by the drag force of a spherical particle, with the same volume and velocity as the original particle:

$$X = \frac{F_\mathrm{d}}{3\pi\eta d_\mathrm{e} x} \tag{3.16}$$

d_e is called the equivalent diameter. Widely used equivalent diameters to describe irregular shaped particles are e.g. the aerodynamic d_a or Stokes diameter d_S. The aerodynamic diameter is defined as the diameter a spherical particle with the density ρ_0 of 1 g/cm^{-3} would have, while having the same settling velocity x_t as the original particle. The definition of the Stokes diameter is similar, but takes into account the bulk density ρ_b of the material. This relation can be summarized in the settling velocity [57]:

$$x_\mathrm{t} = \frac{\rho_\mathrm{p} d_\mathrm{e}^2 g}{18\eta X} = \frac{\rho_0 d_\mathrm{a}^2 g}{18\eta} = \frac{\rho_\mathrm{b} d_\mathrm{s}^2 g}{18\eta} \tag{3.17}$$

Figure 3.5 illustrates the different equivalent diameters in comparison to an irregular particle shape [57]. As depicted, different equivalent sizes appear for the same particle.

In this thesis also electrical mobility diameters and Sauter diameters (next section) are discussed, which again give different values for the same particle. Combinations of those diameters allow earning additional information about the particle or agglomerate. Nevertheless, the expression particle size has to be used with care.

Usually synthesized particles are not all of the same size (monodisperse), but are distributed (polydisperse). This size behavior is expressed in a particle size distribution, which can be described cumulative or differential and is based on number, surface or volume (mass) equivalent diameters. The size distribution allows calculating a mean diameter, which is generally expressed as [57]:

$$\bar{d}_{q,q-1} = \left(\frac{\sum(N_i d_i^q d_i^p)}{\sum(N_i d_i^q)}\right)^{1/p} \tag{3.18}$$

with N the number and d the diameter. p is the moment average and q the moment distribution, with $q = 0$ for number, 1 for diameter, 2 for surface and 3 for volume/mass ($p > 0$). The surface based mean diameter (or Sauter diameter) is e.g. expressed as:

$$d_{3,2} = \frac{\sum N_i d_i^3}{\sum N_i d_i^2} \tag{3.19}$$

3.2.2 Offline characterization

The offline characterization tools used here are traditional devices such as electron microscopy (SEM, TEM), X-ray diffraction methods (XRD, EDX) or BET measurements [12]. Most of these methods are very common in the nanoparticle community and therefore not described in detail here.

3.2.2.1 X-ray Diffraction

A lot of material information is nowadays obtained by diffraction methods. Usually an incident wave is directed onto a material, where the wave is diffracted and collected by a detector, which moves over the sample to record the directions and intensities of the diffracted wave. The observed material consists of atoms, which are arranged in crystal structures. In order to obtain information about the material, the wavelength needs to be comparable to the spacing between the atoms, e.g X-rays. X-ray waves are scattered at atoms, primarily through their electrons. An X-ray striking an electron produces secondary spherical waves (elastic scattering) emanating from the electron. A regular array of atoms (scatterers), as it is in a crystal, produces a regular array of spherical waves. Although these waves cancel out each other in most directions through destructive interference, they concentrate constructively in a few specific directions, determined by Bragg's law:

$$n \cdot \lambda_1 = 2d_{\mathrm{hkl}} \sin(\theta_{\mathrm{hkl}}) \tag{3.20}$$

, λ_1 is the wavelength of the beam, n any integer, d_{hkl} the spacing between diffracting planes, θ_{hkl} the incident angle. The intensity of the Bragg-reflections of crystalline materials is measured for different incident angles leading to a

diffractogram. The diffractogram is characteristic for the investigated material or composition.

The X-ray diffraction does not only lead to information about the material composition, but also about the crystalline size d_C. This information can be found in the broadening of the reflections in a diffractogram, by the Scherrer equation:

$$d_\mathrm{C} = \frac{K\lambda}{B\cos\theta} \tag{3.21}$$

,with the Scherrer constant K (0.89 at Full Width of Half Maximum (FWHM)) and B the FWHM. Further detailed information about diffractometry methods can be found in the literature [42].

3.2.2.2 Brunauer-Emmett-Teller measurement

The Brunauer-Emmett-Teller (BET) method [12] can be used to estimate the primary particle size of a nanopowder. It bases on the adsorption (attachment) of gas atoms or molecules on a solid surface (particle) due to the van der Waals force (physisorption) [61]. The gas adsorption allows calculating a surface area of nanoparticles, which surface is in comparison to its volume rather large. The BET formula is given by:

$$\frac{P_\mathrm{e}}{V_0(P_0 - P)} = \frac{1}{hV_{0\mathrm{m}}} + \frac{h-1}{hV_{0\mathrm{m}}}\left(\frac{P_\mathrm{e}}{P_0}\right) \tag{3.22}$$

with P_e the equilibrium experimental pressure, P_0 the vapor pressure of the adsorbate gas, V_0 the volume the adsorbed gas per gram of adsorbant, $V_{0\mathrm{m}}$ the volume of the adsorbate monolayer per gram adsorbent and h a constant relating the heat of adsorption and condensation.

Equation 3.22 behaves linearly for $0.05 \leq \frac{P_\mathrm{e}}{P_0} \leq 0.35$, with the slope $\frac{h-1}{hV_{0\mathrm{m}}}$ and the intercept $\frac{1}{hV_{0\mathrm{m}}}$. Figure 3.6 shows an example for a BET isotherm of synthesized copper nanopowder.

The specific surface area can then be calculated by [61]:

$$SSA = a_\mathrm{m} N_A \left(\frac{P_0 V_0}{RT}\right) \tag{3.23}$$

with a_m the area of one adsorbed gas molecule (0.162 nm^2 for nitrogen) and N_A the Avogadro number. With SSA known, the primary particle size (surface based) can be calculated by:

$$d_\mathrm{p} = \frac{6}{\rho_\mathrm{b} SSA} \tag{3.24}$$

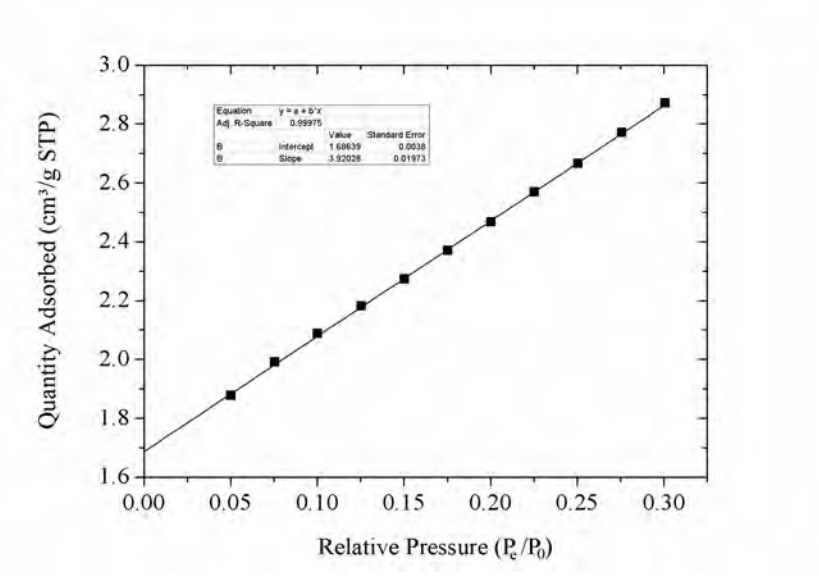

Figure 3.6: *BET isotherm for a copper nanopowder sample produced during this thesis*

3.2.3 Online characterization

In the following online measurement devices are described, which are used intensively in this study. The process developed in this work has shown changing product attributes (production rate, nanoparticle size, etc.) from the beginning, hence a dedicated online measurement system has been needed. For online measurements a Tapered Element Oscillating Microbalance (TEOM), a Scanning Mobility Particle Sizer (SMPS) and an Electrical Low Pressure Impactor (ELPI) are available. While each device leads to specific aerosol information (e.g. production rate, mobility diameter, aerodynamic diameter) their combination allows earning even more information (primary particle size, extend of agglomeration, mass mobility exponent). In the following, the utilized online (aerosol) measurement equipment for this thesis is described. Their combination, leading to a novel online characterization method is described in chapter 5.

3.2.3.1 Dilution system

The main goal of this work is to increase the production rate of metal nanoparticles. To verify the quality of those particles, standardized particle measurement equipment as discussed in the following is used, which however is not built to handle high particle number concentrations. Especially the optical measurement of aerosols is limited by the particle concentration. In order to ensure correct measurements of the devices and to reduce the cost of filter material

etc., an aerosol dilution system is required. Different kinds of dilution systems are known [98]. In this work an ejector dilution system is applied to reduce the particle concentration [54, 83]. The working principle is as follows. A sheath gas flow Q_{in} of nitrogen defined by a primary pressure passes a suction nozzle connected to the process line, to form a low pressure region in front of the suction nozzle inside the dilution system. The low pressure leads to a suction of aerosol Q_{a} inside the dilution chamber, in which both gas flows mix. The amount of aerosol sucked into the dilution system increases with Q_{in}, so that the dilution factor $W = (Q_{\mathrm{in}} + Q_{\mathrm{a}})/Q_{\mathrm{a}}$ is only dependent of the diameter of the suction nozzle. Dilution factors of ten to hundred are usually applied. By cascading further dilution systems this factor can be increased even further.

3.2.3.2 Tapered Element Oscillating Microbalance

The Tapered Element Oscillating Microbalance (TEOM) has been developed by Patashnick and Rupprecht [120]. The TEOM uses the mass dependency of the frequency of a harmonic oscillating element to determine the mass loading of an aerosol. The heart of the TEOM is an oscillating tapered element, a tube through which the aerosol with a constant volume flow (3 l/min by vacuum pump) is guided. A filter is arranged on the free end of the tube, so that the aerosol passes the filter before entering the tube. Aerosol particles deposit in the filter and thereby increase the mass of the filter and the tapered element. The frequency of the oscillating element changes. For a known system, the change of frequency can directly be used to calculate the mass loading of the filter and thereby of the aerosol, with the assumption that all particles are deposited in the filter.

A harmonic oscillator is described by the following equation:

$$\omega = 2\pi f = \sqrt{(\frac{k}{m})} \tag{3.25}$$

with $k = \frac{k_0}{4\pi^2}$, f being the frequency of the oscillating element, m the total mass and k_0 the specific restoring force constant. In the TEOM, the total mass m consists of the mass of the tapered element m_0, the filter mass m_{f} and the filter loading δm.

$$m = m_0 + m_{\mathrm{f}} + \delta m \tag{3.26}$$

With a defined filter loading m_{cal}, the specific restoring force constant k_0 can be determined for an oscillating element by:

$$f_1^2 = \frac{k_0}{m_{\mathrm{f}} + m_0} \tag{3.27}$$

and

$$f_2^2 = \frac{k_0}{m_\mathrm{f} + m_0 + m_\mathrm{cal}} \tag{3.28}$$

leading to:

$$k_0 = \frac{m_\mathrm{cal}}{1/f_2^2 - 1/f_1^2} \tag{3.29}$$

With k_0 defined, unknown mass loadings δm can be determined [120]:

$$\delta m = k_0(1/f_2^2 - 1/f_1^2) \tag{3.30}$$

Hence, the mass loading of the filter can be determined by the change of the frequency of the tapered element, when k_0 is known. It allows a direct measurement of aerosol mass concentration. The frequency is independent of the element mass or mass loadings of previous measurements. The approximation of a harmonic oscillator for the tapered oscillating element is confirmed by Patashnick and Rupprecht. Originally, the TEOM has been designed for ambient air monitoring [134, 158]. Nowadays, it is also used for comparison with other instruments in order to classify them, for example a total suspended particulate sampler developed at the university of Illinois [71] or other manual gravimetric [6] or technical methods [22]. It is noticeable that in the publications mentioned above, the mass concentration determined by TEOM seems lower than the ones measured by the counter methods, which is concluded to be a result of the heated filter. The filter of the TEOM is heated in order to reduce the thermal expansion of the tapered element that may affect the oscillating frequency and to minimize humidity caused deviations. This heating however may cause volatilization of collected organic compounds and therefore leads to an underestimation of airborne particle mass concentration [1]. It has been shown that the TEOM is suitable for mass concentration determination, when volatile particles are known and the TEOM values adjusted.

In this study, a synthetic aerosol containing metal nanoparticles is produced and its mass concentration determined by the TEOM. All metals used in this study are not volatile at the maximum heated filter temperature of 50°C. Nevertheless, in order to prove the correct estimation of production rates the mass concentrations are validated by gravimetric measurements.

Gravimetric measurements are widely used to determine particulate mass concentrations. A filter is weight before and after synthesis under defined conditions, concerning temperature and relative humidity. The filter can be made from different materials [21], but for further processing it seems constructive to choose a water-repellent filter material, to decrease mass measurements deviations. Since a lot of particle characterization is performed on deposited material, it is also desirable to choose a filter material, which is suitable for the applied characterization methods. For example a filter material that does not show any

diffraction peaks, at least not in the metallic region ($20^\circ \leq 2\theta \leq 120^\circ$) in XRD measurements or shows residues in ICP-MS samples. It has been found that PTFE filters with a pore size of 5 µm are suitable for deposition as well as characterization needs.

3.2.3.3 Scanning Mobility Particle Sizer

The Scanning Mobility Particle Sizer (SMPS) has been introduced by Wang and Flagan in 1990 [124,159]. Its development however has started almost 30 years before [164]. The SMPS is a measurement device consisting of neutralizer, a Differential Mobility Analyzer (DMA) [15] and a Condensation Particle Counter (CPC) [147]. It measures particle size distributions of aerosol particles in the size range from 3 to 700 nm. In order to characterize an aerosol with a SMPS, its particles have to be charged. Therefore, first the aerosol is led through a neutralizer, which generates a bipolar cloud of ions. Particles passing this cloud obtain a Boltzmann charge equilibrium [94, 165] and can be classified inside an ensuing DMA. The DMA has been developed in the seventies [79, 95, 164]. It classifies particles in a poly-disperse aerosol by their electrical mobility. A monodisperse aerosol results, which in principle means that all particles inside the aerosol have the same (mobility) size. The basic physical effect is the dependence of the velocity of a charged particle in an electric field on the particle diameter. The velocity of the particles is caused by the equilibrium between the Stokes drag force:

$$F_\mathrm{d} = \frac{3\pi\eta x d_\mathrm{m}}{C_C(d_\mathrm{m})} \tag{3.31}$$

and the electric field force:

$$F_\mathrm{e} = neE \tag{3.32}$$

with n being the number of elementary charge of the particle, e the elementary charge, E the electric field and d_m the electrical mobility diameter. From this, the electrical mobility Z_p is found to be:

$$Z_\mathrm{p} = \frac{x}{E} = \frac{neC_C}{3\pi\eta d_\mathrm{m}} \tag{3.33}$$

Depending on the DMA's geometry, sheath flow rates and classifying voltage, the particle size (electrical mobility diameter) can be calculated [37]. The size selection and monodispersity of the aerosol is referred to as transfer function of the DMA [63]. The monodisperse aerosol leaves the DMA and enters a particle detector. Usually a CPC is used, which enables optical particle detection by increasing the particle size by condensation of a saturated vapor (butanol). The combination of an electrical mobility analyzer and a particle counter can be used to compute a particle size distribution, which has first been combined in a Differential Mobility Particle Sizer (DMPS) [74]. A significant decrease

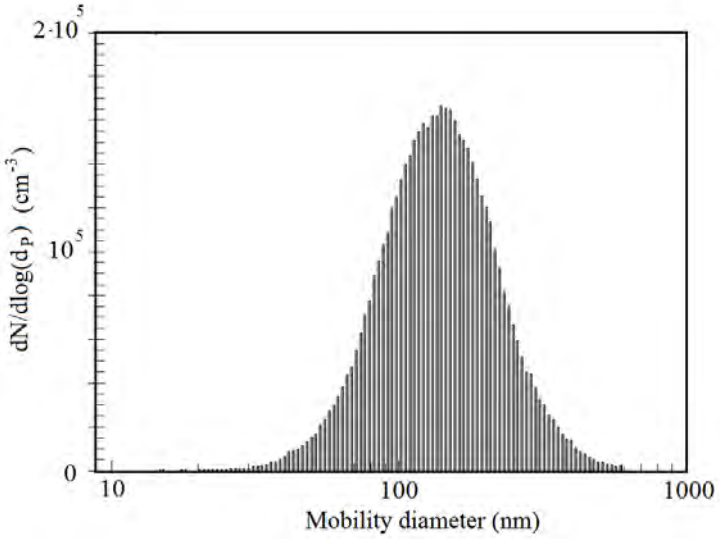

Figure 3.7: *Exemplary number size distribution measured by the SMPS*

in measurement time has then be realized by Wang and Flagan, as they have proposed the SMPS, in which the electric field is applied continuously (scanning) instead of in discrete steps as it is done in the DMPS. Figure 3.7 shows an exemplary number size distribution of arc produced copper particles measured by the SMPS.

3.2.3.4 Electrical Low Pressure Impactor

An even faster measurement of an aerosol size distribution is possible with an Electrical Low Pressure Impactor (ELPI). The distribution is not based on an electrical mobility diameter, but on an aerodynamic/ Stokes diameter. The ELPI has been presented by Keskinen et al. [75,105,106]. Aerosol particles are unipolar charged in a corona charger before they enter a low pressure cascade impactor. A multichannel electrometer connected to each plate measures the electric current carried by each particle onto the stage, when it deposits due to its inertia.

The cascade impactor is classically designed in a way that the gas flow is turned sharply in front of an impactor stage, so that particles of a defined inertia cannot follow the streamlines and deposit on the stage. The Stokes number Stk is a dimensionless parameter, which can be used to estimate whether particles collide with an impactor stage or not [7]:

$$Stk = \frac{\rho_\mathrm{b} C_c d_\mathrm{S}^2 x_\mathrm{c}}{9\eta l} \tag{3.34}$$

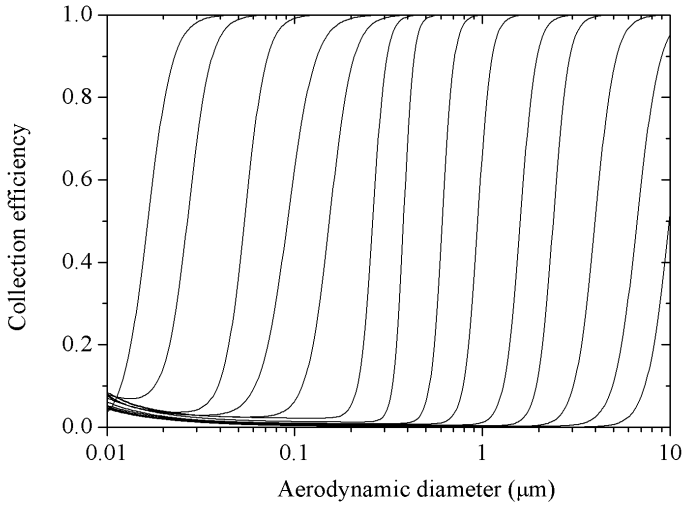

Figure 3.8: *Impactor collection efficiency curves (Stage 1 is the leftmost curve) [105]*

, x_{C} is the average velocity of the carrier gas at a nozzle above the impactor stage and l the diameter of the nozzle. For inertial classifiers such as the ELPI, the square root of Stk corresponding to d_{50} is used, to express the particle size, which is collected with an efficiency of 50%:

$$d_{\mathrm{S},50} = \sqrt{\frac{18\eta l}{\rho_{\mathrm{b}} C_c x_{\mathrm{C}}}} \sqrt{Stk_{50}} \tag{3.35}$$

Figure 3.8 shows the collection efficiency curve for each stage of the ELPI impactor [105]. The impactor stages have been designed so that particles with a diameter ($d_{\mathrm{S},50}$) between 0.03 and 10 µm are evenly deposited. Several impactor stages connected to an electrometer with different $d_{\mathrm{S},50}$ inside the ELPI allow hence the classification of different aerodynamic sizes. The number size distribution can then be obtained by using the electric signal. The number concentration (here for one stage i) is thereby obtained by the measured current of the impactor stage I_i and the charging efficiency $E_{\mathrm{ch}}(d_{m_i})$:

$$N_i = \frac{I_i}{E_{\mathrm{ch}}(d_i)} \tag{3.36}$$

d_i is the geometric mean diameter for the stage i, which has to be estimated by the aerodynamic diameter.

Combining SMPS and ELPI in simultaneous aerosol measurements can provide information about mass mobility exponent and effective density of agglom-

erates [129,154,155] and therefore leads to a method for rapid primary particle size determination, which has been realized in chapter 5.

Chapter 4

Optimized single arc discharge unit (OSU) for metal nanoparticle production

As explained before, in this work the scale-up of metal nanoparticle production is done by the parallelization of a single production unit, the optimal single unit (OSU, Figure 4.1). The basic process of nanoparticle production by the OSU is the transferred arc synthesis. The term OSU implies the complete synthesis reactor to form metal nanoparticles, which includes the housing and its connections, all the inner parts for gas flow adjustment and feedstock re-feeding and especially the electrode pair, which is the main part of the OSU.

In this chapter the experimental setup, the development and the optimization of a transferred arc synthesis process (the OSU) is described, with the goal of a controlled production of metal nanoparticles in larger amounts, while being energy efficient. Parts of this chapter have been published [146] and a German patent has been filed (see appendix D) .

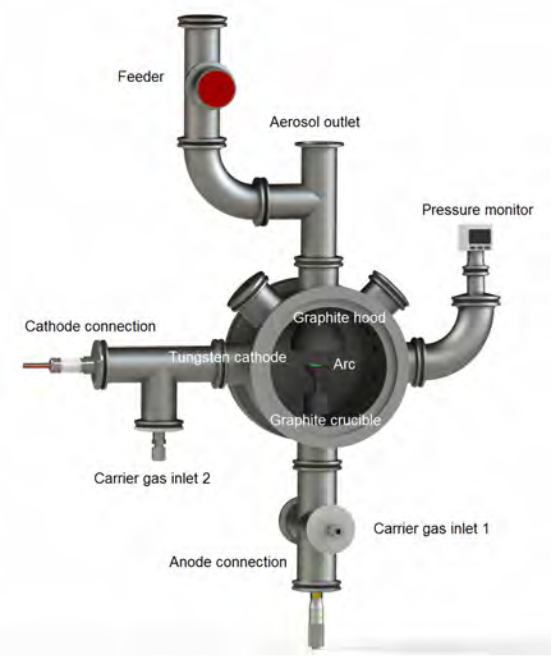

Figure 4.1: *Model of the Optimal Single Unit (OSU)*

4.1 Setup of the OSU

The setup of the OSU can be divided in three parts (Figure 4.2). First the general setup, which in principal summarizes all parts outside of the reactor chamber, starting with the reactor housing and its connections for power and gas supply or material feeding. The particle synthesis setup summarizes all the inner parts of the OSU, e.g. the electrode arrangement or gas flow adjustment, hence the parts where the nanoparticles are formed. The third part of the setup concentrates on the characterization of the formed nanoparticles, online as well as offline. Most of this characterization tools have already been described in section 3.2. A fourth important part of the experimental setup, which however is not directly a part of the scientific investigation, are the safety precautions, which have been considered e.g. when working with high currents or nanoparticles.

Figure 4.3 shows a picture of the overall setup for the OSU, which combines all parts discussed in this chapter.

4.1.1 General setup of the OSU

The heart of the general setup is the reactor chamber, in which metal evaporation and particle formation takes place (Figure 4.1). It consists of a double-walled housing which allows water-cooling. A technical drawing of the OSU

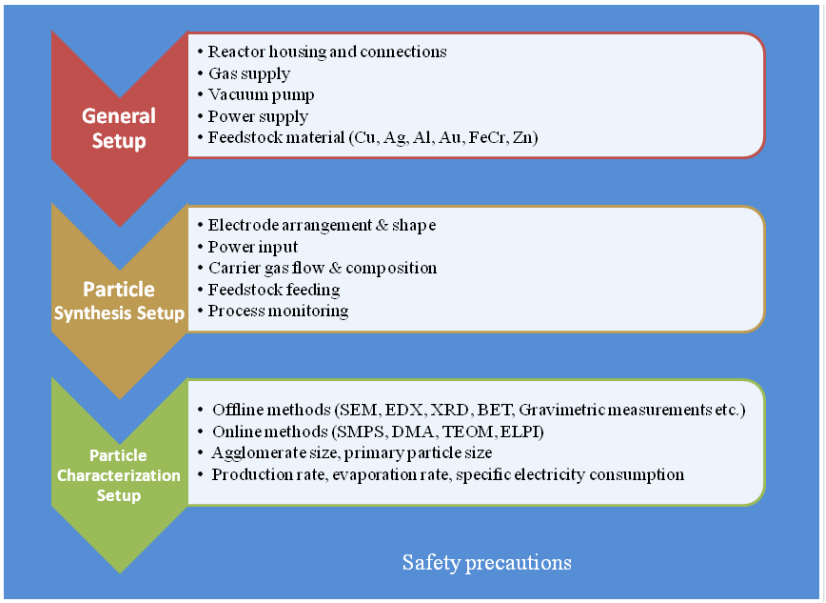

Figure 4.2: *Overall setup*

reactor housing is depicted in the appendix (B.1). It consists of a DN 160 ISO-K chamber, containing 6 circumferentially placed ISO-KF 40 ports, which can be used either for adaptive gas inlets (process or quenching gas), aerosol outlet, electrode arrangements, vacuum pump connection, monitoring tools or feeding mechanisms. The DN 160 ISO-K blank flange to close the OSU has a seventh ISO-KF 40 port, which can be used as a view-port inside the chamber.

The construction of the housing allows several gas flow inlets into the reactor chamber. The gas flows (3.5 to 50 l/min) are typically adjusted by mass flow controllers. As carrier gas nitrogen, argon, helium or 95 vol.% nitrogen + 5 vol.% hydrogen are used and their influence on particle properties investigated during this thesis. All gases have a purity of at least 99.9995%. Except for nitrogen, all gases are supplied by gas bottles. Nitrogen is supplied from the house line. In order to ensure the quality of the nitrogen, it is additionally cleaned by a purifier (Alphagaz Purifier O2-Free, Air Liquide, Düsseldorf, Germany) prior the mass flow controller.

With regard to the goal of an energy efficient synthesis, the process pressure is atmospheric, which means that no pumps have to be used during processing. However, in order to prevent oxygen contamination, the reactor chamber is evacuated and filled with the carrier gas prior the process. The reactor chamber is evacuated to 0.5 mbar by a vacuum pump (Adixen ACP 15, Pfeiffer Vakuum GmbH, Wertheim, Germany). The pressure is monitored by a vacuum transducer. By refilling, re-evacuating and again filling the system with the carrier gas, the oxygen concentration inside the chamber is reduced as much as possible.

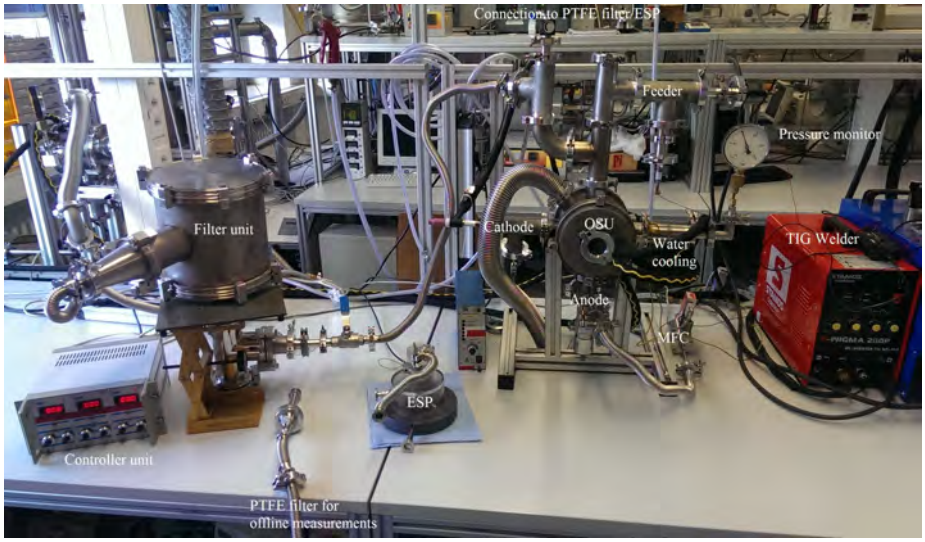

Figure 4.3: *Photograph of the overall OSU setup*

Two ports of the reactor chamber are used for the power supply connection, where a cost-effective power supply, an off-the-shelf TIG welding generator is connected. For transferred arc synthesis the specifications for such a device are simple. It needs a high frequency ignition mode, as the ignition by contact is difficult to realize inside the chamber and may cause a weld or feedstock impurities. Further it should have a constant current mode (up to 180A), which can be adjusted accurately. Several TIG welding generators have been investigated at the beginning of this study, the differences were found to be negligible so that the price has been the deciding criteria. Therefore, for most parts of this thesis a TIG welder of the company Expondo (Stamos S-Wigma 200P, Expondo GmbH, Berlin, Germany) is used. The electric connection is fed into the chamber by high vacuum feedthroughs.

To adhere to the idea of an economic production, no reactive or dangerous precursors are used in this study. Hence, the feedstock material defines the nanoparticle composition. Nevertheless, the interaction of the carrier gas and the feedstock needs to be taken into account. This study lays the focus on the production of metal nanoparticles, therefore nitrogen as carrier gas has to be avoided with nitride forming metals, such as aluminium. For nitride forming metals, other carrier gases such as argon are used. As feedstock material initially the metal in the form of 1 to 5 mm spherical shots are used, because they are easy to handle, especially for re-feeding the crucible.

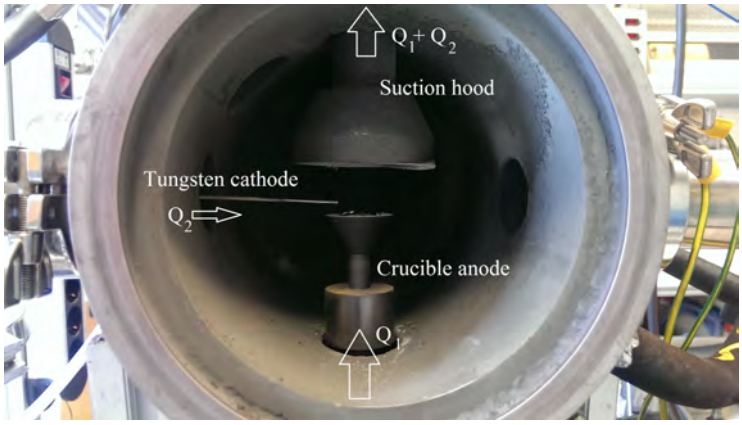

Figure 4.4: *Picture of the inner setup of the OSU, including the graphite crucible with a congealed silver melt, a graphite hood and the tungsten rod cathode*

4.1.2 Particle synthesis setup of the OSU (inner setup)

As the inner setup influences the particle formation process strongly, various gas flow and electrode arrangements are investigated. Important aspects of these investigations are summarized in the result sections of this chapter. Here, the final inner OSU setup depicted in figure 4.4 is discussed on a general basis, to explain the important parts of the inside of the chamber.

The transferred arc is ignited between two electrodes inside the reactor chamber. On the one hand there is the tungsten cathode in shape of a 1.6 mm rod, on the other hand the metal to be vaporized, which is stored initially as shots in a graphite crucible. The shape of the crucible is adjustable and later on investigated. In principal, the crucible has to be made of a conductive material with a much higher melting point than the metal, e.g graphite (sublimation temperature approx. 4000 K). The crucible sits on a crucible carrier, which is made of grade 1 titanium having relatively low heat conductance, while maintaining good electrical conductivity. The electrode distance is set between 3 and 7 mm, depending on feedstock material, carrier gas composition and gas flow. Both electrodes are connected to the power supply by high vacuum current feedthroughs (e.g. figure 4.5). The cathode (tungsten rod) is connected to the negative pole of the welding machine, as it delivers the electrons for the arc. The anode (crucible) is on the same potential as the housing and ground and therefore connected to the electrical grounding of the power supply. The arrangement of the two electrodes inside the reactor chamber is due to the design of the OSU housing flexible. While the position of the cathode is fixed in position during processing, the crucible can be adjusted in height by a micrometer screw or a vacuum lead through to adjust the gap distance between cathode and anode. A second graphite part can be seen in figure 4.4. It is referred to

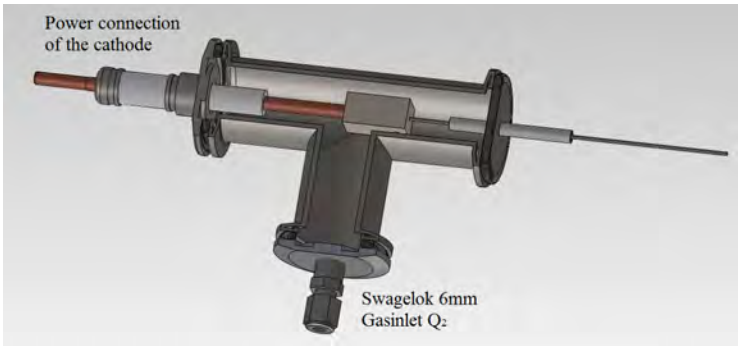

Figure 4.5: *Sectional view of the tungsten rod cathode connection with carrier gas inlet Q_2*

as a suction hood and is used to minimize particle losses inside the chamber. As there are different kind of suction hoods investigated in this theses, of which some are directly connected to the crucible, their design and development are discussed together with the crucible in the result sections.

Principally, the carrier gas flow inlets can be chosen flexible, too. However, they depend on the electrode arrangement. It is beneficial to use two gas flows, one main carrier gas flow Q_1 and one quench gas flow Q_2. The quench flow Q_2 is directed on the arc (cross-flow) and hence the formation zone of nanoparticles. It enters the chamber over an ISO-KF-40-tee and is directed towards the arc via a ceramic tube which surrounds the tungsten cathode, which current feed trough is also attached to the ISO-KF-40-T (Figure 4.5). The carrier gas flow Q_1 enters the chamber at the bottom by an ISO-KF 40 cross (axial-flow), where also the graphite crucible anode connection is placed. It flows upwards the crucible carrier, passing the crucible and entering the nanoparticle formation zone.

As material is evaporated from the graphite crucible, it has to be fed regularly into the crucible in order to maintain the arc running. The goal is to keep the melt on a constant level. A material shot feeder is presented in section 4.5. It supplies a controlled amount of material into the system. Hence, a guidance inside the chamber is needed, which leads the metal shots from the entrance in the chamber to the crucible. This guidance has been realized by a combination with the suction hood.

4.1.3 Particle characterization setup

The devices used for particle characterization are described in the fundamentals (section 3.2). The detailed setup for characterization depends on the measurements, which have to be performed. For the online determination of primary particle size (chapter 5), as well as the determination of sintering parameters

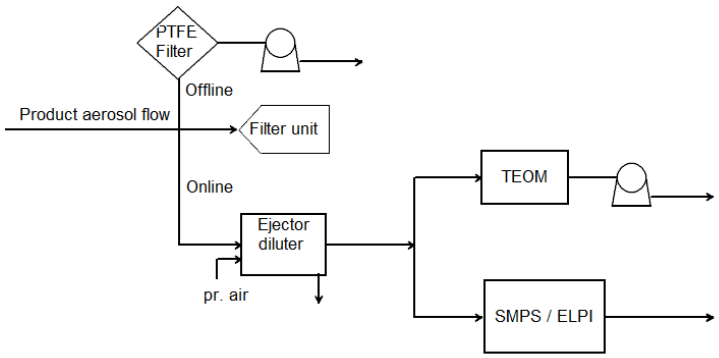

Figure 4.6: *Exemplary characterization setup*

(chapter 6) specific characterization setups are used and described in the belonging chapters.

As the main goal of this study is to design a synthesis process to produce large amounts of metal nanoparticles, three aerosol characteristics are found to be of most interest: the particles size, the production rate and specific electricity consumption. The characterization setup depicted in figure 4.6 is used to obtain the desired aerosol information.

The product aerosol is split in three flows in order to follow two characterization approaches. Offline measurements can be performed on particles, which have been deposited either on a TEM-grid via electrostatic precipitation (Dixkens and Fissan 1999) for TEM measurement (JSM 7500F, JEOL, Tokyo, Japan) or on a PTFE filter with a pore size of 5 µm for gravimetric, BET(Gemini VII 2390, Micromeritics GmbH, Aachen, Germany) or XRD measurements (X'pert Pro MPD with Ni-filtered copper Kα radiation, PANalytical, Almelo, Netherlands). The filter is suitable for XRD measurements of metals, since it does not show any diffraction peaks at angles above 20°. The data is recorded in steps of $2\theta = 0.01°$ over a range of $20° \leq 2\theta \leq 120°$. By weighing the filter and the crucible prior and post synthesis a production as well as an evaporation rate can be determined.

The second gas flow is used for online measurements. Typically, a dilution system is used to bring the particle concentration (typically $10^7 - 10^8$ cm^{-3}) within the measurement range (below 10^6 cm^{-3} for SMPS and ELPI) of the measurement devices. The TEOM obtains information about the aerosol mass density (µg/m^3), which allows calculating the production rate when the carrier gas flow is known. The ELPI or SMPS gives information about the particle sizes in form of number based size distributions. By monitoring the applied

current and voltage over the electrodes, the specific electricity consumption (SEC) (kWh/kg) can be calculated by means of:

$$\text{SEC (kWh/kg)} = \text{Arc power (kW)} / \text{Production rate (kg/h)} \tag{4.1}$$

The remaining aerosol flow that is not needed for characterization is led into a filter, where the particles are separated from the carrier gas.

4.1.4 Safety requirements

The safety requirements for a nanoparticle production unit such as the OSU are quite stringent and base partly on assumptions, as the full hazardous potential of nanoparticles is not understood completely yet. A discussion of all safety relevant aspects for this process would surely go beyond the scope of this thesis. Here following headwords are given to summarize the most important issues, when working with nanoparticles:

- Nanoparticles may cause irritation of skin, eyes or lung
  - Reactor must be closed during process
  - Reactor must be equipped with overpressure valves
  - Protective equipment must be worn when working with nanoparticles
  - Dust emission must be reduced to a minimum
    - Cleaning of process equipment covered with nanoparticles by wet cloths
- Especially metal nanoparticles can ignite or explode during fast oxidization
  - Controlled passivation of metal nanoparticles before releasing to ambient air
  - Particles / Reactor must be kept away from reactive substances

4.2 Crucible design and electrode arrangement

This section describes the development of the crucible design and electrode arrangement inside the reactor chamber for optimal conditions of particle synthesis via transferred arc. The reactor chamber allows due to its design multiple arrangement possibilities. Electrode arrangement means thereby the position of the two electrodes relative to each other, as well as the shape of the crucible and the direction of the gas flow on the electrodes and arc. Figure 4.7 shows an exemplary crucible design and an electrode arrangement of the transferred arc

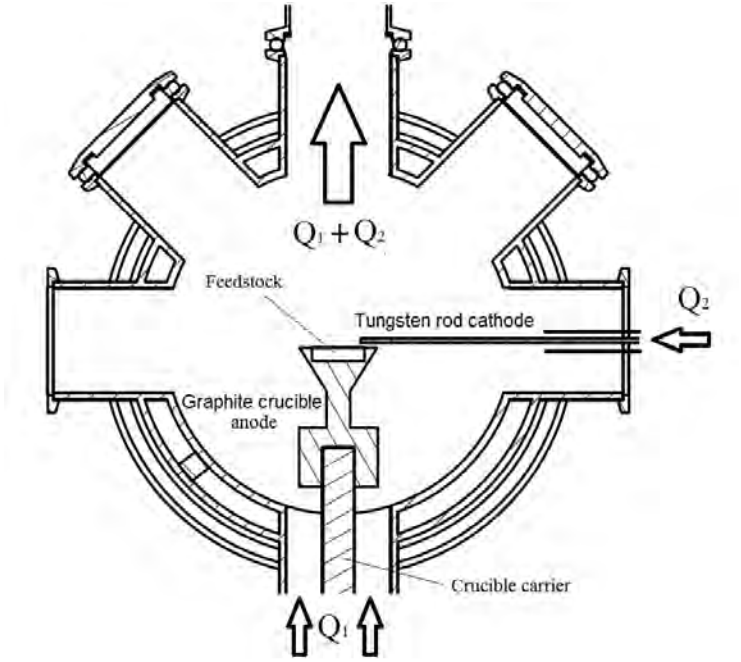

Figure 4.7: *Exemplary crucible design and electrode arrangement for a transferred arc synthesis*

setup. The tungsten rod cathode is coming from the side. It has been found early during this investigations that the cathode arrangement from the side is more advantageous in comparison to other positions. With this cathode position, the arc runs stable and is easy to ignite. Furthermore, high power arcs can be used without any visible cathode consumption as the up-streaming arc does not heat the cathode that strongly. The crucible anode is sitting on a crucible carrier at the bottom of the reactor chamber. This position is also fixed as the crucible carries the feedstock, which eventually turns liquid. Two gas flows are adjusted: an axial flow Q_1, which enters the reactor chamber at the bottom flange streaming along the crucible and a cross flow Q_2, coming from the side streaming along the cathode directed on the arc. The aerosol outlet is usually the top flange of the reactor housing using also the buoyancy.

The crucible anode is a crucial part of the transferred arc synthesis. Multiple crucible designs and electrode arrangements are therefore tested during this study. In all cases, the crucible is not cooled in order to minimize energy losses and to keep the reactor chamber as simple as possible. All crucibles are made of a massive graphite rod. A cylindrical recess with a diameter of 20 mm and a depth of 10 mm is used to fill in the feedstock material to be evaporated. On the other side a carrier recess with a diameter of 21 mm is implanted for the tungsten crucible carrier.

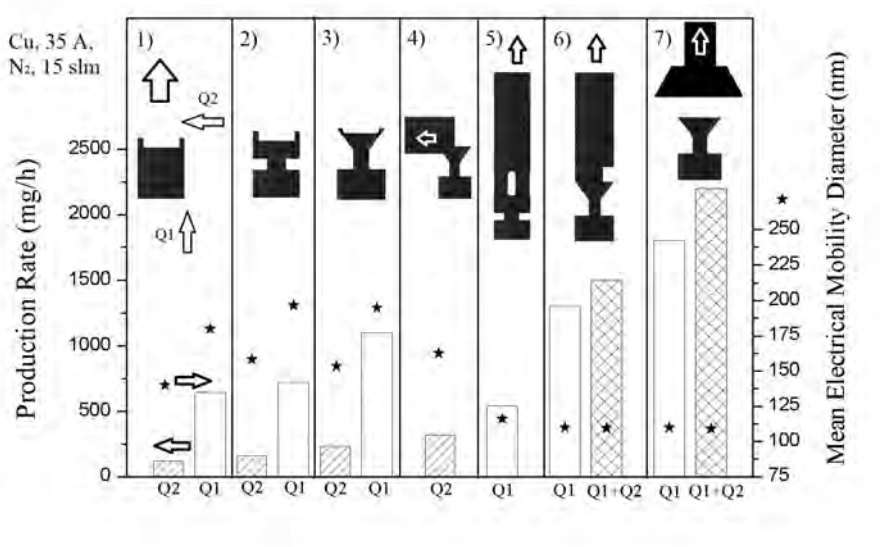

Figure 4.8: *Effect of crucible design on production rate (bars) and particle size (asterisks) with Q_1 using only the axial gas flow, Q_2 only the cross gas flow and $Q_1 + Q_2$ a combination of both flows. (Total gas flows 15 l/min, 35 A, in nitrogen for copper)*

Figure 4.8 depicts different crucible designs and their effect on production rate (bars) and particle size (asterisks), also depending on the gas flow direction for copper nanoparticles. The test conditions are almost similar for each crucible. The tungsten rod cathode comes from the side. The axial flow from bottom to top being Q_1 and the cross flow Q_2 coming from the side over the cathode rod as depicted in Figure 4.7. Some results are obtained for both gas flows combined ($Q_1 + Q_2$). The total gas flow (nitrogen, 15 l/min) and the applied current (35 A) are kept constant.

Crucible 1 is the simplest to manufacture. The maximum production rate reached is about 700 mg/h (for Q_1). Although the same current is applied, the production rate in the axial setup (Q_1) is much higher than the production rate in the cross setup (Q_2). Since arc synthesis is a highly thermal process, an upward gas flow in the same direction as the buoyancy leads to less wall deposition and thereby to a higher process efficiency, as less turbulences and smaller temperature gradients occur. Another advantage of the axial setup is a much more stable arc, which is especially for lower electric currents and the lower energetic arcs useful. The production rate of the cross flow setup is much lower, but the influence of the gas flow on the particle size (mobility diameter) is found to be greater, so that the particle size control is easier and smaller

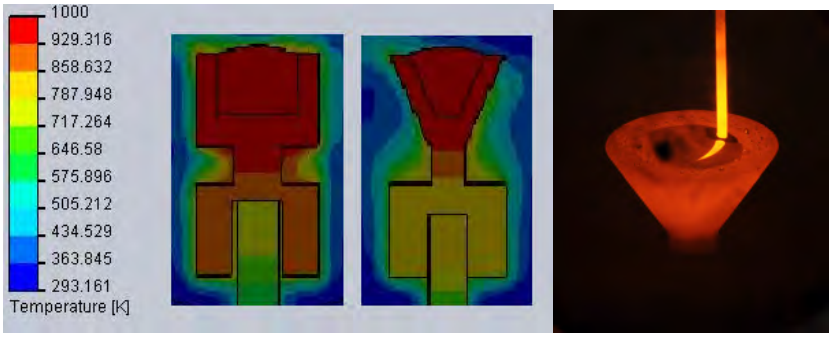

Figure 4.9: *Comparison of heat loss of crucible 2 and 3 and image of crucible 3 directly after extinguishing arc*

particles can be produced. In the cross flow setup the gas flow is directly guided towards the arc and therefore to the particle nucleation zone, smaller residence times result, which lead to smaller particles.

Crucible 2 has a reduced diameter in the middle part in order to reduce the heat losses towards the current feedthrough, which results in a minor increase of production rate and particle size. This approach has been a crucial factor during the design of crucible 3. By shaping the upper part of the crucible conically, the heat losses have been reduced significantly (figure 4.9), which is also reflected in the production rate. Figure 4.9 depicts a comparison of the modeled heat losses of crucible 2 and 3 and a picture of the glowing crucible 3 directly after the arc extinguished, here with the tungsten cathode from the top. The glowing is reduced significantly at the end of the conical top. With crucible 3, a production rate of copper nanoparticles above 1 g/h is achieved. Some of the investigations shown in the following sections are done with this design.

Starting with crucible 4, the goal has no longer been to optimize the evaporation of material by the shape of the crucible, but to reduce the losses inside the reactor chamber. The water-cooled walls of the reactor are a thermophoretic trap for the produced particles. In principal most of the ensuing crucible designs base on crucible 3. Crucible 4 has a graphite pipe added so that flow Q_2 is guided out of the reactor zone. Here, the gas outlet is at the side. However, due to the upward gas flow as a result of the buoyancy, a lot of particles do not enter the pipe. In comparison to crucible 3, a small increase in production rate is observed when using the cross flow mode (Q_2), but in comparison to the axial flow mode (Q_1) of crucible 3, the production rate decreases strongly.

With crucible 5, 6 and 7 three different approaches have been investigated to optimize the axial flow mode, as this configuration has been proven to be more productive. As some of these designs have a direct contact between the crucible and the upper ISO-KF-40 port, they are capable for gravity-based feeding of feedstock material into the crucible, which is discussed in section 4.5. The added

Figure 4.10: *Clogging of crucible 6*

funnel is hence not only used as a guided aerosol outlet, but also as a guidance for feedstock material back into the crucible.

Crucible design 5 shows a significant decrease in production rate in comparison to crucible 3. The added graphite pipe (funnel) has been manufactured with four elongated holes for a consistent gas inlet, but the arc tends to exit the aerosol guidance through one of the holes opposite to the cathode at higher currents. Most of the particles are deposited inside the chamber.

To overcome this problem, the funnel of crucible 6 has only one inlet. It shows very high production rates (1300 mg/h) at the axial flow mode (Q_1). This design has been investigated intensively during this study and some of the results in this study have been achieved with this crucible design. By adding a cross flow Q_2 to the main flow Q_1 (total gas flow constant 15 l/min), the production rate is increased further, while the particle size is reduced. The combination of cross and axial flow appears to be an optimum solution to increase the production rate, while keeping the particle size in the desired nanoscale range. With this setup, almost no particle deposition inside the chamber is visible after synthesis. A production rate of 1.5 g/h (with the discussed parameters) is reached. But clogging of the crucible pipe occurs after some time (figure 4.10) with this setup at high production rates.

The clogging appears inside the funnel, so it seems that splashed material from the melt deposits atop of it. The deposition takes place at local temperatures, which are not sufficient to re-melt the material. If splashed material is deposited somewhere in the funnel, metal vapor condensates on it and quickly clog the funnel. In order to reduce the precipitation inside the exhaust pipe, a higher gas flow Q_1 (40 l/min) can be used. The higher gas flow reduces the clogging in the upper part of the pipe, but favors the development of a clogging, positioned directly above the melt. Another issue of this design is the thermal conductivity of the funnel. Despite the active cooling, the high temperatures at the outlet flange of the reactor housing lead to a damaging of the rubber sealing, which requires additional cooling. Crucible design 6 is hence a good melt carrier

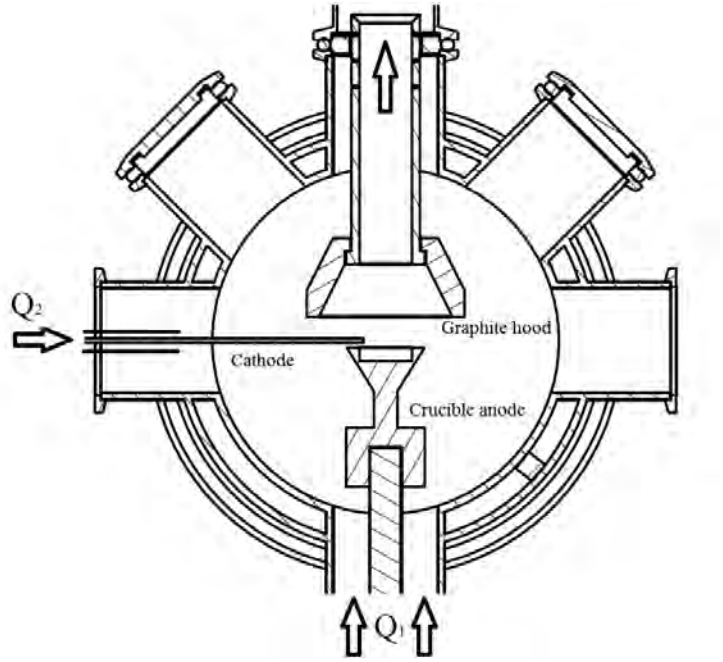

Figure 4.11: *Optimal inner OSU design*

and aerosol guidance for low power or low production rate processes. For a high production process this design is not convenient due to the clogging problem.

To surmount the clogging problem, crucible design 7 has been tested. Figure 4.11 shows the inner design of the OSU with crucible design 7, which is found to result in the highest production rates and smallest primary particles sizes. The crucible is separated from the aerosol outlet guidance, in this case a 60 mm graphite hood with an opening of 52 mm and an angle of 62° to overcome the clogging as well as the thermal conductivity problem. A hood above a particle-forming zone has been used e.g. in laser-decomposition reactors [86]. The space between crucible and hood is variable and shows no clogging after 8h for copper nanoparticle production. This setup has several advantages in comparison with the former designs. First, clogging due to splashed particles does not appear anymore. Second, the heat losses at the crucible are decreased significantly due to the separation of crucible and hood. Technical drawings of the crucible and hood are depicted in the appendix (B.2, B.3, B.4). Production rates > 2 g/h are reached with this setup. Due to the combination of Q_1 and Q_2, the particle size can be reduced to less than 100 nm.

The cross gas flow Q_2 has a significant influence on the particle size. But it also effects the arc directly. At higher values (5 l/min) it deflects the arc away from the center (figure 4.12). The design of the hood, allows thereby working

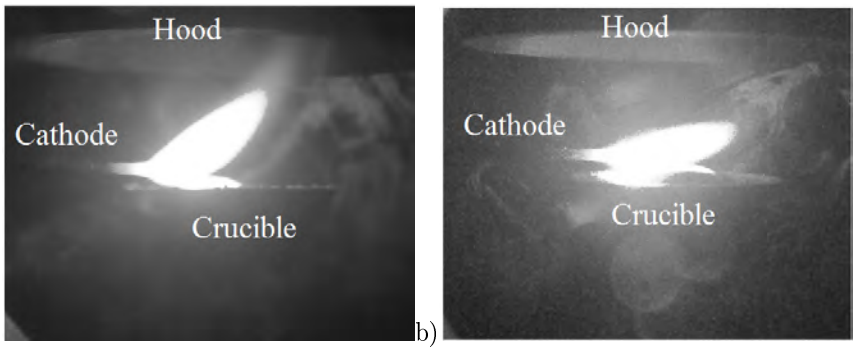

a) b)

Figure 4.12: *Transferred arc of crucible design 7 with a cross flow Q_2= 0 l/min (a) and 5 l/min (b). (Cu, 35 A, Q_1 = 40 l/min)*

with additional cross flows up to 5 l/min, without losing too many particles inside the reactor chamber. These values can not be reached with other setups. Figure 4.12 shows the transferred arc with crucible design 7 at two different cross flows. The impact of the cross flow is discussed in section 4.4.

Summarizing, it can be said that for high power and highly productive arcs crucible 7 is the most promising. It shows comparatively high production rates with relatively small particle sizes. Furthermore, it shows a good performance in terms of long term running as no clogging or extensive heat development appears. Some particle losses inside the reactor chamber appear, which are at least for the high production arcs negligible. For materials with a low vapor pressure, hence for low production arcs, crucible 6 is advantageous, as almost no particle losses appear and clogging seems only problematic at production rates $>$ 1 g/h.

The development of the crucible design (CD) and the optimal inner setup of the OSU has been a long-standing process, while in parallel other relevant investigations for this study have been undertaken. These investigations have been done with earlier crucible designs.

4.3 Effect of carrier gas composition on nanoparticle synthesis

It is well known that the carrier gas composition has a marked influence on transferred arc synthesis. Munz et al. have used a transferred arc to synthesize silica and aluminum nitride [113]. They show that hydrogen addition to argon increases the silica production. Tanaka et al. explain the enhanced evaporation of feedstock material by the addition of hydrogen or nitrogen to argon in a transferred arc by the formation of small hydrogen (nitrogen) bubbles in silicon [149]. Those bubbles are capable of transporting additional silicon atoms to

the top of the melt and thereby increase the production rate. They have found that hydrogen bubbles are less effective to form bigger bubbles and hence to provide less material than nitrogen bubbles, due to the faster atomic hydrogen diffusion in the melt. A production rate enhancement of manganese-silver alloy nanoparticles by hydrogen addition to a transferred arc discharge due to tiny hydrogen bubble formation is also reported by Lee et al. [89]. Also Shin et al. have found that the addition of nitrogen to argon as quench gas increases the evaporation of copper powder [142].

According to Murphy [115], the important arc parameters influenced by the gas composition are: the heat flux density, current density and thermal and electrical conductivity, which can lead to a variation in anode temperature and thereby directly influencing the evaporation rate. Table 4.1 shows the results of their numerical simulations of an arc between a tungsten cathode and a water-cooled copper anode for different gases mixed with argon. The heat flux and current density, which probably have the highest influence on the melt heating and evaporation, increase significantly in ascending order, when helium, nitrogen or hydrogen is added even at the moderate concentrations around 10 vol.% used in this study.

For the investigation of the impact of the carrier gas on the production of metal nanoparticles, CD 3 is used with a carrier gas flow $Q_1 = 10$ l/min (see previous section). As carrier gas nitrogen, argon, helium and 95 vol.% nitrogen + 5 vol.% hydrogen are used to investigate their influence on particle formation. As material copper, silver and zinc are investigated as they do not react with any of those carrier gases.

The determined production rates (figure 4.13) behave as expected in accordance to the calculations of Murphy for argon and helium carrier gases, which show an increase of thermal conductivity, heat flux density and current density. More zinc is produced than silver and copper in agreement with its much higher vapor pressure (at 1200K for zinc 103 mbar, for silver 10^{-3} mbar, for copper 10^{-5} mbar; [59]). The change from an argon to a helium arc increases the particle production rate of all three metals approximately by factor 5 at constant electric current. From the investigated gases, argon has the highest electric conductivity and lowest heat capacity, which leads to a broad, but comparatively low power arc [128]. Hence, less material is evaporated.

When nitrogen is used as carrier gas, the heat flux and current density at the anode is larger, the arc power and therefore the evaporation rate increase. However, the large increase in production rate is not only caused by the enhanced thermal evaporation. Tanaka et al. have observed a significant increase in production rate of silicon nanoparticles, when adding nitrogen to an argon arc [149]. They conclude that molecular nitrogen dissociates completely at high arc temperatures leading to an extremely high partial pressure of atomic nitro-

Table 4.1: *Influence of different argon gas mixtures on important arc parameters (Data taken from Murphy et al. [116])*

Carrier gas	Thermal conductivity	Electrical conductivity	Heat flux density	Current density
	(W/mK)	(A/Vm)	W/mm^2	A/mm^2
Ar	2.3	7.5	50	7.2
Ar+10vol.% He	2.4	7.3	55	7.3
Ar+10vol.% N_2	2.6	7.3	63	9.5
Ar+10vol.% H_2	3	7.2	90	10.9

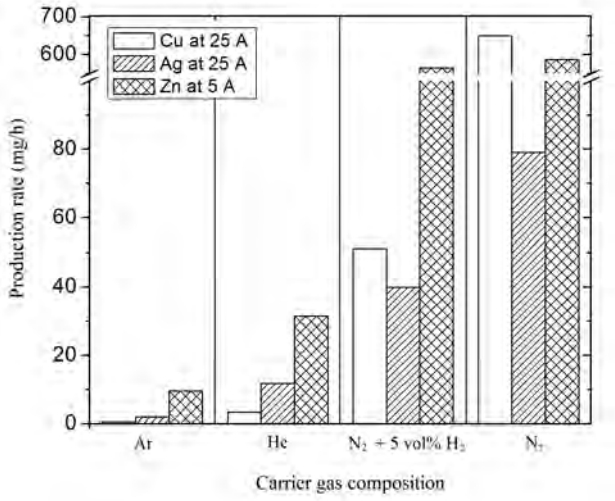

Figure 4.13: *Dependence of the gas composition on the production rate for copper, silver (both 25A) and zinc (5A) in the cross flow arrangement (CD 3, $Q_1 = 10$ l/min) [146]*

gen in the arc. On the other hand, nitrogen atoms recombine outside the arc to form molecular nitrogen again, maintaining a low atomic nitrogen partial pressure. The steady recombination of atomic nitrogen generates more heat that can be used for material evaporation. This effect can only occur in a bi-atomic gas, such as nitrogen or hydrogen. Also a mechanically caused increase in production rate is described due to the formation of small bubbles in the molten feedstock containing nitrogen, which splash fine molten feedstock material, when moving to the surface outside of the arc. The movement of those bubbles is also explained by the difference in partial pressure of the nitrogen. Figure 4.14 shows a schematic describing these effects. The effect of bubble formation has also been observed by Lee et al. for manganese aluminum alloys and Förster et al. for copper, when adding hydrogen to an argon arc [89] [39].

In this study, all production rates increase further, when changing from a pure helium to a pure nitrogen arc (figure 4.13), but not in accordance to the vapor pressure of the metals. The production rate of copper in nitrogen is 100 times higher in comparison to the one of copper in helium. A significant increase in particle production by a factor of 20 is also observed for zinc. The production rate of silver however increases only by a factor of 5, so that the production rate of copper particles now exceeds the one of silver.

An explanation for the smaller increase in production rate of silver in comparison to copper is difficult to find and might be a consequence of different effects. XRD measurements indicate crystalline zinc, silver and copper with all

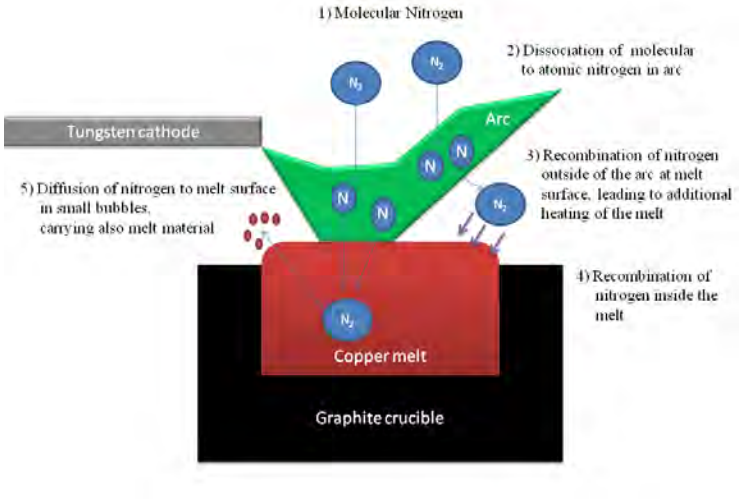

Figure 4.14: *Schematic nitrogen dissociation, recombination and the effect of bubble formation*

carrier gases with minimal oxygen contaminations. As an example figure 4.15 shows the XRD pattern when nitrogen is used as carrier gas. For the sake of completeness, here also the XRD patterns of aluminium and FeCr are shown. These samples are shown for an argon arc, as aluminium and FeCr would form nitrides, when working with nitrogen. It is found that the initial composition of FeCr is not conserved in the produced powder (nanoparticles) as the XRD pattern can be assigned mostly to chromium.

The significant increase in copper evaporation in nitrogen can be observed visually through the observation window. The change from an argon arc to a nitrogen arc leads to a broader, bright green-lighting arc. The weld pool in the crucible expands, but remains shallow. Figure 4.16 shows the shallow congealed copper (c) with cavities and almost spherically shaped silver (a) feedstock material. Large cavities are observable inside the congealed copper, which are assumed to be a result of the nitrogen bubble formation described above. This is not observed for silver. In the nitrogen arc the molten silver takes an almost spherical shape. The spherical shape of the silver melt is conserved, when the arc is extinguished and the silver congeals. No cavities are observable. It appears that the formation of tiny nitrogen bubbles in silver is suppressed, which might be a consequence of the decreased diffusion of nitrogen in silver in contrast to copper [149]. For zinc (b), almost no material remains after processing even for short times, due to the fast evaporation. EDX measurements have been performed on the congealed silver and copper to investigate the composition of the feedstock material after synthesis. Both materials show relics of tungsten

and oxygen on the surface of the melt, so one can conclude that the feedstock impurities are not responsible for the different evaporation behavior. During synthesis, a copper oxide layer on the melt would directly evaporate due to the higher vapor pressure in comparison to pure copper [100]. The tungsten relics appear to behave as a kind of slag on the melt, since they are mainly detected at the edge of both samples. This might explain also why no tungsten impurities are detected by XRD in the particles.

The nitrogen arc also appears smaller in case of the silver. The arc shape and attachment to the anode seems to influence the evaporation remarkably. Nonetheless, the reason for the difference in arc attachment is not understood. Metal vapor may influence the evaporation rate of the anode material. It is reported that even a low concentration of metal vapor can increase the electrical conductivity and therefore lowers the arc power [32, 43, 115]. A decreased evaporation may result. It is however unlikely that copper vapor, in comparison to silver vapor, leads to a significant difference in those conductivities at low concentrations.

The production rate of copper, silver (both at 25A) and zinc (5A) in a carrier gas composed of 5 vol.% hydrogen in nitrogen is also displayed in figure 4.13. The production rate of copper particles is higher than the one of silver in the nitrogen + 5 vol.% hydrogen mixture, but is smaller than the one in a pure nitrogen atmosphere. In view of the larger heat flux and current density predicted by Murphy et al. (2010) [115] for the hydrogen mixture as compared to the nitrogen mixture, this is not expected. Figure 4.16 displays the congealed copper feedstock after nitrogen (c) and nitrogen + 5 vol.% hydrogen (d) processing. As can be seen, the feedstock shape changes significantly due to the hydrogen addition. The congealed copper shows a shiny surface, as it is the case for the congealed silver after nitrogen processing. Almost no visible cavities appear. This may confirm the impact of the absorption of nitrogen (hydrogen) into the molten feedstock and the formation of small bubbles, which increase the production rate. A cut through photograph of the congealed copper feedstock after nitrogen (a) and 5 vol.% hydrogen mixture (b) is shown in figure 4.17. In the nitrogen sample, large cavities appear at the surface of the feedstock. In contrast to this, no cavities are visible at the surface of the hydrogen sample, but small bubbles appear inside the sample. This observation is confirmed by the hypothesis that hydrogen bubbles are less effective to form bigger bubbles than nitrogen, which might be a consequence of the faster diffusion of hydrogen atoms in the molten feedstock [149]. Smaller bubbles splash less material. Accordingly, the splashing material appears to have a greater effect on the production rate than the increased feedstock temperature, since for copper the particle production rate in the nitrogen + 5 vol.% hydrogen arc is a factor of 13 smaller than that in a pure nitrogen arc.

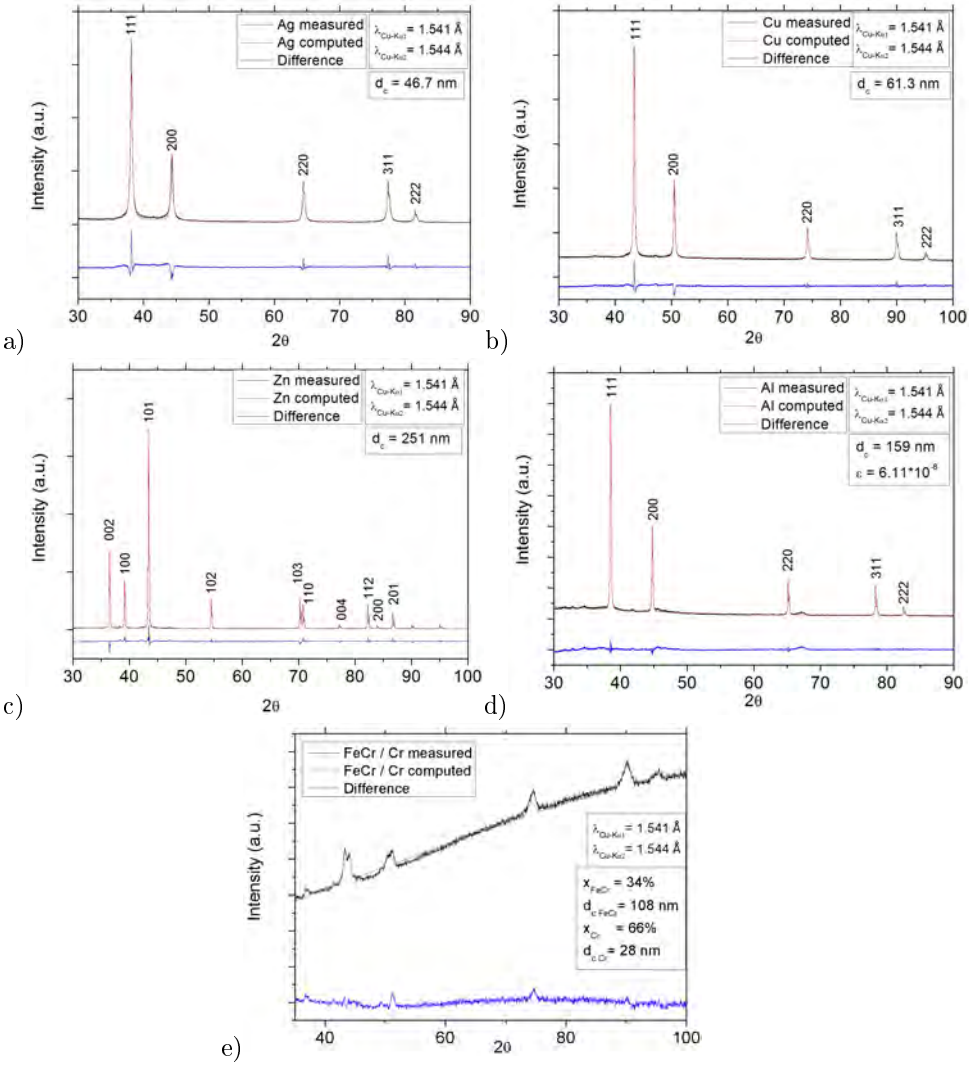

Figure 4.15: *XRD pattern for Ag (a), Cu (b), Zn (c) synthesized in a nitrogen plasma and Al d), FeCr e) in formed in a argon plasma. d_C is the calculated crystalline size of the metal particles and x the composition [146]*

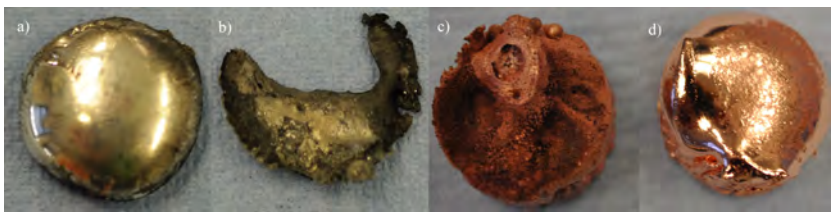

Figure 4.16: *Congealed feedstock of a) silver, b) zinc, c) copper after arc evaporation in nitrogen atmosphere and d) copper after arc evaporation in nitrogen + 5 vol.% hydrogen atmosphere [146]*

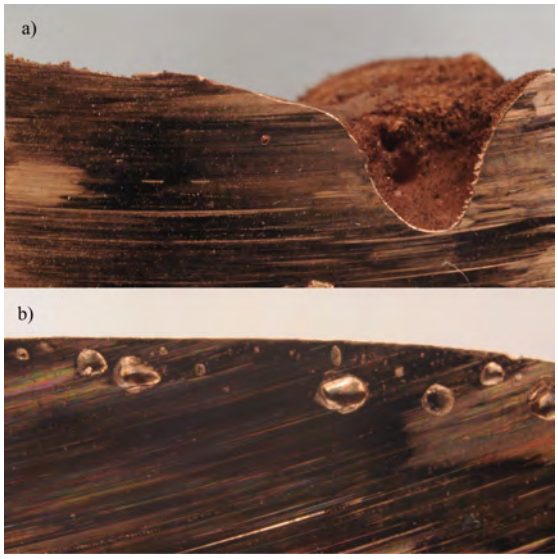

Figure 4.17: *Section photograph of the congealed copper feedstock after a) pure nitrogen arc processing and b) nitrogen + 5% hydrogen processing [146]*

However, the splashing of nitrogen bubbles might lead to the formation of micron-sized particles, which affect the production rate significantly. SEM measurements show some micron-sized particles directly after the reactor, but much less in front of the measurement equipment. This may be the consequence of several bends in the aerosol line from the reactor to the measurement zone and the dilution system, where micron-sized particles may impact due to their large inertia, whereas the smaller produced particles have much smaller relaxation times and react faster on a direction change of the carrier gas. Especially at those bends particle depositions are observed, so one can conclude that the effect of the micron-sized particles on the production rate is not that significant, because they will not enter the measurement system, but should not be neglected.

Since the effect of bubble formation is a consequence of the dissociation and recombination of bi-atomic molecular gases, they seem more suitable for arc evaporation than atomic gases. It is remarkable that the atomic gases behave as expected in terms of production rate opposed to the bi-atomic molecular gases, which cannot be predicted by Murphy's model as this does not include the bubble formation.

The strong influence of the carrier gas on the production rate directly impacts the specific electricity consumption (figure 4.18). Since the highest production rate is reached in a nitrogen arc, its specific electricity consumption is the lowest for all three metals. The nitrogen + 5 vol.% hydrogen mixture, helium and argon follow in ascending order for all investigated metals. Zinc has the lowest specific electricity consumption due to its low melting point. The

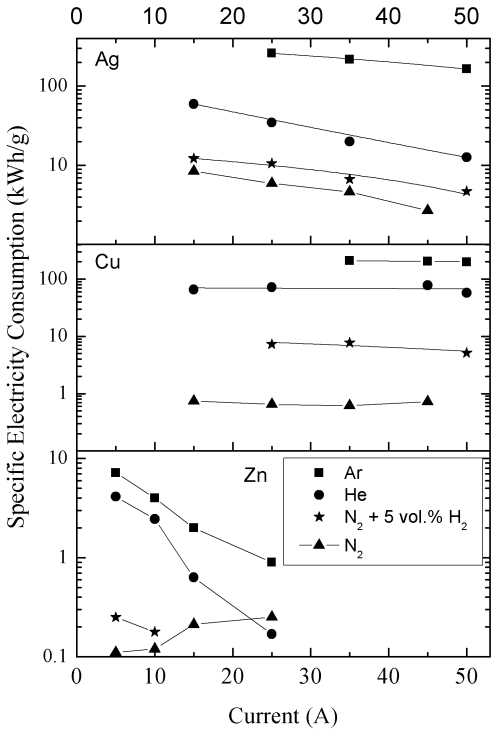

Figure 4.18: *Specific electricity consumption for silver, copper and zinc depending on applied electric current and carrier gas composition (CD 3, $Q_1 = 10$ l/min) [146]*

consumption arranges between 0.1 and 10 kWh/g and is below 1 kWh/g at 25A for all gases tested. For copper only in case of nitrogen as carrier gas it is below 1 kWh/g, for the other gases one or two orders of magnitude higher. The specific electricity consumption of silver is similar to that of copper, except for the case of nitrogen, where it shows 3 to 5 times larger values. Hence, the specific electricity consumption is not only power and material dependent, but depends also strongly on the carrier gas composition used for synthesis. For the investigated metals, nitrogen appears to be the most efficient carrier gas.

The previous results have all been obtained with the goal of maximizing the production rate and hence a reduced specific electricity consumption. For some applications however, not the production rate per se of nanoparticles is important, but the production rate of nanoparticles at a defined particle size. The carrier gas composition can also be used to manipulate the primary particle size, but at the expense of the production rate. It is a comparatively easy way to change the primary particle size significantly in arc synthesis e.g. by adding argon to a nitrogen carrier gas and thereby reduce the nitrogen concentration.

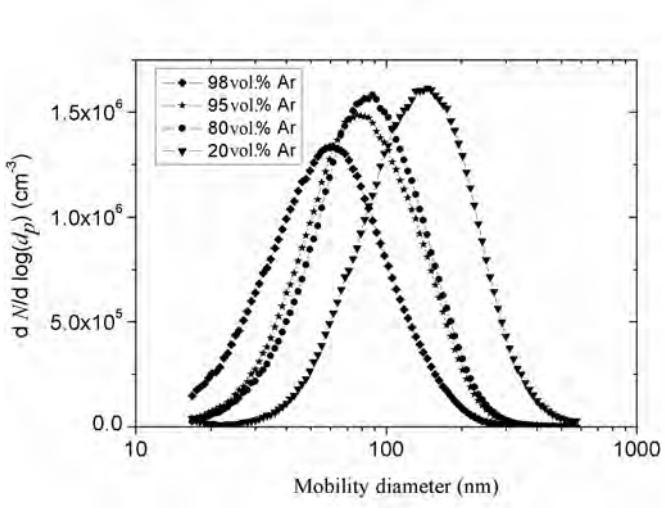

Figure 4.19: *Number-based particle size distribution for copper particles at different argon/nitrogen composition (CD 6, Q_1 = 15 l/min, Dilution factor 100) [145]*

Argon has also the advantage of increasing the stability of the arc due to its lower energy threshold to form atomic ions [69]. A first impression of the impact of the gas mixtures is given in figure 4.19, where the number size distributions are measured at different nitrogen-argon concentrations with the SMPS. The mobility diameter obtained by the SMPS gives an indication of the diameter of the agglomerates as they appear in the aerosol. The mean agglomerate size shifts to larger values with higher nitrogen concentration. The arc power and evaporation rate increase significantly, when nitrogen is added to argon. Hence, more material is evaporated so that larger agglomerates are formed. The mean agglomerate size doubles, when using 80 instead of 5 vol.% nitrogen. Although it is not shown here, it is remarkable that the agglomerate size does not increase further in the concentration range between 40 and 100 vol.% nitrogen. The number concentration and mean mobility diameter of the agglomerates formed at high nitrogen concentrations changes only marginally, when varying the exact concentration.

As depicted in figure 4.20, the primary particle volume obtained by BET measurements increases with the nitrogen concentration. This explains also, why the production rate increases further, although the mobility diameter and number concentration remain almost the same (figure 4.19). It appears that denser agglomerates are formed at higher nitrogen concentrations. The primary particle volume increases linearly with the production rate, which leads to the assumption that the increase in production rate is mostly dependent on the size of the primary particles. The primary particle size can be adjusted by the

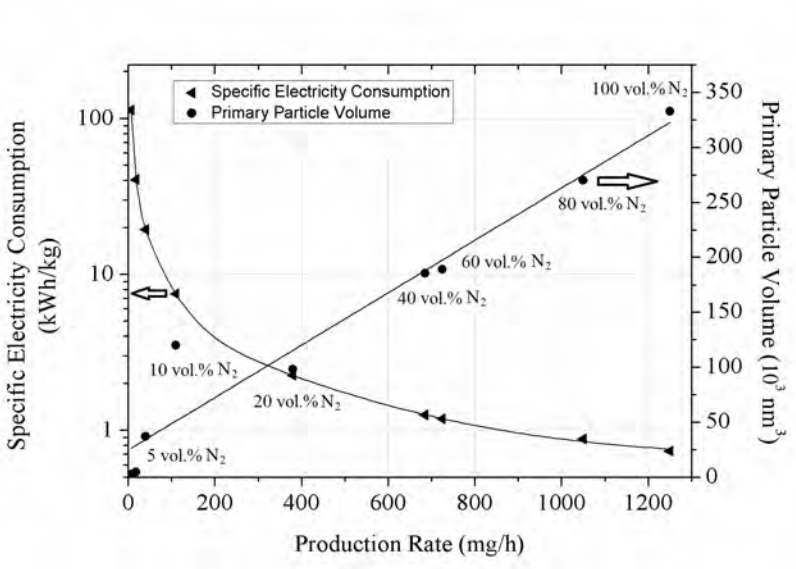

Figure 4.20: *Specific electricity consumption and primary particle volume for different production rates (CD 6, $Q_1 = 20$ l/min) [145]*

carrier gas composition in the range 15 to 80 nm. Between the 100 vol.% and the 20 vol.% nitrogen mixture the primary particle size decreases linearly with ca. 4 nm / 10 vol.%. The particle size decreases significantly at higher argon concentrations (nitrogen $<$ 20 vol.%). Therefore, argon –nitrogen gas mixtures can be used, when a specific particle size is desired. The specific electricity consumption decreases with the nitrogen concentration and thereby with the increasing production rate, although the voltage and thereby the power input is increased when nitrogen is added into the system.

To conclude it can be said that the carrier gas composition has a large impact on the particle production rate and can increase it with orders of magnitude. This increase is observed for all investigated metals. In argon and helium, the evaporation rate increases, when metals with a higher vapor pressure are used. In the nitrogen arc, copper particle production exceeds the one of silver, although the vapor pressure of copper is lower. This appears to be a consequence of the formation of small nitrogen bubbles in the molten feedstock, which impacts feedstock evaporation significantly. The addition of hydrogen to the nitrogen carrier gas does not lead to an increase of production rate, since the bubble formation is reduced for hydrogen, due to the faster hydrogen diffusion in the molten feedstock. For metals not forming nitrides, the nitrogen arc is by far the most energy-efficient process. The increase in production rate is mostly due to an increase of primary particle size, which again makes it to a limiting

factor of the production rate. The variation of carrier gas composition allows hence also a precise adjustment of primary particle size.

4.4 Influence of power input and gas flow on production rate and particle size

The power input has traditionally been used as a controlling parameter for material evaporation in transferred arc synthesis [14, 101, 163]. This effect is also visible in the nanoparticle production rate (figure 4.21), since it increases strongly with power input above a threshold value. For silver e.g., there is a minimum power input of 175 W required to start feedstock evaporation and particle formation. The higher the power of the arc, the more energy is directed to the anode and hence to the material to be evaporated. While a higher energy input increases the temperature and thereby the evaporation of material and so the particle production rate, it as well increases the energy costs for the system.

Figure 4.22 displays the dependency of the arc voltage and the power input on the applied current and electrode distance. The power input is calculated from the product of the applied electric current and the resulting voltage between the electrodes. The required voltage for a stable arc decreases slightly with increasing current and increases with the electrode distance as predicted by the Paschen's law (for breakthrough voltage).

The investigation of the previous section shows that a nitrogen arc has a significant higher production rate than the other investigated arcs. Therefore, for non-nitride forming metals, nitrogen is used for the investigation of the influence of the power input and gas flow on the particle production rate. For other metals argon is used instead.

Figure 4.23 depicts the influence of the applied electric current on the production rate for the different metals, using CD 6. In principal it can be concluded that a higher electric current leads to an increased production rate. This increase levels of at higher currents, at which a further increase in electric current does not promote an increase in production rate. The production rate is strongly material dependent, the responsible parameter for that however is difficult to determine, as it is at least not only dependent of the materials' vapor pressure. Other effects, such as thermal or electrical conductivity, heat flux or bubble formation can affect the production rate (see previous section). Of all investigated metals, zinc has the highest production rate, owned to its high vapor pressure. In nitrogen a production rate >30 g/h has been observed at 45 A. The production rate is increased by a factor of approximately 70, by raising the applied current from 5 A to 45 A. The only other metal which reaches the mark of 1 g/h with this setup is copper. At 45 A nearly 2.2 g/h of copper nanoparticles are produced in nitrogen. The increase of production rate in dependency

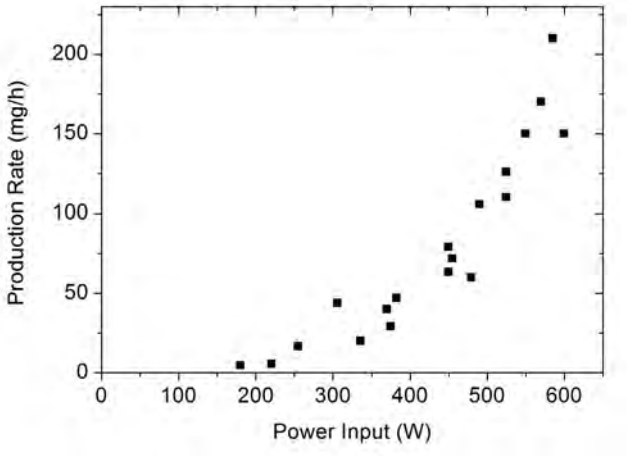

Figure 4.21: *Production rate of silver nanoparticles as a function of power input at an electrode distance of 7 mm (CD 3, Q_1 =10 l/min)*

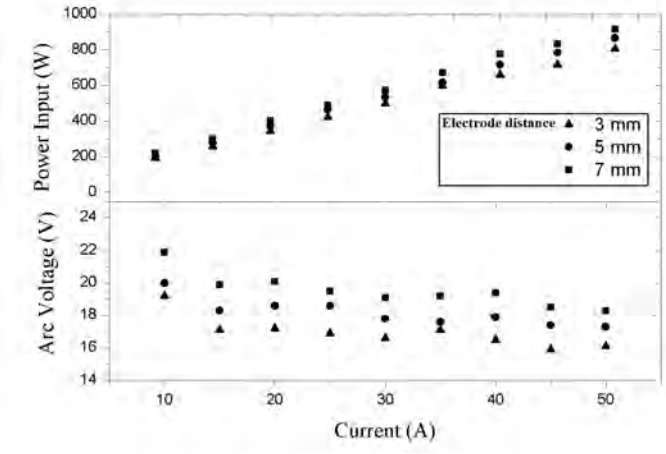

Figure 4.22: *Dependence of arc voltage and power input on applied electric current and electrode gap distance (voltage) with copper electrodes (CD 3, Q_2 =5 l/min, nitrogen) [145]*

of the current is in comparison to zinc not that strong. It is again material dependent.

The increase of production rate with current is for silver and aluminium the least significant. The maximum production rate of silver is determined to be around 0.4 g/h, even at 65 A, which is a maximum limit of applied current for the OSU setup, due to the strong heat development. Aluminium is known to form nitrides. Hence, argon is used as carrier gas for aluminium synthesis. At 65 A the maximum attainable production rate is about 20 mg/h. If nitrogen is used and aluminium nitride formed, the production rate increases approximately by a factor 10. The dependency of the current stays nearly the same. FeCr shows strong dependency on the current, its production rate nevertheless is the lowest of all investigated metals. As already mentioned in the previous section (Figure 4.15), the feedstock composition of FeCr can not be transformed 1:1 into aerosol particles, as the produced particle consist mostly of chromium (66 vol.%).

Figure 4.24 shows the specific electricity consumption. Except for zinc, the specific electricity consumption behaves linearly for all metals over the applied electric current, which proves that beside the carrier gas composition the applied electric current is a very important parameter to affect and control the production rate. In the investigated power range, an increase in power (electric current) leads to an increase in production rate, so that the efficiency of the process stays constant, even for higher production rates. Only zinc shows a nonlinear behavior, which can be reasoned by its strong evaporation above 5 A. At 45 A a specific electricity consumption of 25 kWh/kg is observed for zinc.

As the specific power consumption behaves almost linearly for the other metals in the investigated power range, it appears that the production of nanoparticles by this method can be increased arbitrarily by just supplying more power to the process. Figure 4.25 shows the primary particle size for zinc, copper, silver and aluminium according to the production rate and specific electricity consumption. The biggest particles are produced with zinc, due to its strong evaporation. The particle size ranges depending on the input current between 78 and 220 nm. Silver particles are produced in a size range of 76 to 144 nm, copper particles between 48 and 112 nm. The particle sizes of aluminium are much smaller, as they are produced with argon as carrier gas. It is remarkable that silver exceeds the particle size of copper, although the production rate is much higher for copper than for silver. This might be consequence of the rapid sintering of silver even at low temperatures, which favors the formation of bigger particles and less agglomerates. However, the primary particle size increases with the applied electric current for all metals, eventually exceeding the size of 100 nm (not for aluminium). The point of exceedance of this limiting value is of course material dependent. It means that by definition no longer nanoparticles are produced, according to ISO/TS 27687:2008. Hence, an in-

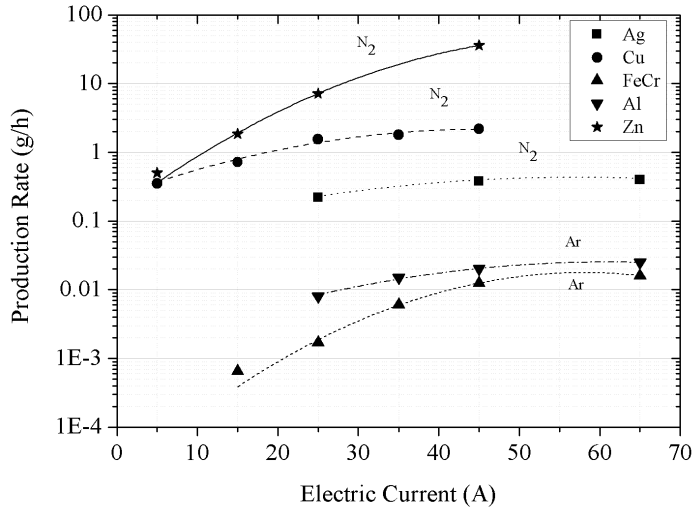

Figure 4.23: *Production rate of different metals in dependence of the applied electric current (CD 6, $Q_1 = 20$ l/min)*

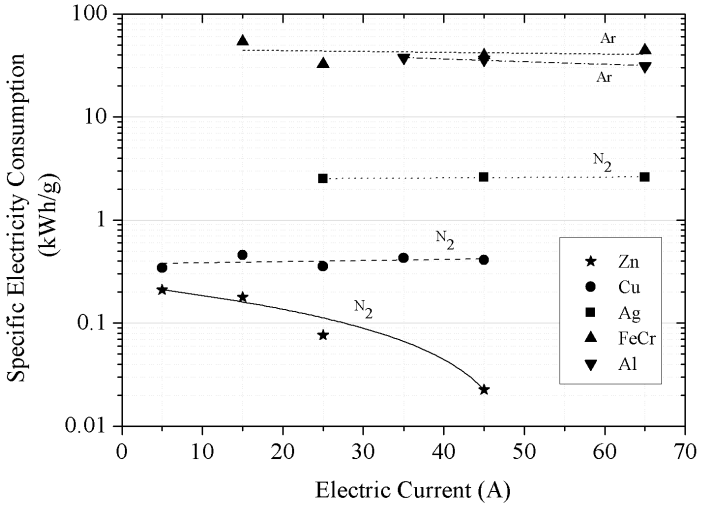

Figure 4.24: *Specific electricity consumption of different metals in dependence of the applied electric current (CD 6, Q_1=20 l/min)*

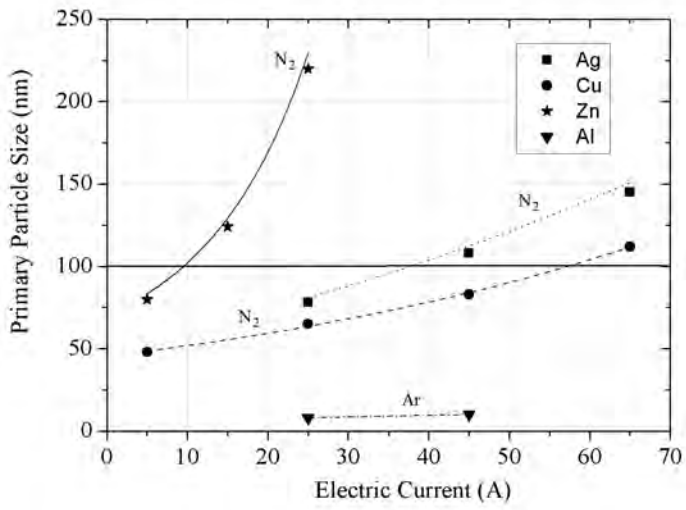

Figure 4.25: *Primary particle size of different metals in dependence of the applied electric current (CD 6, Q_1=20 l/min)*

crease in production rate by simply increasing the power input has an inherent limitation.

The knowledge of the primary particle sizes allows furthermore an estimation of the electricity consumption per surface area of nanopowder and not the production rate. This is depicted in figure 4.26. The electricity consumption per surface area is for zinc, copper and even aluminium for smaller power inputs in the same range (10 to 30 Wh/m^2). The surface area of the small aluminium particles is much larger than the one of zinc, which equalizes the increased specific electricity consumption. The electricity consumption per surface area for silver is much higher than for any other metal, which results from the ratio of a relatively large particle size and low production rate.

Further optimization of production rate in the nanoscale size range can be realized by the amount and direction of the gas flow, including CD 7. Figure 4.27 depicts the influence of the amount and direction of the gas flow on the production rate and primary particle size for copper particles at 35 A. It shows that the production rate increases with the carrier gas flow Q_1. An explanation of this is that at higher gas flows, a more efficient transport of particles out of the formation zone occurs. Also particle losses in the lines are decreased extensively at higher gas flows. Nevertheless, a volume flow higher than 40 l/min is not advisable due to instabilities of the arc and increased gas consumption.

The second (cross) flow Q_2 is also beneficial in terms of production rate. By adding 3 l/min (solid line, figure 4.27) from the side, the production rate

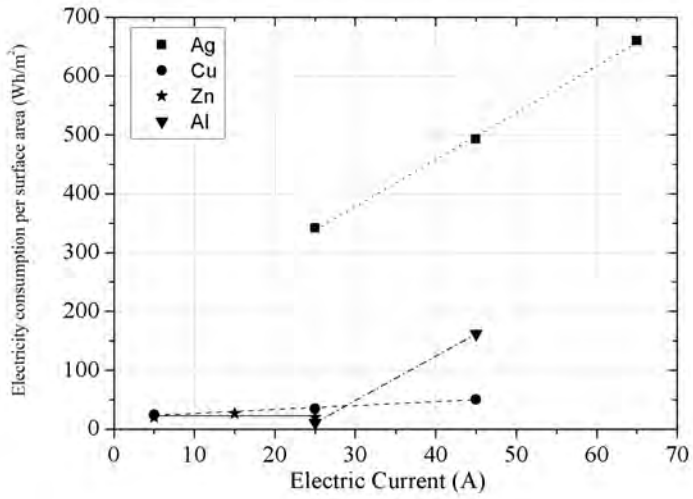

Figure 4.26: *Electricity consumption per surface area in dependence of the applied electric current (CD 6, Q_1=20 l/min)*

can be increased about 1 g/h ($Q_1 = 40$ l/min), to a value of approximately 5.5 g/h. Is the cross flow Q_2 increased further (dotted line) the production rate decreases significantly. On the one hand the arc gets unstable at a cross flow $\geqq 5$ l/min so that the production process is quite discontinuous. On the other hand, much smaller particles are formed at this flow. The particle size decreases significantly with the cross flow Q_2, as it directly influences the residence time in the nucleation and coagulation zone. The higher the flow, the smaller is the residence time and hence the resulting particle size.

Principally one can adjust the primary particles size of the copper nanoparticles in the range from 60 to 130 nm by varying the nitrogen gas flow. In order to reach the maximal production rate of metal nanoparticles, a main carrier gas flow Q_1 as high as possible and a cross flow Q_2 at about 3 l/min appear to be optimal.

Table 4.2 summarizes the optimal parameters to produce metal nanoparticles with the OSU in larger amounts keeping the particle size below 100 nm (except for zinc). The applied parameters are strongly material and carrier gas dependent. For most metals, CD7 appears to be the best in terms of production rate, which might be a consequence of the higher carrier gas flows, which can be used with this setup. The mass load per cubic centimeter stays almost constant, when the gas flow is doubled, but the particle size decreases. For aluminium and FeCr, basically the argon arcs with CD 6 seem to be most promising. The production rate is due to the use of argon in comparison to the other metals comparatively low. A further increase in gas flow does not lead to an increased

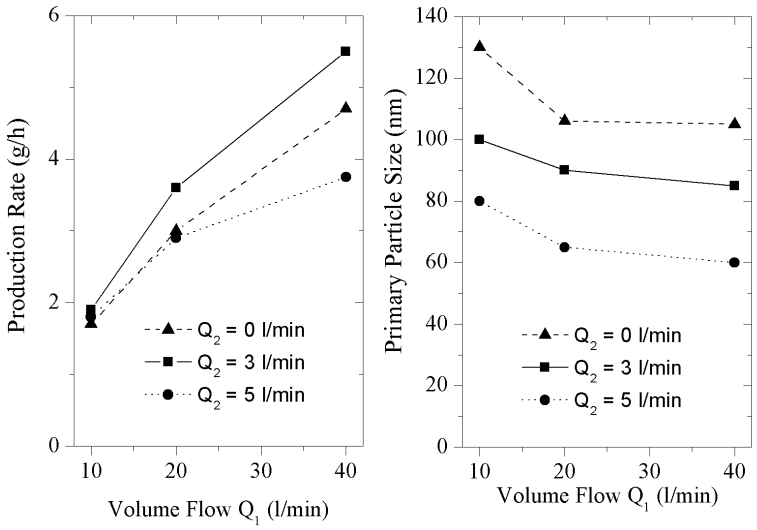

Figure 4.27: *Influence of amount and direction of gas flow on production rate (left) and particle size (right) at 35A (CD 7)*

production rate. In comparison to CD 7, CD 6 shows slightly decreased particle losses to the reactor walls and is hence preferred for metals with lower production rates. A cross flow Q_2 is advantageous for the synthesis with CD 7. At a value of 3 l/min the arc remains stable, while significant smaller particles can be produced. The particle size of in argon produced particles is much smaller, so that an additional decrease of particle size is not required. As discussed before, the applied electric current impacts the production rate and hence particle size strongly, which means that the highest current is not automatically the optimal process condition. The evaporation rate of copper and zinc are very high even at lower currents. An increase in current might lead to a marginal increase in evaporation and production rate, but is not beneficial in terms of electricity consumption and particle size. Due to the heat development at higher currents a maximum current value of 60 A has been set. The purity and composition of produced particles is shown by the XRD measurements depicted in figure 4.15.

Table 4.2: *Optimal parameters for nanoparticle production with the OSU*

Metal	Carrier Gas	CD	Q_1(l/min)	Q_2(l/min)	Elect. Current (A)
Zn	N_2	7	40	3	25
Cu	N_2	7	40	3	35
Ag	N_2	7	40	3	60
Al	Ar	6	20	0	60
FeCr	Ar	6	20	0	60

Table 4.3: *Production rate (PR), specific electricity consumption (SEC), mobility size d_m (agglomerates) and primary particle size d_P (BET) of the different metals achieved with the optimal parameters*

Metal	PR (g/h)	SEC (kWh/kg)	d_m(nm)	d_P(nm)
Zinc	36	12	212	180
Copper	5.5	179	144	83
Silver	1.0	6807	128	120
Aluminium	0.03	32025	65	15
FeCr	0.02	41017	63	18

Table 4.3 shows the production rate, specific electricity consumption, mobility size (agglomerates) and primary particle size (BET) of the different metals achieved with the optimal parameters of table 4.2. Due to its vapor pressure, zinc is the material with the highest production rate and hence lowest specific electricity consumption. More than 30 g/h of zinc nanoparticles with a mean primary particle size of 180 nm can be produced. By the techniques discussed before, the particle size can be reduced, but at the expense of decreased production rate. Copper nanopowder with a mean primary particle size of 83 nm can be produced with a rate of 5.5 g/h. The specific electricity consumption of copper production is approx. 180 kWh / kg. The maximum realized production rate of silver has been approx. 1 g/h with a particle size of 120 nm. The particle size at this production rate seems rather large, especially when compared to the values of copper. Also, the mobility size of the produced silver agglomerates does almost not differ from the primary particle size, which indicates the formation of very dense agglomerates consisting of only few, but larger particles due to sintering (discussed in the following chapter). The production rates of aluminium and FeCr are low, because argon has been used. The production rates are in the milligram range (30 mg/h for aluminium, 20 mg/h for FeCr and chromium). The specific electricity consumption are hence significantly higher than the ones produced by a the nitrogen arc. But, the particle sizes are very small, which makes this synthesis procedure relevant for some applications even at this low production rates.

To conclude it can be said that the applied electric current and gas flow adjustment has a marked influence on particle size and production rate. The production rate and particle size increase with the applied electric current and are thereby controllable, which can be explained by an increase of arc power, anode region temperature and hence stronger material evaporation. The increase in particle size is the limiting factor, when increasing the production rate by input power. The gas flow adjustment allows a direct manipulation of the residence time in the formation zone and is therefore a key parameter when producing metal nanoparticles via the transferred arc.

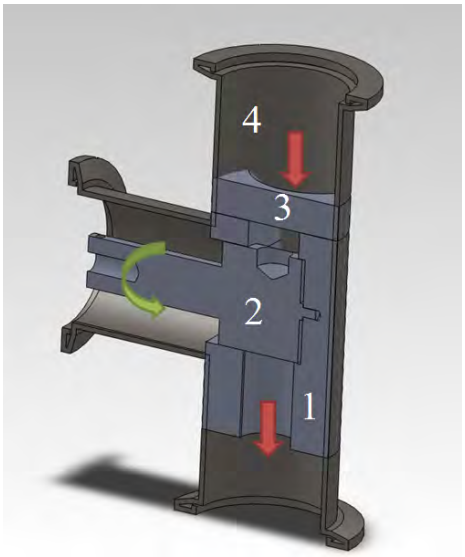

Figure 4.28: *Electrically controlled shot feeder*

4.5 Long term process stability including crucible feeding

All investigations in the previous sections have been done with the goal of enhancing the synthesis process in terms of production rate and particle properties. The process development however deals not only with enhancing the quality and quantity of the product, but has to ensure that the process can be maintained energy- and cost-efficient. This requires to keep the system running as long as possible with the minimal possible number of interruptions and man hours. This section concentrates on the long term stability of the process, including the development of a dedicated crucible feeding mechanism, which fills the evaporated amount of metal back into the crucible.

All long term measurements are performed with CD 7. The main limitation for the long term synthesis is the limited amount of initial feedstock material in the crucible. The arc extinguishes and hence the synthesis stops, when no more material is left in the crucible. Therefore fresh material has to be fed, which can be done through the guiding funnel and hood, which is arranged above the crucible (Figure 4.11). Different feeding mechanisms have been applied, all based on the same principle of feeding material into the crucible from the top using gravity. The final design is depicted in figure 4.28. It is an electrically controlled feeder. An electric motor drives a cylinder, with a small drill inside. While the drill is filled with shots on the reservoir side, it is emptied on the other side, where shots drop into the crucible.

The feeder is designed to refill the crucible with bulk metal with minimal vacuum leakage. Therefore it is integrated into standard ISO-KF 40 flanges,

Table 4.4: *Evaporation rates of the different metals for different applied electric currents (Optimal flow setting)*

Current (A)	Evaporation rate (g/h)				
	Zinc	Copper	Silver	Aluminium	Steel
5	6.6	-	-	-	-
15	-	6.2	1.6	-	0.008
25	52	-	-	-	-
35	-	16.7	3.4	0.032	0.031
45	161	-	-	-	-
60	-	20.2	7.2	0.120	0.110

which guarantee full vacuum capability at minimal costs. It is also designed to prevent wedging of feeding material inside the mechanism and therefore can be used with a variety of forms and shapes of feedstock materials. Typically shots of the desired metal with sizes of 1-2 mm are used. The center of the feeder is an aluminium cylinder (1) positioned in the middle of a T-flange. A hole is drilled into its side that serves as a bearing for a rotating cylindrical shaft (2) made of steel. A circular plate with a chamfered hole on its edge (3) is mounted on top of the main cylinder. The space above it serves as a reservoir for the feedstock metal (4). The hole is directing the material to the left of the shaft. As it spins, the material is lifted over the shaft, where its guided to the bottom of the main cylinder and exits the feeding mechanism to the direction of the crucible. The size of the chamfered hole can be adjusted by spinning the circular plate and thereby reduces the mass fed during one impulse.

The mechanism is driven by a 12 V electrical motor (DC geared motor 1:516 IG320516-41C01, Shayang Ye Industrial Co., Taiwan) that is wired via an electrical vacuum feedthrough to the outside. It runs with a rotation speed of 11.2 rpm. The motor shaft is plugged into a drill at the end of the cylindrical shaft and secured with a screw. The motor is screwed onto a circular plate, which can be adjusted similar to an O-ring. Additional holes are drilled into the plate to enable easy evacuation of the ISO-KF 40 tube that is used as the motor housing.

By this method, the feed amount is given by the volume of the reservoir and number of rotations, which is adjusted to the evaporation rate of the material. To variate the mass flow fed by the mechanism, the motor's power supply is regulated by a timer (VM188, Velleman, Belgium). The impulse for feeding and pausing can be set in a range from 1 s to 60 h. Here, the feeding mechanism is operated at a constant level according to the evaporation rate, but can also be controlled by means of a suitable signal proportional to the evaporation rate.

Table 4.4 summarizes the evaporation rates of the different metals at different parameters, after which the feeding mechanism is adjusted. As expected, the evaporation rate is strongly material- and process-dependent (applied electric

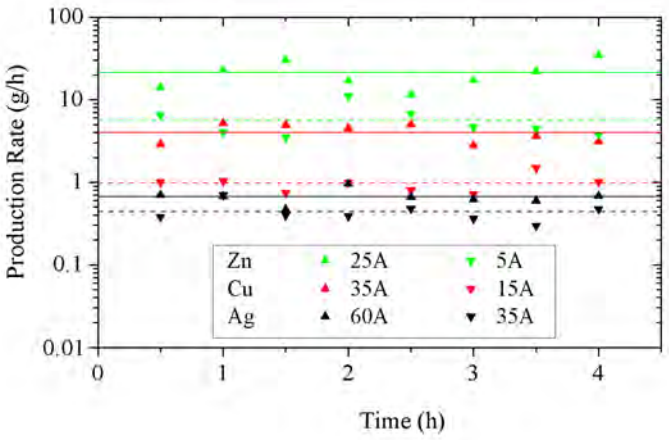

Figure 4.29: *Production rate over time (Optimal conditions)*

current). Principally one can conclude that the evaporation rate is approximately 2 to 10 times higher than the production rate for all metals (compare to table 4.3), which is due to particle losses at the reactor walls or process lines. This material can also be collected and used as "Quality B" powder. The evaporation rate is the highest for zinc even at lower currents. Its feeding rate needs therefore to be much higher than the one of copper and silver, respectively. Is the evaporated amount filled into the crucible, the OSU is able to produce high amounts of material over extended time.

The production rate of the different metals over a time span of 4 hours at different electric currents, determined by gravimetric measurement, is plotted in figure 4.29. Each measurement is performed every 30 minutes over an interval of 90 seconds. As can be seen, the production rate maintains constant over the time span of 4h. The measurement has been stopped after this time as no problems occur, longer runs are without any problems feasible. BET measurements show constant values of primary particle sizes over the 4 hour time span, which are close to the determined values of the short time measurement.

The mean production rates over time differ from the maximum values determined in the previous section. The mean production rate of copper over time at the optimal parameters is with 4 g/h almost 28% below the maximum production rate. This might be a consequence of measurement errors including small variation in gap distances during measurement as feeding is not constantly. In total however, the frequent feeding of material results in a constant level of feedstock melt inside the crucible and hence the realization of the long term running.

Chapter 5

Online and ex-situ determination of primary particle size in transferred arc synthesis

The synthesis of metal nanoparticles by means of the OSU is described in the previous chapter. The OSU allows producing metal nanoparticles of different particle sizes, forming agglomerates of different extent of aggregation. The particle properties can be adjusted depending on the desired product or application. In order to validate the particle properties, it is very important to determine the particle sizes correctly. Until this point, particle characterization has been done by commercial characterization methods. The primary particle size has been determined by offline methods, e.g. XRD, BET measurement or electron microscopy. Although these characterization methods are accurate, they are offline methods and measure therefore nanoparticles synthesized over a longer period of time. Since the transferred arc synthesis is a more fluctuating synthesis method in comparison to furnace or flame synthesis, alternating particle sizes might result from changing process conditions, e.g. due to an increasing arc gap with time. Such information cannot be delivered by offline methods. Hence, information and online monitoring of primary particle size as well as the evolution of particles during formation is desirable. In this chapter two approaches are presented, one measures the primary particle size online at the end of the process and another one monitors the particle size evolution ex-situ. Parts of this chapter have been published separately [145].

5.1 Online determination of primary particle size

Online monitoring of the synthesized aerosol is performed classically by means of a SMPS or ELPI. The SMPS e.g. determines number size distributions

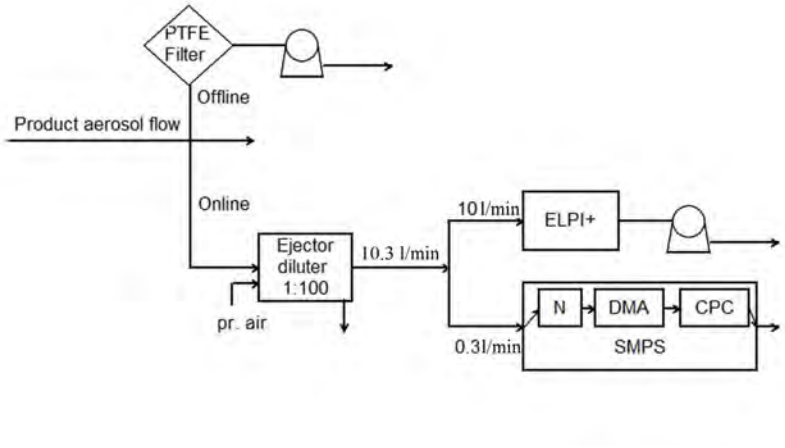

Figure 5.1: *Characterization setup*

based on the mobility diameter, which closer relate to the agglomerate size than the primary particle size, especially for high-intensity arc synthesis. Generally, online methods to determine particle size information are well known [107]. A large number of studies have been performed on aerosols by SMPS [124], ELPI [75] and TEOM [134]. A combination of those devices has been used to obtain detailed information about aerosol characteristics such as mass load, effective density or mass mobility exponent of the agglomerates [13,50,129,130,154,155].

In this section, a fast online characterization system based on parallel SMPS and ELPI measurement is used. A simple approach is developed to estimate the effective density and thereby the primary particle size, based on an assumed mass mobility exponent. Afterwards, a direct relation between effective density and mass mobility exponent is suggested on the basis of a comparison with BET measurements, which gives the opportunity of estimating the primary particle size directly. Hence, an online aerosol measurement platform is created leading to a fast, but detailed primary particle size measurement. This is desirable especially when it comes to scaling up the production process of nanoparticles, in which slowly changing process conditions can occur.

5.1.1 Experimental setup and procedure of the online measurement technique

Figure 5.1 shows the characterization setup used to determine the aerosols' attributes. Copper nanoparticles are used for this investigation, which are produced by the OSU with CD 6. Two aerosol flows for characterization are extracted from the product flow leaving the OSU. One aerosol flow is used for filter deposition and offline characterization, the other one for online character-

ization. For offline characterization, particles are deposited on a PTFE filter with a pore size of 5 µm. With time, a cake of copper nanoparticles is formed on the filter, which is removed mechanically. The collected powder is used for BET measurements in order to determine the primary particle size of the synthesized particles offline. All BET samples are degassed at 120°C for at least 8 h prior to the measurement. Afterwards TEM measurements are performed to confirm the achieved results. For the online characterization a dilution system (VKL 100, Palas GmbH, Karlsruhe, Germany) is required, as the number concentration of particles in the product flow is too high for measurements with a CPC and the electrometers in the ELPI. The dilution with a factor 100 is also necessary to stop further coagulation in the characterization lines. To dilute the aerosol, a part of the product flow is sampled into the dilution system as a result of the reduced pressure created in an ejector and diluted with the ejector gas. A total flow of 10.3 l/min of mixed ejector gas and aerosol is then led to the online measurement devices.

In order to determine the primary particle size online, the number size distribution of the aerosol is measured with the SMPS and ELPI in parallel. An SMPS system is used to measure the aerosol size distribution based on the equivalent mobility diameter. The ELPI measures the aerosol size distribution based on the aerodynamic or Stokes diameter (see chapter 3.2.1).

Determination of the primary particle size is done on the basis of the measurement of the effective density by parallel size distribution measurements by ELPI and SMPS [129, 155]. The effective density ρ_{eff} is the parameter resulting in the same aerodynamic and mobility diameter for agglomerates with the same Stokes number. The standard analysis software of the ELPI is used, which already contains an automatic correction for charging probability and small particle losses [105]. The SMPS data including diffusion correction and correction of charging probability is added. In order to reach an appropriate fit, the width of the SMPS distribution columns displaying $\mathrm{d}N_{\mathrm{SMPS}S_i}/\mathrm{d}log(d_{\mathrm{m}})$ is adjusted to the ones of the ELPI $\mathrm{d}N_{\mathrm{SMPS}S_i}/\mathrm{d}log(d_{\mathrm{S}})$. For the i-th size channel $i_1 : d_{\mathrm{m}} > d_{\mathrm{S1}}(\rho_{\mathrm{eff}})$ and $i_2 : d_{\mathrm{m}} \leq d_{\mathrm{S1}}(\rho_{\mathrm{eff}})$ follows:

$$\frac{\mathrm{d}N_{\mathrm{SMPS}S_i}}{\mathrm{d}\log(d_{\mathrm{s,i}})} = \frac{\sum_{i_1}^{i_2} \mathrm{d}N_{\mathrm{SMPS}}(d_{\mathrm{m},i})}{\log(d_{\mathrm{S2},i}(\rho_{\mathrm{eff}})) - \log(d_{\mathrm{S1},i}(\rho_{\mathrm{eff}}))} \tag{5.1}$$

with d_{m} being the mobility diameter, d_{S2} the maximum and d_{S1} the minimum Stokes diameter of the i-th ELPI channel.

Next, the effective density ρ_{eff} (changing the position of the particle size distribution) and a factor a (adjusting the total number concentration of the ELPI and SMPS to similar values) is varied until the mean error square between the Stokes diameter size distribution $\mathrm{d}N_{\mathrm{ELPI}}/\mathrm{d}\log(d_{\mathrm{S}})$ and the mobility diameter

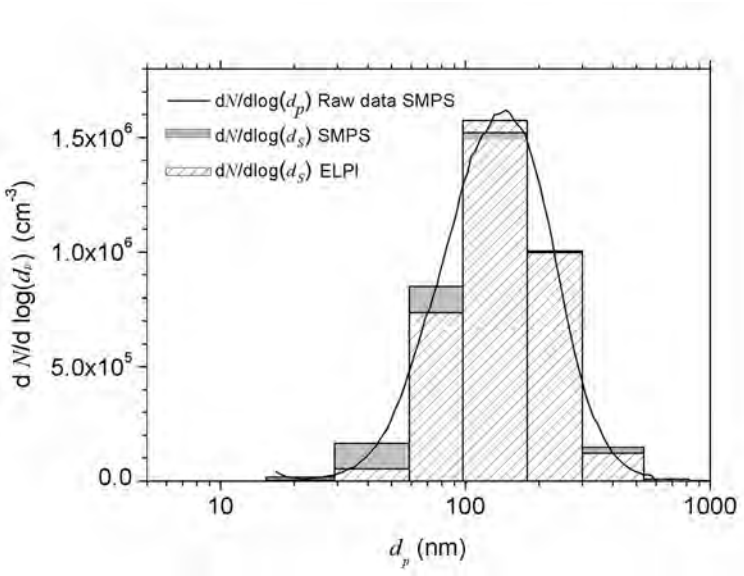

Figure 5.2: *Example of a size distribution fit of ELPI and SMPS measurement in order to determine the effective density based on the Stokes diameter (10 vol.% N2, 10 slm, 25A) [145]*

size distribution $\mathrm{d}N_{\mathrm{SMPS}}/\mathrm{d}log(d_{\mathrm{s}})$ is minimized and the ELPI distribution fits the one of the adjusted SMPS:

$$\mathrm{Error} = \sum_{i=1}^{i_{max}} \left[\left(\frac{\mathrm{d}N_{\mathrm{SMPS}}}{\mathrm{d}\log(d_{\mathrm{s}}(\rho_{\mathrm{eff}}))} \right) - a \left(\frac{\mathrm{d}N_{\mathrm{ELPI}}(\rho_{\mathrm{eff}})}{\mathrm{d}\log(d_{\mathrm{s}}(\rho_{\mathrm{eff}}))} \right) \right]^2 \tag{5.2}$$

with $0 < \rho_{\mathrm{eff}} < \rho_{\mathrm{bulk}}$ and $0.2 < a < 1$.

Here, the highest possible effective density is set to the bulk density. Figure 5.2 shows a resulting size distribution fit. It can be seen that the fit of the two distributions matches well. An estimation of the primary particle size can then be done with the determined effective density.

The mobility diameter of fractal agglomerates can be calculated as [144]:

$$d_{\mathrm{m}} = d_{\mathrm{p}} n_{\mathrm{p}}^{\frac{1}{D_{fm}}} \tag{5.3}$$

d_{p} is the primary particle diameter, n_{p} the number of primary particles in the agglomerate and D_{fm} the mass mobility exponent.

The agglomerate mass is calculated with:

$$m_{\mathrm{aggl}} = \frac{\pi}{6} d_{\mathrm{m}}^3 \rho_{\mathrm{eff}} = n_{\mathrm{p}} \frac{\pi}{6} d_{\mathrm{p}}^3 \rho_{\mathrm{b}} \tag{5.4}$$

where m_{aggl} is the agglomerate mass. The primary particle size can be determined on the basis of equation 5.4 with the effective density resulting from the combined ELPI-SMPS fit:

$$d_{\mathrm{p}} = d_{\mathrm{m}} \left(\frac{\rho_{\mathrm{eff}}}{\rho_{\mathrm{bulk}}} \right)^{\frac{1}{3-D_{fm}}} \tag{5.5}$$

This estimation is valid for all n_{p} in the free molecular regime and for $n_{\mathrm{p}} < 100$ in the continuum regime [144]. Since $n_{\mathrm{p}} > 100$ has never been observed in the present setup for bigger particles, the estimation should be valid in the present process. The only unknown parameter beside the primary particle size in equation 5.5 is the mass mobility exponent D_{fm}, when the effective density is determined. Therefore the primary particle size is determined for different assumed D_{fm} and compared with BET measurements in order to determine D_{fm}.

5.1.2 Results of the online size determination

As shown in the previous chapter, agglomerates consisting of different primary particle sizes can be formed by the carrier gas composition of argon and nitrogen (see chapter 4.3, figure 4.20). Figure 5.3 shows the effective density of copper agglomerates determined by parallel ELPI and SMPS measurements for different argon/nitrogen mixtures. The effective density does not change significantly for nitrogen concentrations above 40 vol.%, but decreases strongly for lower concentrations. Since ρ_{eff} is used for the estimation of the number of primary particles per agglomerate (figure 5.4) and primary particle size (figure 5.5), a significant change over vol.% nitrogen is observable in the estimated values. Figure 5.4 depicts the predicted number of primary particles in agglomerates for different assumed mass mobility exponents. A higher value of the mass mobility exponent leads to more primary particles in the agglomerates for the same effective density. The impact of the assumed mass mobility exponent is less for higher effective densities, as the number of predicted primary particles per agglomerate differs only marginally at high nitrogen concentrations. Dense agglomerates, in which the primary particles shield each other reducing the effective drag force, have a higher mass mobility exponent. Hence, they are built of more and smaller primary particles at same effective density and mobility.

Figure 5.5 shows a comparison of the estimated primary particle size with different assumed mass mobility exponents and the experimentally found BET diameters, which might be taken as an estimation for the mean primary particle diameter. The primary particle size fits well for nitrogen concentrations below 10 vol.% and a mass mobility exponent of 2.2. In this range agglomerates with $n_{\mathrm{p}} > 5$ are formed by cluster-cluster agglomeration. A mass mobility exponent of 2.2 is common for such agglomerates [144]. However, the BET diameter at

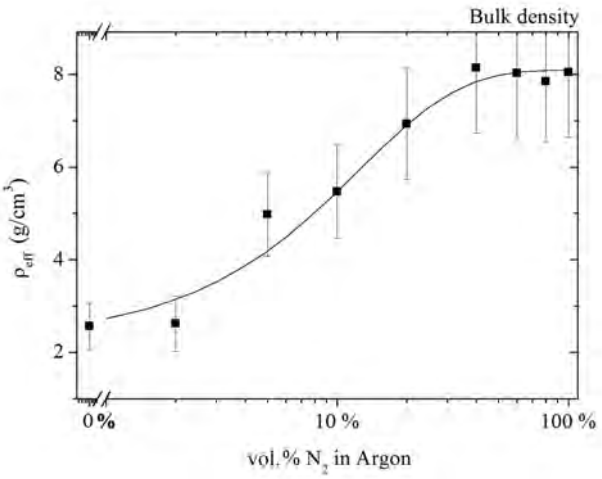

Figure 5.3: *Estimated effective density by parallel ELPI and SMPS measurements. The agglomerate structure is changed by varying the carrier gas composition from argon to nitrogen [145]*

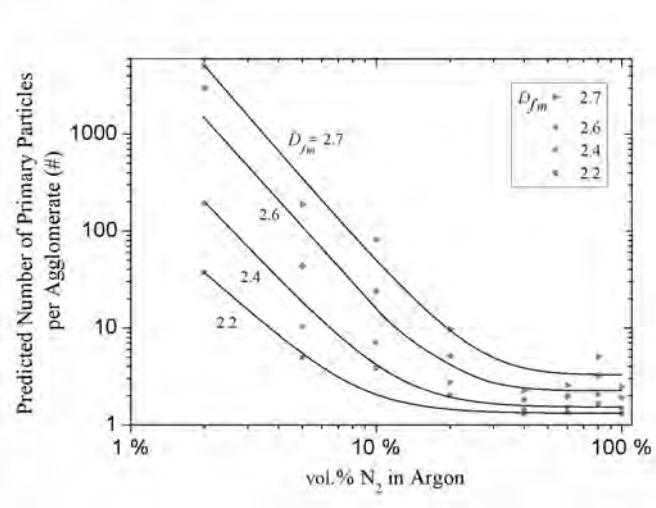

Figure 5.4: *Predicted number of primary particles per agglomerate determined from the effective density for different assumed mass mobility exponents. The solid lines are a guide to the eye [145]*

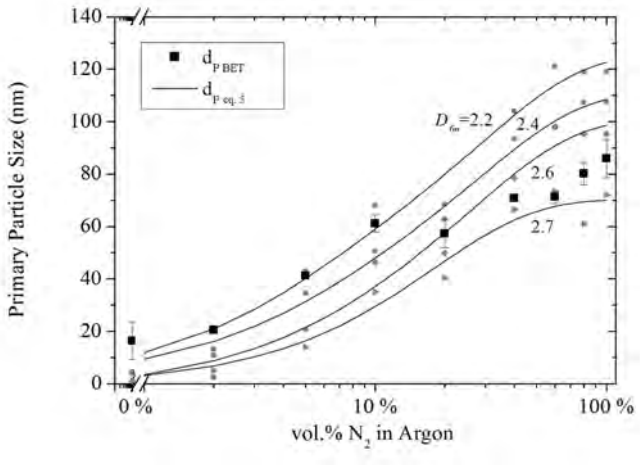

Figure 5.5: *Comparison of estimated primary particle diameter by SMPS and ELPI measurement with the experimentally found BET diameter [145]*

increased nitrogen concentration fits much better with the estimated primary particle sizes with higher values of mass mobility exponents, between 2.6 and 2.7. The arc length and width increases and develops more heat at higher nitrogen concentration. Larger and dense agglomerates, with less primary particles seem to be formed by cluster-particle or particle-particle collisions [167]. Also sintering is likely. Those agglomerates will have a higher mass mobility exponent.

Figure 5.6 shows an estimation of the mass mobility exponent based on the effective density, when assuming d_{BET} yields the primary particle size. The mass mobility exponent behaves linearly in two regimes. It stays constant below a relative density of 0.6. For higher relative densities (> 0.6) the mass mobility exponent increases (with a gradient of 2.2). At a relative density of 1 the mass mobility exponent has to be 3 by definition. Hence, the mass mobility exponent can be estimated directly, when knowing the effective density of an agglomerate by:

$$D_{fm} = \begin{cases} 2.2 & for\ \frac{\rho_{\mathrm{eff}}}{\rho_{\mathrm{bulk}}} \leq 0.63 \\ 2.2 & \frac{\rho_{\mathrm{eff}}}{\rho_{\mathrm{bulk}}} + 0.8 \text{ for } \frac{\rho_{\mathrm{eff}}}{\rho_{\mathrm{bulk}}} > 0.63 \end{cases} \tag{5.6}$$

Since the mass mobility exponent can thus be estimated by the effective density, it does not have to be assumed anymore for the primary particle size calculation. Equation 5.5 includes then only one unknown constant (ρ_{eff}), which can be determined by the parallel ELPI-SMPS measurement. Therefore, an

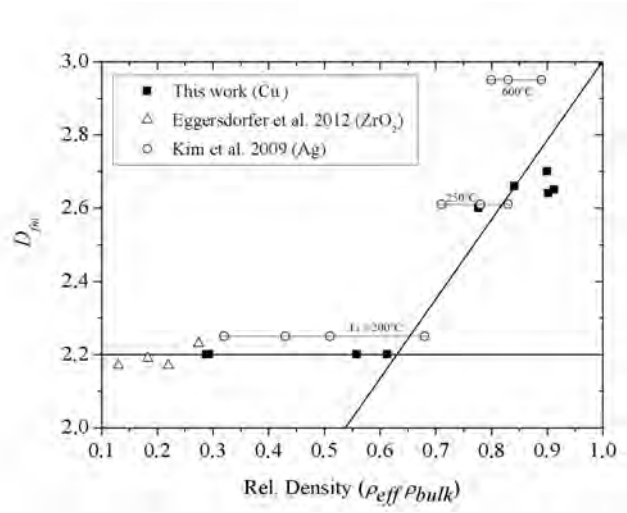

Figure 5.6: *Mass mobility exponent estimated by means of the effective density. The data of Kim et al. are shown for different sintering temperatures [31, 77, 145]*

approximate, but fast online method for the estimation of primary particle size in agglomerates is possible.

As depicted in figure 5.6, the results found in this work matches well with the determination of mass mobility exponent (fractal dimension) and effective density by other researchers in different material systems [31, 77]. The data from Kim et al. are determined at different sintering temperatures leading to partially sintered agglomerates, which increase the effective density. Stronger sintered agglomerates are known to have a higher mass mobility exponent due to the compaction and thus a better shielding of the inner particles to the gas stream. Although not shown in figure 5.6, there are other publications confirming the presented results. Maricq et al. [103], e.g., report mass mobility exponents in the range 2.2-2.35 for relative densities between 0.1 and 0.5 for soot particles. Even though not evaluated, the data show a nonlinear behavior for increased effective densities, which might result in higher mass mobility exponents. Relative densities of 0.2-0.7 and mass mobility exponents of 2.3-3 are found by Virtanen et al. [155] for silver particles. While the results fit well for small relative densities, there is a strong deviation for increasing relative densities. Already at a relative density of 0.7, a mass mobility exponent of 3 is reported, indicating quasi-spherical particles.

In order to further validate the found results TEM measurements are performed. Figure 5.7 shows TEM images of copper particles synthesized at different nitrogen concentrations. It appears that apart from the particles of the determined size (figure 5.7 a,b), also some smaller particles (approx. 10 nm) are created, which stick to the bigger particles. Those bigger particles might shield

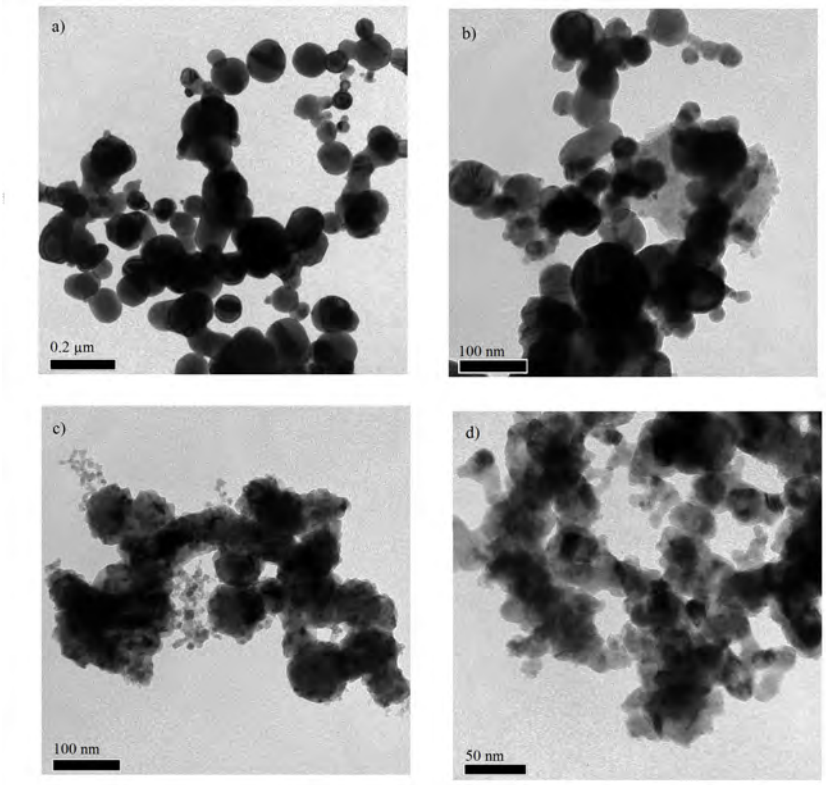

Figure 5.7: *TEM images of copper particles synthesized at different nitrogen concentrations in argon. a) 100 vol.%, b) 60 vol.%, c) 5 vol.% and d) 0 vol.%*

the smaller particles so that this agglomerate behaves more like a spherical particle than agglomerates consisting only of particles with the same size. Particles formed at lower nitrogen concentrations appear smaller and not that dense (figure 5.7 c,d). Both observations might confirm the found effective density and mass mobility exponent.

In order to validate determined particle sizes, particles have been deposited on a TEM grid by ESP and counted. More than 600 particles have been counted for determining an accurate size distribution. Figure 5.8 shows a TEM image and a particle size distribution of copper particles produced with CD 7 in 100 vol.% nitrogen. As depicted, the distribution is rather broad ($\sigma_\mathrm{g} = 1.54$). The obtained geometric mean number-based particle size ($d_\mathrm{g,n}$) is 58.9 nm. This diameter can be transformed to a surface weighted mean diameter for better comparability, which is closer related to the determined diameters:

$$d_{3,2} = 6\frac{\sum N_i \frac{\pi}{6} d_{\mathrm{p}_i}^3}{\sum N_i \pi d_{\mathrm{p}_i}^2} = 84.7\,\mathrm{nm} \tag{5.7}$$

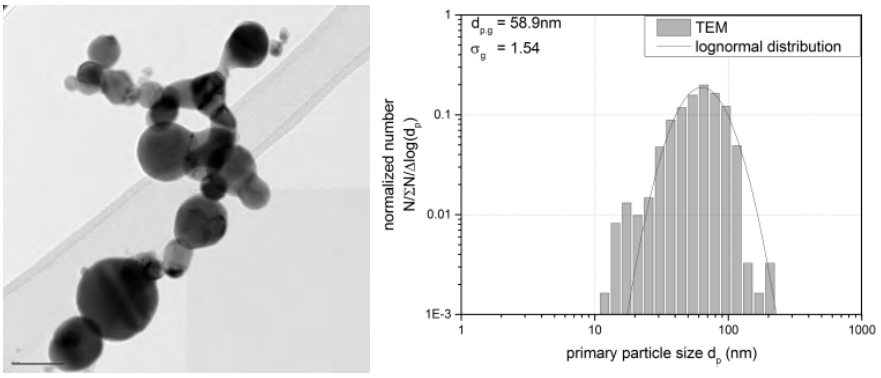

Figure 5.8: *TEM image and a particle size distribution of copper particles (CD7)*

N_i is the number of particles in a bin of the histogram distribution and $d_{\mathrm{p},i}$ is the mean number weighted diameter of the bin (i). The value of 84.7 nm compares well to the diameter obtained by the presented ELPI/SMPS method of 89 nm and the BET diameter of 86 nm.

5.2 Thermophoretic proximity sampling

Online and offline measurement techniques including the one presented in the previous section imply a preceding sampling, which refers to particle sampling beyond the process of formation and growth downstream of the process. Characterization downstream of the process is usually done as information about the final product is of interest. Nevertheless, deeper understanding of primary particle evolution during arc discharge synthesis close to or inside the formation zone is desirable.

A possibility to gain further information of the formation and growth evolution is proximity sampling close to the particle formation zone. Proximity particle sampling and characterization have mainly been used to characterize soot or flame generated particles. Two methods of proximity aerosol characterization of primary particle sizes are established: thermophoretic sampling [29] and light induced incandescence (LII) [137]. LII analyzes the enhanced thermal radiation of laser-heated particles and is applied to determine primary particle sizes in-situ during the process based on a model [109, 132, 143]. Thermophoretic sampling uses the phenomena of thermophoresis to deposit particles from a hot aerosol or flame on a cold sample surface, usually a TEM grid. An appropriate thermophoretic sampling device has been developed by Dobbins and Megaridis [29]: A piston that moves an attached TEM grid with high velocity through a hot aerosol containing flame-generated soot particles. Their technique found fur-

ther practice in numerous flame-generated particle size investigations [5, 20, 99]. Modifications of the original design by Dobbins and Megaridis have been performed in terms of protected TEM grids during insertion [65] and rapid sample insertion into the flame by a double-acting pneumatic cylinder [85]. TEM proximity sampling and LII are compared and evaluated by van der Wal et al. [153] for a flame synthesis process. They conclude that in principal both methods are capable to measure particle sizes accurately, but find that local flame temperatures affect the cooling rate of the particles and thus the optical signal of LII. Furthermore, LII is to date only for carbon well developed. This leads to the assumption that thermophoretic sampling close to the particle formation zone in arc synthesis is advantageously in comparison to LII. However, thermophoretic proximity sampling has not been used to sample particles from an arc discharge synthesis process. To transfer the technique of thermophoretic sampling to arc discharge synthesis new requirements evolve for technical performance and design of the device.

In this section, a thermophoretic proximity sampling technique that enables possibilities to acquire new insights of primary particle formation close to an arc discharge is used based on the design of Dobbins et al. [29]. The design has been adopted in order to be able to use it with closed reactors such as the OSU using vacuum components. The exposure time is claimed to be short enough for sample insertion into very hot zones such as an arc plasma without significant heating of the grid or even burning. Different TEM samples are taken by the thermophoretic proximity sampler at various positions around the arc and hence the particle formation zone. The results are evaluated regarding sampling success and particle size evolution around the formation zone. Furthermore, the obtained results are compared to online and offline measurements of particles sampled downstream of the process by BET, TEM microscopy and the previously discussed ELPI/SMPS method.

5.2.1 Experimental setup & method for thermophoretic proximity sampling

Figure 5.9 shows the experimental setup used to investigate the particle formation process ex-situ. Copper nanoparticles are used for this investigation, which are produced by the OSU with CD 7. The thermophoretic sampler (Figure 5.10) is adapted to the front of the OSU by a reduction piece from ISO-KF-160 to ISO-KF-40. It has been constructed for inserting TEM grids into the aerosol as close to the source as possible. It holds compounds of three main elements: a controlling unit, the pneumatic piston and the sample holder. The controlling unit consisting of a PLC, pneumatic actuators, power supply and proximity sensors permit to control the sampling procedure. Settable parameters of the PLC

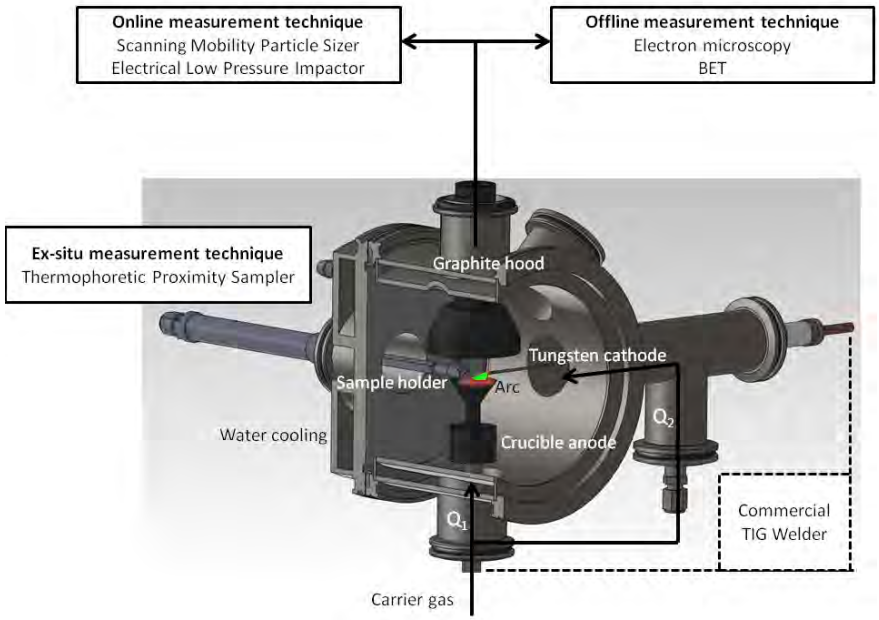

Figure 5.9: *Experimental setup for connecting the proximity sampler to the OSU*

are the sampling time and the fail safe-time. The sampling time is the time between the incoming signal that the sampler has reached its final position and the signal of retraction. It can be set between 1 and 10000 ms. The fail safe-time determines the time until the sampler is set back to its initial position, if the system could not detect the rod reaching the forward position. The controlling unit operates a pneumatic piston mounted on an ISO-KF-40 flange, which is adapted to the reactor chamber. The standard vacuum component ensures the vacuum tightness of this device, thereby not disturbing the synthesis process. In order to prevent the piston from turning during movement, the piston rod is designed as a square type. Atop of the piston rod, an L-shaped sample holder is adjusted. It allows sample taking at different position than the center at which the piston rod moves. The sample holder carries the TEM grid by pinching between two thin steel sheets. The distance from the center position (l_S) can be adjusted by the fixing length of the L-shaped holder. It can also be turned on the piston so that different angles (α_S) between TEM grid and crucible surface can be realized. The L-shaped holder has one further very important aspect. As in this study the sampling is done on particles, which are produced by electrical discharge, one has to ensure that the discharge between the two electrodes is not interrupted by the sampler. The sampler is connected to the reactor chamber, which is in direct contact with the crucible anode and hence on the same electrical potential (ground). This means that as soon as the distance between

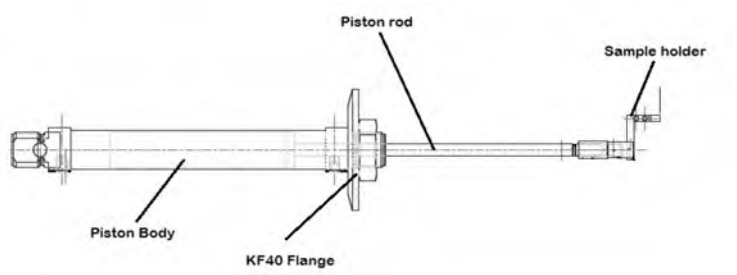

Figure 5.10: *Thermophoretic sampler*

sample holder and tungsten cathode is smaller than cathode and crucible, the arc jumps to the sample holder. The consequences would range from a burned TEM grid, to false results or even a damaged sample holder. Therefore the holder has to be arranged in a way that the distance to the cathode is always larger than the electrode gap, which can be tested prior to sampling and start of synthesis.

Once the arc is ignited and a stable production is reached, the sampler is triggered and a sample taken thermophoretically at the desired position. Thermophoretic sampling uses the phenomenon that particles are experiencing a force from the hotter side (molecule bombardment) and hence move in the direction of the "cooler" region [40]. In the free molecular regime (Kn $>>$ 1) the resulting thermophoretic velocity (x_{th}) to the sample can be calculated by [157]:

$$x_{\mathrm{th}} = \frac{0.55\eta}{\rho_{\mathrm{g}}} \nabla T \tag{5.8}$$

, where ∇T is the thermal gradient. The thermophoretic sampling is hence independent from the particle diameter. This equation becomes more complex for the continuum regime including a dependency from the particle diameter [7]. However, even when assuming a quite low arc temperature of 2000°C a Knudsen number [166] of roughly 28 indicates that the sampling is done in the free molecular regime in the present setup and is hence particle size independent. The taken samples shall therefore be deemed to be representative.

The process has to be stopped afterwards and the TEM grid taken out. The TEM grids retrieved from the procedures are analyzed by transmission electron microscopy. TEM grids consisting of a net structure are used. At least 600 particles are counted per sample. The primary particle size distribution of the sample is determined with help of a digital measurement software. The primary particles are indicated in the image by the analyzing person using an ellipse tool, which calculates the area of the ellipse. This allows calculating the primary particle diameter of each particle leading to a primary particle size distribution and a geometric mean diameter. The results are compared to determined particle

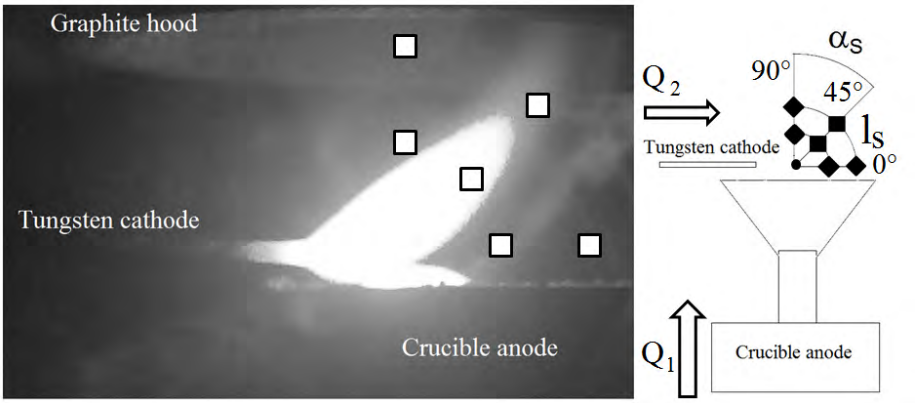

Figure 5.11: *Picture of the arc and proximity measurement points*

sizes measured on- and offline at the end of the process. In order to compare the particle sizes of the individual measurement techniques with each other, they have to be expressed with the same diameter weighting. Therefore, the surface weighted diameter is calculated based on the TEM counting with help of the specific surface area (SSA) and equation 5.7.

With this experimental setup, particle sizes and distributions are determined at seven different positions. Six of those positions are inside the reactor chamber and are investigated by the proximity sampling method. One measurement point is downstream of the reactor where the on- and offline measurement equipment is arranged. Figure 5.11 shows a picture of the arc in the presented setup for copper at 35 A in nitrogen. The shape of the arc is a combination of electromagnetic effects and buoyancy. The measurements points are chosen according to the shape of the arc. Two different distances from the center (l_S) are investigated, namely 1 and 2 cm. At both of these distances the measurement angle (α_S) is arranged between 0°, 45° and 90°. 45° is the angle, at which the sampler directly hits the arc and probably the main path of particle formation.

5.2.2 Results of thermophoretic proximity sampling

Generally one can say that the thermophoretic sampler delivered TEM samples at all investigated positions. At a sampling time of 1 ms the particle deposition on the TEM grid is found sufficient for collecting agglomerate, as well as primary particle information. Increased sampling times (5 ms) show a rather high number of particles on the TEM grid, so that agglomeration might appear on the TEM grid after deposition. At even higher sampling times (>10 ms) the TEM grid starts to get damaged. Therefore, the following results are all based on a sampling time of 1 ms.

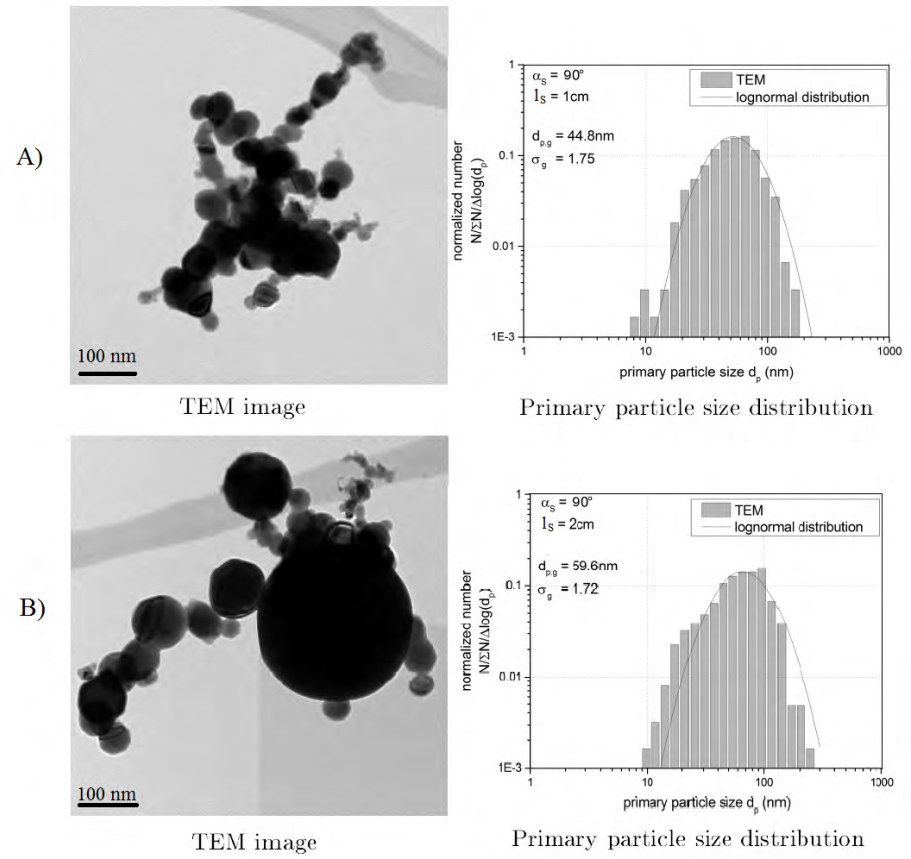

Figure 5.12: *TEM image of an exemplary agglomerate and the size distribution determined at an measurement angle $\alpha_S = 90°$ for $l_S = 1$ cm (A) and $l_S = 2$ cm (B)*

Figure 5.12 depicts a TEM image of an agglomerate and the size distribution determined at an measurement angle $\alpha_S = 90°$ for $l_S = 1$ cm (A) and $l_S = 2$ cm (B). Both distributions are rather broad ($\sigma_g \sim 1.7$), which is common for arc discharge synthesis [101]. However, the geometric mean number-based particle size at the measurement distance of 1 cm is with 44.8 nm approximately 15 nm smaller as it is at the sampling distance of 2 cm (59.6 nm). Although the particle size of 44.8 nm is rather large at the distance of 1 cm, it appears that the growth of primary particles is still not completed at that position. The effect of different particle sizes due to the measurement distance is almost negligible at a measurement angle $\alpha_S = 0°$. Here, particle sizes of 52.4 nm for $l_S = 1$ cm and 54.2 nm for $l_S = 2$ cm are found. At that angle almost no difference is found, whether the particles size is determined 1 or 2 cm away from the center position, which might be a result of the arc shape. It appears that no particle formation takes place in this direction.

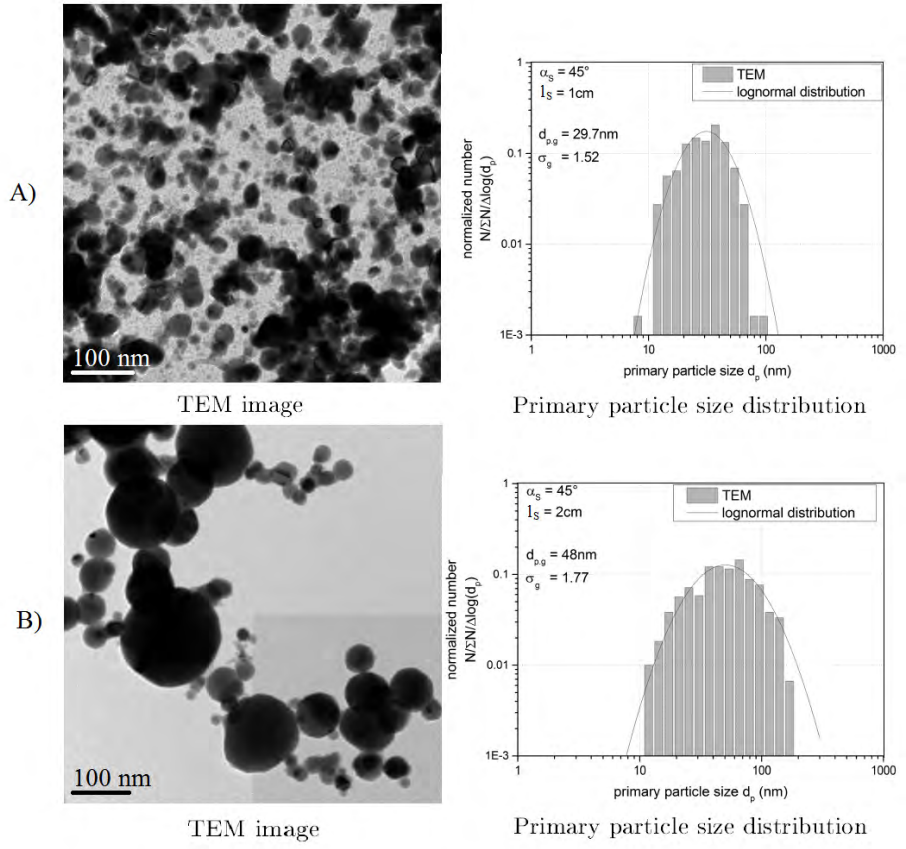

Figure 5.13: *Exemplary TEM image and size distribution determined at a measurement angleα_S = 45° for l_S = 1 cm (A) and l_S = 2 cm (B)*

This assumption is confirmed, when inspecting the result of the proximity measurement at a measurement angle of 45°, which is depicted in Figure 5.13. At a measurement distance of 1 cm the TEM images obtain a significantly increased particle loading on the TEM grid. It appears that almost no agglomeration appeared as mostly single particles are depicted. Some agglomerates are present, however due to the significant number of particles on the TEM grid it is possible that those agglomerates have formed on the grid and not in the gas phase. The particle size ranges between 8 and 88 nm leading to a geometric mean particle size of 29.7 nm, which is much smaller than all other samples. The distribution is with $\sigma_g = 1.52$ more narrow. It seems as if this sample has been exposed to a region with a high concentration of singular particles. Looking at the shape of the arc depicted in figure 5.11, this point of measurement is most likely the position closest to the arc. Higher temperatures resulting from the proximity to the arc at that position lead to a significantly decreased coalescence time in comparison to the collision time, which favors the formation of single

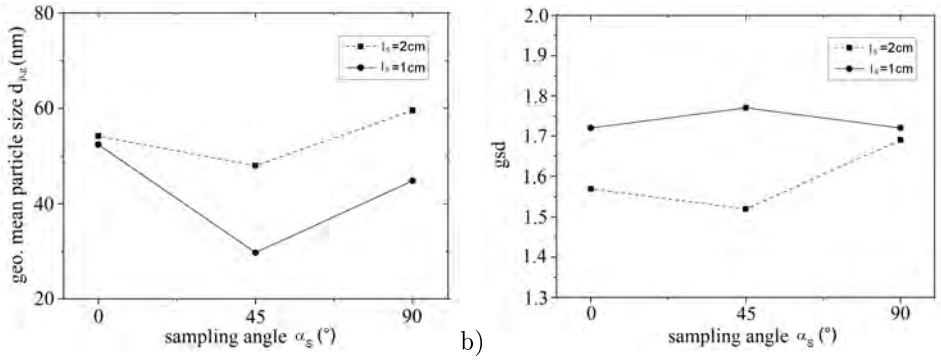

a) b)

Figure 5.14: *Geometric mean primary particle size ($d_{p,g}$) (a) and geometric standard deviation $\sigma_{p,g}$ (b) depending on sampling distance l_s and angle α_s for the proximity sampler*

spherical particles as depicted in the TEM image [82, 136]. It seems that this measurement point sampled particles during growth, without harming the TEM grid. No damages to the TEM grid are found. At a measurement distance of 2 cm the TEM image and distribution looks similar to the ones of the other measurement points. The TEM coverage is smaller and single agglomerates consisting of multiple particles are visible. The geometric mean particle size is with 48 nm considerably bigger than at the 1 cm measurement position at the same angle. Nevertheless, it is the smallest diameter in comparison to the measurement points at the same distance (2 cm) but different angles (0-90°), which again is reasoned by the shape of the arc.

Figure 5.14 shows the previously discussed results of particle size and geometric standard deviation (gsd) in relation to each other. The position of sampling has a significant influence on the particle size as well as the gsd. Principally it can be concluded that sampling closer to the arc leads to smaller particle sizes. Close to the particle formation zone, where the residence time of formed particles is short and the temperature high, growth mechanisms of condensation surface growth and coalescence are favored. The sampled particles are mostly small and singular. For an increasing distance to the arc, the residence time of formed particles is longer and thus the primary particles are grown further. At larger distances mostly agglomerates are formed, also due to the increased residence time. The distance from the arc however is not equal to the measurement distance l_S, as the measurement angle and hence the shape of the arc is crucial as well.

Figure 5.15 compares the primary particle sizes determined by the proximity sampler to the particle sizes determined by the ex-situ methods. In order to compare the results, all diameters are given as surface weighted diameter $d_{p3,2}$. By achieving primary particles of 41.9 nm to 77.5 nm at a sampling distance of

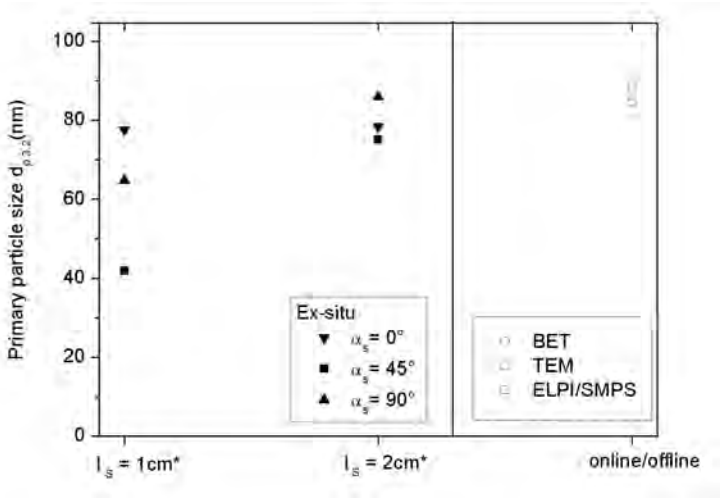

Figure 5.15: *Primary particle size depending on sampling distance (*Results obtained by thermophoretic proximity sampler)*

1 cm, it can be concluded that particles have been successfully sampled during primary particle growth. Smaller sampling distances to the arc are desirable in order to monitor the growth of particles. However, as the electrode distance is roughly 7 mm, closer collection points are difficult to achieve and take the risk of damaging the TEM grid or sampler. At a sampling distance of 2 cm, the particle sizes are almost in the same range as they are for the online/offline methods, leading to the assumption that proximity sampling has been performed late in terms of primary particle size evolution. The primary particle sizes determined by offline TEM and BET measurement go quite well along with the determination by combined online ELPI/SMPS measurement. TEM analysis leads to a primary particle size of 84.7 nm, BET measurement to 86 nm and combined ELPI/SMPS measurement to 87.5 nm at the end of the process. At a distance of 2 cm, surface weighted diameters between 75.4 nm and 84 nm have been measured. The growth of primary particles is therefore already concluded 2 cm distant from the arc.

Chapter 6

Online determination of sintering parameters for metal nanoparticles and their application in a simple model for particle size estimation

The scope of this chapter is to present a model, which describes the formation of particles by the present transferred arc process. The model applies the data obtained along fluid streamlines from CFD simulations of the OSU setup. An important aspect of nanoparticle formation, especially the evolution of primary particle size, is the sintering of particles. To describe sintering accurately and hence the formation of particles by the model, material dependent sintering parameters are required, which are determined experimentally in the first section of this chapter. Afterwards, the model is described.

6.1 Determination of sintering parameters

Sintering is a fundamental process in nanoparticle formation. It describes the densification of primary particles in agglomerates driven by the reduction of surface curvature and energy [45, 87]. Sintering is an irreversible process, in which coalescence and rearrangement of primary particles form an agglomerate even up to a compact sphere [117]. It is not a melting phenomenon. It takes place during nanoparticle formation processes, when e.g. aggregates are formed (neck formation between two collided particles). Sintering is also applied to change the morphology of synthesized nanoparticles and agglomerates. There are various diffusion mechanisms, which lead to the densification (sintering) of an agglomerate [125]. These mechanism are mathematically expressed in several equations to describe the sintering behavior [45]. Usually, there are at least two

unknown material dependent parameters in these equations, namely the activation energy E_a and a sintering kinetic constant c. This chapter concentrates on determining those two parameters for metal nanoparticles used in this work in order describe their formation process.

Sintering parameters for various metals are investigated. The change in the mobility diameter of nanoparticles (Ag, Al, Cu, Zn), produced by transferred arc synthesis, is measured using a tandem-DMA setup. The gained data is analyzed to obtain the sintering parameters. Three diffusion mechanisms that cause coalescence of nanoparticles are studied, namely: grain boundary diffusion, volume diffusion and surface diffusion. Sintering due to rearrangement is not part of this investigation.

6.1.1 Sintering parameters

The sintering parameters are determined by a fitting procedure, which bases on the work of Koch and Friedlander [82]. Sintering is described there as a phenomenon of surface area reduction:

$$\frac{\mathrm{d}a}{\mathrm{d}t} = -\frac{1}{\tau_\mathrm{s}}\left(a - a_\mathrm{f}\right) \tag{6.1}$$

where $\mathrm{d}a$ is the change of surface area during the time $\mathrm{d}t$, a_f is the surface area of the agglomerate after complete sintering and τ_s is the characteristic sintering time. The sintering time is strongly temperature dependent, but it also depends on the primary particle diameter d_p and the applied diffusion mechanism [45,81]. For grain boundary and surface diffusion the dependency is given in equation 6.2 and for volume diffusion in equation 6.3 [18, 19, 23]:

$$\tau_\mathrm{s,GB,SD} = C(T) d_\mathrm{p}^4 \tag{6.2}$$

$$\tau_\mathrm{s,VD} = C(T) d_\mathrm{p}^3 \tag{6.3}$$

with $C(T)$ being the temperature depending constant

$$C(T) = \frac{c \cdot T}{exp\left(-E_\mathrm{a}/RT\right)} = c \cdot T \cdot exp\left(E_\mathrm{a}/RT\right) \tag{6.4}$$

that contains the temperature T, the gas constant R and the sintering parameters c and E_a. These sintering parameters are determined in this chapter. E_a is the activation energy that has to be overcome to start the sintering process. c is a pre-exponential parameter that contains different material dependent constants.

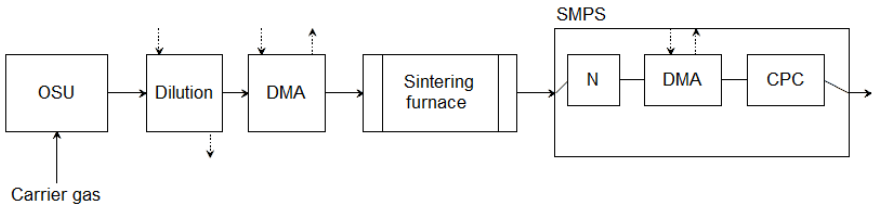

Figure 6.1: *Experimental setup to determine sintering parameters*

6.1.2 Experimental procedure & model to determine sintering parameters

Figure 6.1 depicts the experimental setup used to determine the sintering parameters. The sintering procedure is investigated by a tandem-DMA setup [73]. The OSU with CD 6 is used to produce nanoparticles of different materials (Ag, Cu, Zn, Al). As some of these materials have a strong tendency to oxidize, the complete setup up to the connection to the SMPS applies vacuum components, including a vacuum-tight radial DMA [133]. An oxidization of the particles before entering the sintering furnace would lead to a changed material system, which should be avoided. The particles are classified in a first DMA and led into the sintering furnace (Carbolite TZF 12/75-700, Carbolite Limited, Hope Valley, United Kingdom). Different temperatures are applied in the sintering furnace to reach different extents of sintering. The temperature is successively increased. After the sintering process, the aerosol flows into a SMPS for a measurement of the mean mobility diameter (second DMA, TSI 3081). By this way, a shift of the mobility size, depending on the temperature can be observed, which expresses the sintering procedure.

For each material, several initial mobility (agglomerate) diameters are selected with the first DMA and a number based size distribution is measured after sintering at different temperatures with the SMPS. The change in the modal value of the mobility diameters is observed and used to obtain the temperature dependent mobility diameters for 4 or 5 different initial mobility diameters (Figure 6.2). In most cases the temperature is increased close to the melting point of the bulk material, even if the sintering process is completed at lower temperatures. This is done to obtain every part of the sintering curve, including the point of complete coalescence.

As described in chapter 3.2.3.3, the SMPS measures an electrical mobility diameter. Therefore equation 6.1 is transposed from the change of surface over time ($\frac{\mathrm{d}a}{\mathrm{d}t}$) into the change of the primary particle diameter over time ($\frac{\mathrm{d}d_\mathrm{p}}{\mathrm{d}t}$).

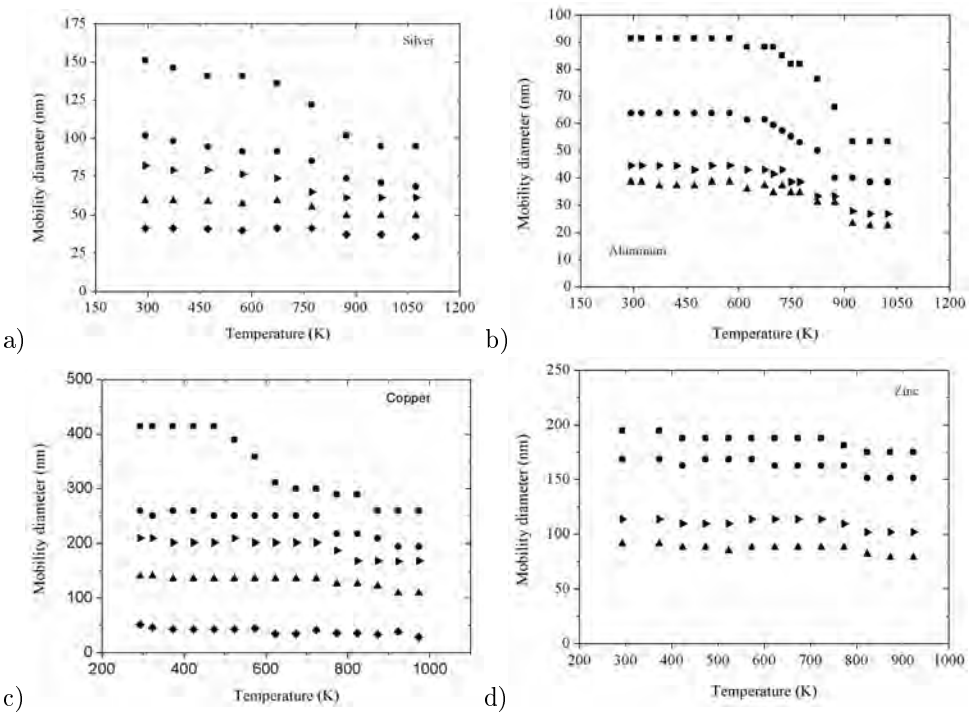

Figure 6.2: *Temperature dependent mobility diameter for a) silver b) aluminum c) copper and d) zinc nanoparticles for different initial mobility diameters.*

With the assumption of constant volume and the knowledge of the final fully sintered particle ($d_{\mathrm{m,f}}$)

$$V_{\mathrm{p}} = \frac{\pi}{6} d_{\mathrm{m,f}}^3 = \frac{\pi}{6} n_{\mathrm{p}}.d_{\mathrm{p}}^3 \tag{6.5}$$

one can derive for the number of primary particles in an agglomerate:

$$n_{\mathrm{p}} = \left(\frac{d_{\mathrm{m,f}}}{d_{\mathrm{p}}} \right)^3$$

and for the agglomerate surface area:

$$a = n_{\mathrm{p}} \pi d_{\mathrm{p}}^2 = \frac{\pi d_{\mathrm{m,f}}^3}{d_{\mathrm{p}}}$$

and hence:

$$\frac{\mathrm{d}a}{\mathrm{d}d_{\mathrm{p}}} = \frac{-\pi d_{\mathrm{m,f}}^3}{d_{\mathrm{p}}^2} \tag{6.6}$$

Applied to equation 6.1 follows:

$$\frac{\mathrm{d}a}{\mathrm{d}t} \cdot \frac{\mathrm{d}d_p}{\mathrm{d}d_p} = -\frac{1}{\tau_\mathrm{s}} \left(a - a_\mathrm{f}\right)$$

$$\frac{\mathrm{d}d_p}{\mathrm{d}t} \cdot \frac{-\pi d_\mathrm{m,f}^3}{d_\mathrm{p}^2} = -\frac{1}{\tau_\mathrm{s}} \left(\frac{\pi d_\mathrm{m,f}^3}{d_\mathrm{p}} - \pi d_\mathrm{m,f}^2 \right)$$

$$\frac{\mathrm{d}d_\mathrm{p}}{\mathrm{d}t} = \frac{1}{\tau_\mathrm{s}} d_\mathrm{p}^2 \left(\frac{1}{d_\mathrm{p}} - \frac{1}{d_\mathrm{m,f}} \right) \tag{6.7}$$

The derivation above is valid for grain boundary, surface and volume diffusion, but it is not possible to differentiate between grain boundary and surface diffusion, because both share the same dependency on the primary particle diameter in the sintering time τ_s (equation 6.2) [23]. The sintering parameters obtained by fitting to the experimental data are valid for both diffusion mechanisms, although different material constants appear. For volume diffusion the corresponding sintering time equation 6.3 is used.

By using equation 5.3 from the previous chapter and the assumption of a constant volume (equation 6.5) during sintering, the primary particle size d_p of particles in an agglomerate with the mobility size d_m can be calculated by:

$$d_\mathrm{p} = \left(\frac{d_\mathrm{m,final}^3}{d_\mathrm{m}^{D_{fm}}}\right)^{\frac{1}{3-D_{fm}}} \tag{6.8}$$

The sintering profile obtained by the tandem DMA setup is used to derive the primary particle diameter using equation 6.8. d_p can also be calculated by numerically integrating equation 6.7 given the sintering parameters. Minimizing the error function between these two diameters by varying the sintering parameters c and E_a delivers both values experimentally. This procedure has been repeated for several initial mobility sizes.

As discussed in the previous chapter, the mass mobility exponent D_{fm} has a significant influence on the estimated primary particle size. For the presented fitting procedure a mass mobility exponent of 2.2 is assumed for all agglomerates, although the study in the previous chapter has shown that even higher mass mobility exponents may appear in transferred arc synthesis. The fixed mass mobility exponent is a limitation of this model, which might be solved in a future work by expressing the mass mobility exponent as a function of n_p.

6.1.3 Experimentally obtained sintering parameters of metal nanoparticles

An overview of the obtained sintering curves is depicted in figure 6.2. The initial mobility diameters of silver (a) at the start of the sintering process ranged from 40 to 150 nm. The compaction due to sintering extends over a rather long

range of temperature. The compaction starts at about 500 K and is completed at about 1000 K. The starting mobility diameter of aluminium ranged from 40 to 90 nm. The compaction of aluminium (b) begins at about 700 K and is finished at about 900 K. The starting diameters of the copper particles range from 80 to 400 nm, as primary particle sizes of about 80 nm have been measured in the synthesis experiments described in chapter 4. The copper nanoparticles begin to compact at about 600 K. Sintering is completed at about 800 K. The cause for the short compaction range and the smaller difference between initial and final particles is considered to be the rather big size of the primary particles. The sintering curve of the 400 nm particles appears different than the others, which might indicate a different sort of agglomeration at that size. The average diameter of primary particles of zinc (d) is rather high, too. The compaction of zinc begins at about 750 K and finishes at about 850 K. The point of total compaction is not easy to find, as the decrease in diameter is hardly noticeable. A further increase of the temperature is not depicted here, as starting evaporation leads to significant changes in the mobility diameter.

Figure 6.3 shows the best-fitted curves (grain boundary and volume diffusion) for each metal. Figure 6.3 a) depicts the sintering curve and the primary particle diameter of silver that started sintering with a mobility diameter of 100 nm. The difference between the models of grain boundary / surface and volume diffusion is barely noticeable. Near the end of the sintering curve, at which the number of primary particles in the agglomerate becomes one, the grain boundary/surface diffusion model seems to overestimate the values of the primary particle diameter more than the model of volume diffusion, but only marginally. The fitting procedure for silver works fine as long as the classified starting mobility size is above the primary particle size of 27 nm. For aluminium (b) the measurement shows a good agreement between model and measurement. The primary particle size has been estimated to approximately 10 nm. For copper (c) a comparison of the model for grain boundary and volume diffusion is shown for a starting diameter of 210 nm. In general, the differences in the fitting results between grain boundary / surface and volume diffusion are only minor. The larger primary particle sizes of copper and zinc (d) however require a careful evaluation of measurement data obtained at critical particle sizes. The model shows deviations at a mobility size of 200 nm for zinc, since the agglomerates seem to consist of only 1.5 primary particles.

Table 6.1 summarizes the obtained sintering parameters for every material examined in this work. In addition, the model is applied to experimental data of Nakaso et al. for gold [117]. The results are also displayed in table 6.1. It appears that regardless of the diffusion mechanism and material, the activation energy E_a is in a range from 90 kJ/mol to 300 kJ/mol. The difference in the activation energy is small in comparison to the pre-exponential parameter c, so

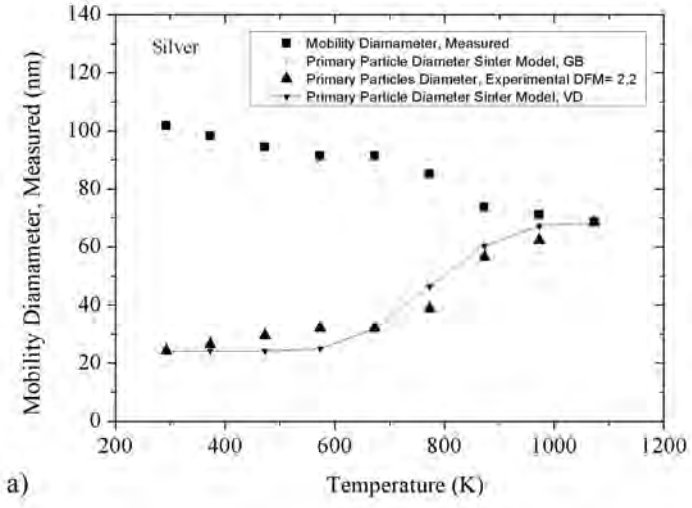
Silver
Mobility Diamameter, Measured
Primary Particle Diameter Sinter Model, GB
Primary Particles Diameter, Experimental DFM= 2.2
Primary Particle Diameter Sinter Model, VD
Mobility Diamameter, Measured (nm)
Temperature (K)
0
20
40
60
80
100
120
140
200
400
600
800
1000
1200

a)

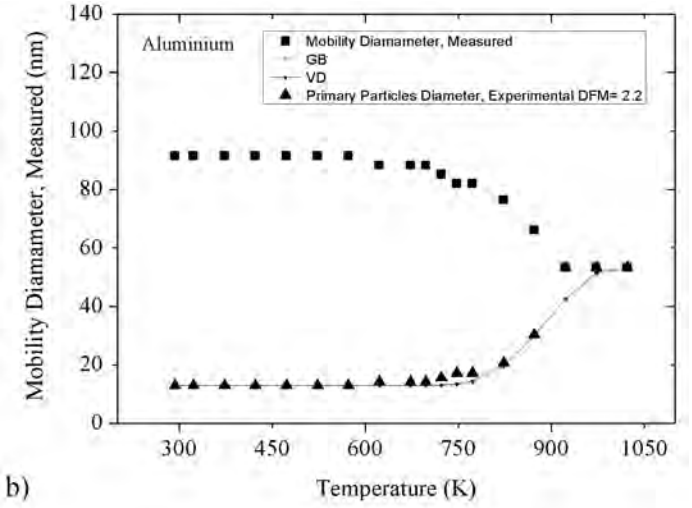
Aluminium
Mobility Diamameter, Measured
GB
VD
Primary Particles Diameter, Experimental DFM= 2.2
Mobility Diamameter, Measured (nm)
Temperature (K)
0
20
40
60
80
100
120
140
300
450
600
750
900
1050

b)

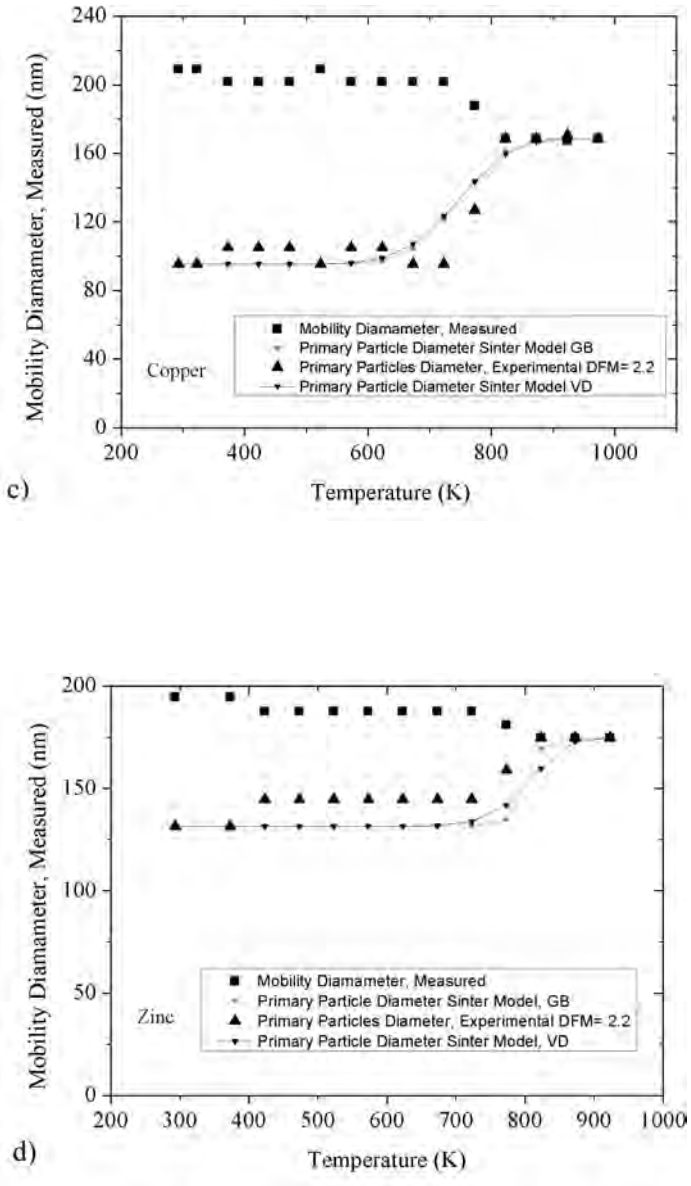

Figure 6.3: *Sintering procedure for c) copper and d) zinc nanoparticles for selected sizes*

Table 6.1: *Sintering parameters obtained by the presented procedure*

Material	Grain boundary /Surface Diffusion		Volume Diffusion	
	$c_{\mathrm{GB,SD}}$ ($\mathrm{s/m^4K}$)	$E_{\mathrm{GB,SD}}$ (J/mol)	c_{VD} ($\mathrm{s/m^3K}$)	E_{VD} (J/mol)
Ag	$2.31 \cdot 10^{19}$	$1.11 \cdot 10^{5}$	$1.67 \cdot 10^{13}$	$9.20 \cdot 10^{4}$
Cu	$2.76 \cdot 10^{16}$	$1.33 \cdot 10^{5}$	$1.58 \cdot 10^{11}$	$1.08 \cdot 10^{5}$
Al	$9.52 \cdot 10^{10}$	$2.78 \cdot 10^{5}$	$5.45 \cdot 10^{6}$	$2.21 \cdot 10^{5}$
Zn	$1.52 \cdot 10^{5}$	$3.10 \cdot 10^{5}$	$4.83 \cdot 10^{6}$	$1.72 \cdot 10^{5}$
Au	$3.11 \cdot 10^{23}$	$1.06 \cdot 10^{5}$	$2.58 \cdot 10^{16}$	$8.32 \cdot 10^{4}$

that the existence of a general activation energy for sintering seems reasonable. The stable value of activation energy might also be caused by the fitting procedure. Both sintering parameters are alternated in order to find the minimum error. However, the fitting routine can not distinguish between a local or absolute minimum and small changes in the activation energy lead to big changes in the temperature constants.

Comparing the activation energy E_{a} obtained by this work for metal particles to literature data for bulk metals (table 6.2) [45], one can conclude that the values are generally in a good agreement. For grain boundary and surface diffusion, the activation energy of copper, silver and gold of the nano-sized particles are between the literature values of those two diffusion mechanisms for the according bulk metal. As the model of this work cannot distinguish between these two mechanisms, values in between seem to be reasonable. The estimated activation energies for surface and grain boundary diffusion of aluminium and zinc particles are larger than the bulk metals activation energy. Both metals have a higher tendency towards oxidization than the other ones, so small amounts of oxygen inside the system might lead to particle contamination. An oxide layer would increase the activation energy for sintering significantly [139]. For volume diffusion, the values determined for nanoparticles are smaller than for the bulk material, with the exception of zinc and aluminium, which again might be reasoned by an oxygen contamination. The activation energy for volume diffusion is generally smaller than the bulk values. This can be explained by the difference of curvature of the bulk and nanoparticle body [45].

Comparing the determined pre-exponential factors c of the different metals, aluminium and zinc have the lowest pre-exponential parameter for both diffusion mechanisms, while gold has the highest. The value can be compared to the atomic volume of the material, as gold has the highest and aluminium the lowest atomic volume. The size effect of atomic volume on the diffusion mechanism during sintering is described in the literature [45,141]. When arranged in order, there is also a congruence between the parameter and the metals densities found.

Table 6.2: *Comparison of the activation energy for sintering of bulk [45] and particle (this work) metal*

Material	Grain boundary ; Surface Diffusion		Volume Diffusion	
	bulk [45] (kJ/mol)	nano (This work) (kJ/mol)	bulk [45] (kJ/mol)	nano (This work) (kJ/mol)
Ag	90; 266	110.55	185	91.956
Cu	107; 205	132.59	213	108.29
Al	60; 142	277.81	142	221.01
Zn	60; 27	310.42	94	171.94
Au	110; 234	105.80	172	83.157

This is shown in figure 6.4. The density of a material impacts e.g. its heat capacity. The lower the heat capacity of a material, the lower is the amount of energy that has to be imparted to the material to heat it up. For sintering, the heat is needed to start the diffusion process.

The explanation above does not fit for zinc, as the pre-exponential parameter does not behave according to the ones of the other metals. Zinc crystallizes in a hexagonal crystal system. Also the grain sizes of zinc are much bigger than the ones of the other metals. Both attributes are known to effect the sintering behavior strongly and may hence explain the much lower value of the pre-exponential parameter [35, 73].

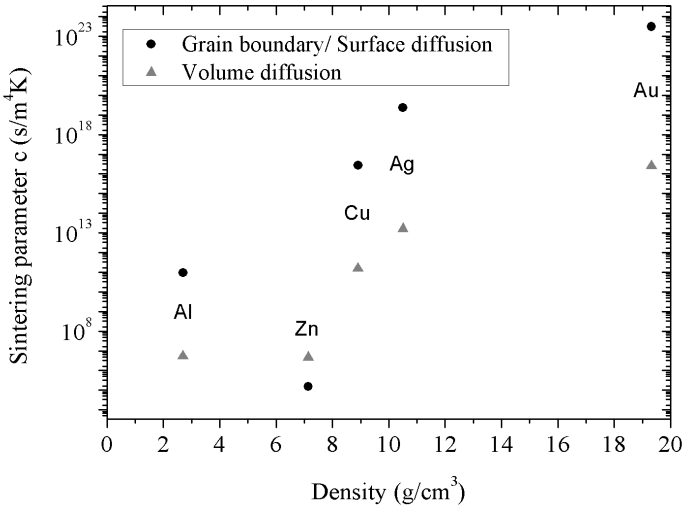

Figure 6.4: *Influence of material density on pre-exponential sintering parameter c for volume and surface/grain boundary diffusion*

6.2 A simple model for particle size estimation

A simple model to predict the particle size of the particles produced in the arc and describe the formation process is developed. It bases on CFD data made accessible by the University of Tampere, which describes the temperature, metal vapor concentration, and position for 65 pathlines in a concrete model of the OSU. In the following, the results of the model is shown for four of the 65 pathlines.

6.2.1 Nucleation

From the CFD data the temperature profile and the copper vapor concentration is used to estimate the particle growth inside the OSU chamber, based on classical nucleation, coagulation and sintering theory [40,87]. For sintering, the sintering parameters of copper determined in the previous section are used.

Is the temperature T, the saturation vapor pressure p_S and the copper monomer concentration n_1 in a system known, the saturation S of the copper vapor can be calculated by:

$$S = \frac{p_1}{p_S} = \frac{n_1 kT}{p_S} \tag{6.9}$$

n_1 is the copper monomer concentration and p_1 the partial pressure of copper. The saturation S changes therefore upon a change in temperature T and especially a change in the copper monomer concentration n_1 due to nucleation, which can be expressed as:

$$\frac{\mathrm{d}n_1}{\mathrm{d}t} = -n_i I \tag{6.10}$$

, where n_i is the number of atoms in a formed nucleus and I the nucleation rate of particles/ nuclei.

Figure 6.5 shows the temperature profile of 4 pathlines from the given CFD data. Drastic differences between the temperature profiles are visible, which can be explained by the spatial and stochastic differences of the streampaths, which also show some degree of turbulence. Some tend to circle around the crucible respectively the hot area and do not cool down so that no saturation appears up to 3 seconds. Other streams reach the saturation point at different times due to a stronger cooling rate. The saturation calculated on basis of these 4 temperature profiles and an according copper monomer concentration is given in figure 6.6. Depending on the monomer concentration and the temperature profile the saturation changes, most often leading to a supersaturation, which means that $S > 1$. The nucleation starts at that point, which is indicated by a

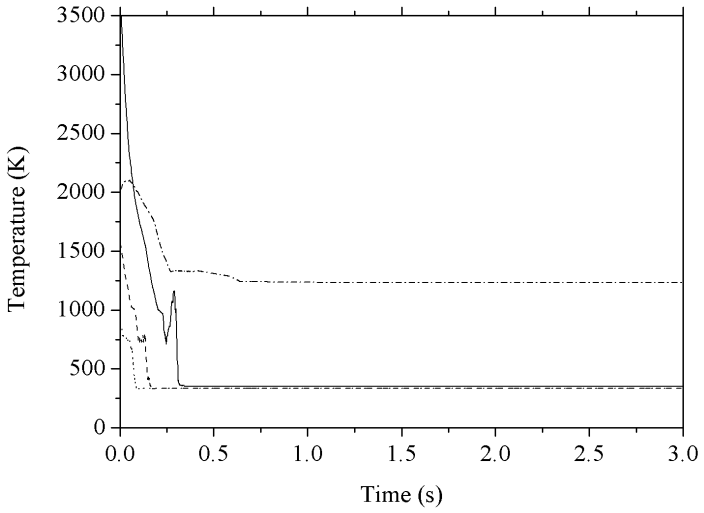

Figure 6.5: *Temperature of 4 streamlines of the underlying CFD-model*

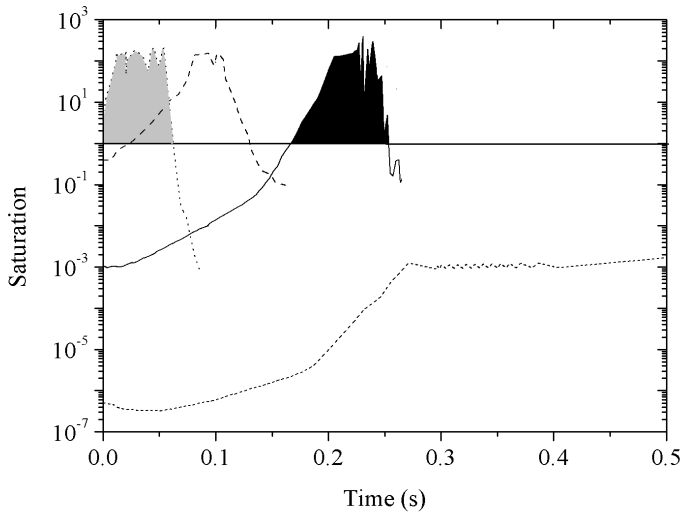

Figure 6.6: *Saturation calculated for the 4 temperature profiles of figure 6.5 and related copper monomer concentration*

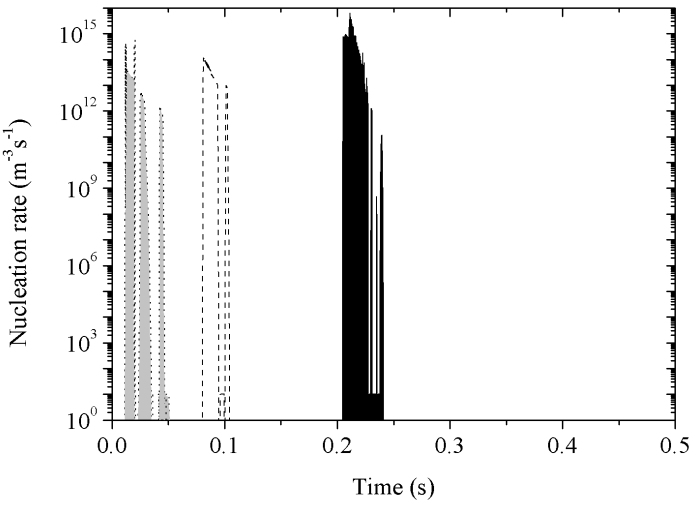

Figure 6.7: *Nucleation rate for the three supersaturated pathlines from figure 6.6*

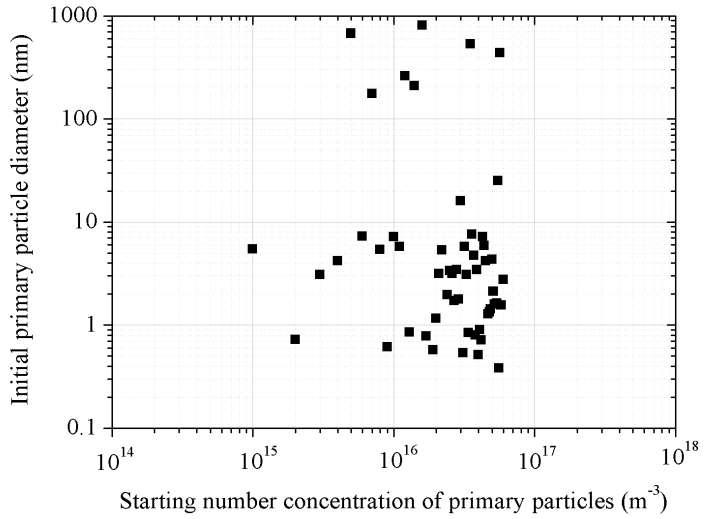

Figure 6.8: *Initial primary particle diameter and number concentration obtained from the nucleation model for all obtained streamlines*

black line in the figure. As depicted only 3 of the 4 shown streamline profiles lead to a supersaturation. In one case (dash-dotted line) the temperature does not decrease that significantly so that the vapor is supersaturated, which means that in that case no nucleation appears. The nucleation rate on these streamlines is shown in figure 6.7. Only the three supersaturated streamlines lead to a nucleation rate. The nucleation rates of the 3 streamlines are almost the same, as well as the supersaturation has been, due to similar monomer concentrations and temperatures. The particle concentration N formed by nucleation can be calculated by integrating over the nucleation rate:

$$N = \int_{t_0}^{t} I \mathrm{d}t \tag{6.11}$$

The initial number concentration N of the formed particles is depicted in figure 6.8 for all pathlines. Here, it is shown over the primary particle diameter, which is actually the critical nucleus diameter d_n^* (see chapter 3.1.1). The nucleus diameter of the primary particles varies over three magnitudes, which is reasonable as the d_n^* reacts quite sensitive on differences in temperature and saturation. The number concentrations lead to realistic values. These diameters and number concentrations are used as input to a coagulation and sintering model on basis of the temperature profile.

6.2.2 Coagulation and Sintering

The coagulation and sintering model for particle size estimation bases on the model of Kruis et al. [87] extended by the determined sintering parameters. The evolution of particle size d_p and number of primary particles per agglomerate n_p is estimated by the ratio of surface a and volume v_a of the formed agglomerates:

$$d_\mathrm{p} = \frac{6 v_\mathrm{a}}{a} \tag{6.12}$$

$$n_\mathrm{p} = \frac{v_\mathrm{a}}{v_\mathrm{p}} \tag{6.13}$$

v_p is the volume of the primary particle. The volume of the agglomerate v_a does only change due to coagulation:

$$\frac{\mathrm{d}v_\mathrm{a}}{\mathrm{d}t} = -\frac{1}{N}\frac{\mathrm{d}N}{\mathrm{d}t} v_\mathrm{a} \tag{6.14}$$

with

$$\frac{\mathrm{d}N}{\mathrm{d}t} = -\frac{\beta}{2} N^2 \tag{6.15}$$

N is the number concentration of particles (or agglomerates) and β the collision frequency between the particles (or agglomerates), which is also a function of

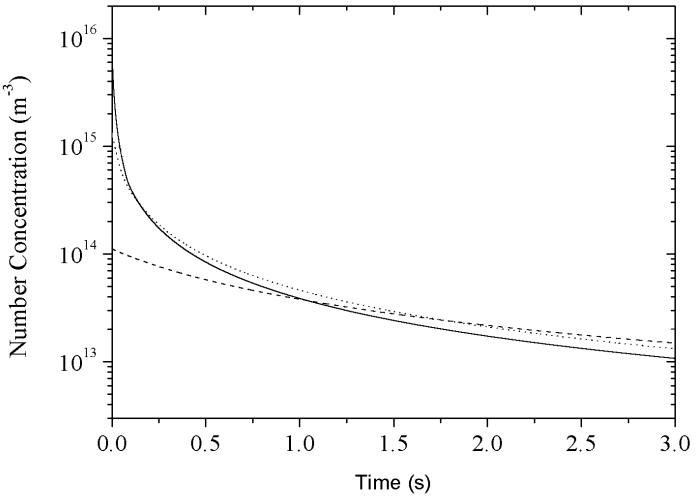

Figure 6.9: *Exemplary number concentrations over time*

v_a (see chapter 3). The surface area of an agglomerate a increases due to coagulation, but decreases due to sintering [82].

$$\frac{\mathrm{d}a}{\mathrm{d}t} = -\frac{1}{N}\frac{\mathrm{d}N}{\mathrm{d}t}a - \frac{1}{\tau_\mathrm{S}}(a - a_\mathrm{f}) \tag{6.16}$$

τ_S is the characteristic sintering time, which is calculated on basis of the sintering parameters described in the previous section. a_f is the surface of a spherically sintered agglomerate and can be calculated with help of the primary particle surface area a_0 and volume v_0 by:

$$a_\mathrm{f} = (\frac{v_\mathrm{a}}{v_0})^{\frac{2}{3}} a_0 \tag{6.17}$$

Figure 6.9 shows the number concentration of particles/ agglomerates over time for four exemplary pathlines. As expected, the number concentration decreases due to coagulation for all pathlines. Independent of the starting number concentration, the number concentration reaches the same order of magnitude (10^{13} m^{-3}), which is a common number concentration for production aerosols. Figure 6.10 a) shows the evolution of primary particle size resulting from the model. As depicted, the particle size increases over time for all pathlines due to coagulation and sintering. Smaller particles tend to increase their size stronger, as coagulation and sintering is more rapid for smaller particle sizes. Of course also the temperature profile and residence time of each pathline impacts the particle size. The strong increase in particle size corresponds with the particle sizes determined by the thermophoretic sampler in the previous chapter. Parti-

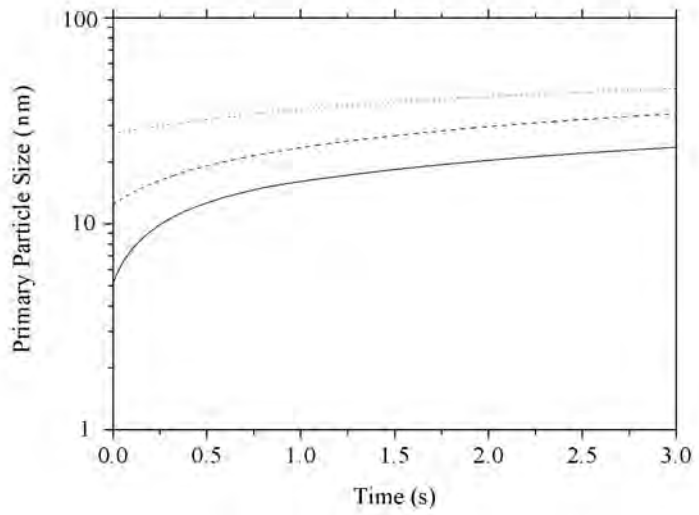

a)

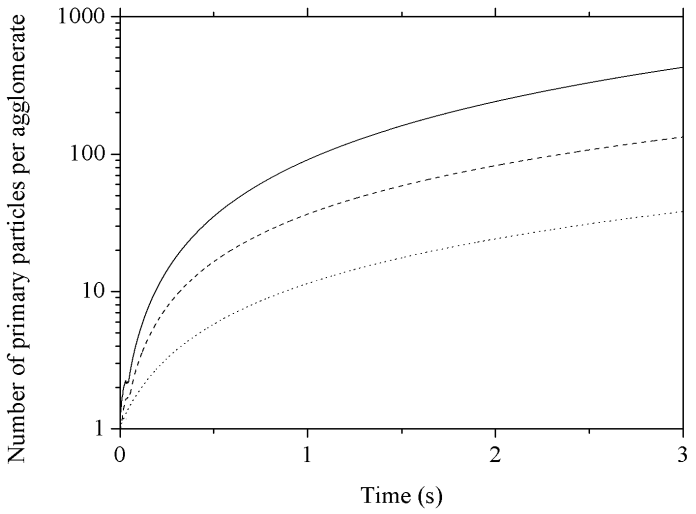

b)

Figure 6.10: *Exemplary primary particle size a) and number of primary particles per agglomerate b) during coagulation and sintering for the exemplary curves of figure 6.9*

cle sizes in the range from 8 to 60 nm result from the model, which is lower than the actual measured particle sizes for the given parameters (700 W, nitrogen, CD7, Q_1= 40 l/min, Q_2 =3 l/min). The experimentally determined mean primary particle size is 83 nm. The error resulting from the model might be based on a too low temperature in comparison to the real conditions. An increased temperature favors sintering and thus the formation of bigger particles. Figure 6.10 b) shows the number of primary particles per agglomerate. The number of particles per agglomerate differs strongly for the different pathlines, depending on the coagulation and sintering rate and hence on the primary particle size. The model seems to overestimate the number of particles per agglomerate, which is again a result of temperatures. A higher temperature promotes sintering and therefore a lower degree of agglomeration.

Apart from the too low absolute values of mean primary particle size, the model seems to describe the formation of particles in a transferred arc in a qualitative manner sufficiently, undergoing simultaneous coagulation and sintering with the determined sintering parameters. Especially the influence of number concentration (evaporation rate) and temperature profile (applied arc power, gas flow) on the particles can be described by the model.

Chapter 7

Nanoparticle synthesis by multiple transferred arcs (mOSU)

The main goal of this thesis is to develop a production facility that is suitable of producing metal nanoparticles in larger amounts. The previous chapters describe the development and characterization of the OSU (one electrode pair) and its production attributes. It is shown in chapter 4.3 that the production rate of the OSU depends mostly on the size of the primary particles, which can be controlled amongst others by the carrier gas composition and the applied electric current. Nitrogen is found to be by far the most economic carrier gas in non-nitride forming systems. This leaves the electric current as a controlling parameter. A higher electric current leads to bigger particles and thereby to an increased production rate. The maximum primary particle size is by definition 100 nm. Hence, for one electrode pair the maximum production rate is limited.

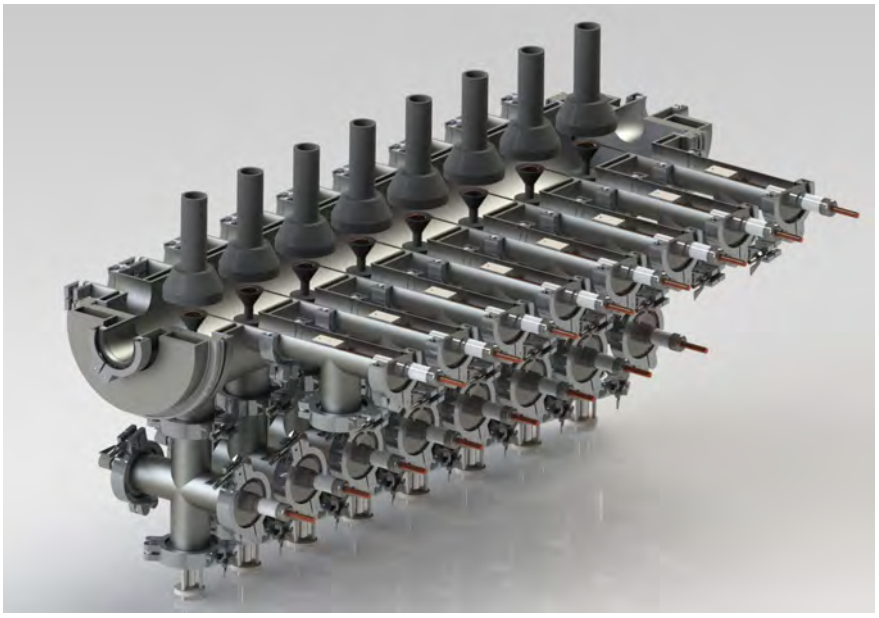

Figure 7.1: *Cut-through schematic of the mOSU with crucible setup 7*

In order to reach higher production rates of nanoparticles, the approach in this thesis is to multiply the number of electrode pairs and thereby multiply (scale-up) the total production rate. This setup is called multiple Optimal Single Unit (mOSU). The basic idea is to increase the production rate by increasing the number of electric arcs (not the power of one arc), keeping the infrastructure of the setup almost the same, meaning that there is still only one reactor housing, one gas supply, one filtration unit, etc. required. Table 7.1 lists the parts, which can and cannot be scaled up. An essential advantage of the scale-up by parallelization is that most of the process optimization and testing is done on the lab-scale version (OSU), before it is applied to the production facility, with the expected outcome in terms of production quality of the mOSU, being the same as from a single OSU. Based on practical issues such as ease of handling and cleaning, the mOSU is designed containing 8 electrode pairs (Figure 7.1). Some parts of course have to be adapted to the unit multiply due to technical or safety issues, as e.g. each electrode pair needs its own power supply.

The production facility for metal nanoparticles built for this thesis consists of two mOSUs, a filter unit and a gas reconditioning and recirculating system. This chapter describes the development, setup and synthesis of the scaled-up production facility. A German patent has been filed containing some of the following parts (see appendix D).

Table 7.1: *Scalable and not scalable parts of the production facility*

Scalable parts	Not scalable parts
Vacuum pump	Power supply
Roots pump (Gas supply)	Electric connections
Reactor housing	Electrodes
Piping	Feeder
Monitoring devices	
Process cooling	
Filtration unit	

7.1 Setup of the pilot plant for nanoparticle production

In this section the different parts of the production facility containing two mOSUs is described. Principally it can be divided in three parts, the synthesis of particles by the mOSUs, the collection of the produced particles inside a filter unit and the gas supply and reconditioning (Figure 7.2).

Figure 7.3 shows a process schematic of the pilot plant containing two mOSUs. A key factor of this process is the recirculation of carrier gas by a roots pump (recirculating pump 1). The process can hence be described as a closed loop. It can be evacuated before synthesis by a vacuum pump (2). To prevent the system from overheating the recirculated carrier gas is cooled before entering the roots pump by a gas cooling unit. The circulated amount of carrier gas is measured by differential pressure monitoring over a 40 mm orifice, before it enters the mOSU's by a gas distribution system. Two distributors divide the carrier gas flow equally on each of the 16 electrode pairs inside the two mOSUs. Particles are formed in the mOSUs and carried away by the carrier gas out of the mOSUs through the product flow joiner. The product flows of the mOSUs combine and enter a filter unit for particle deposition. Two filters are attached to the mOSU setup, so that the synthesis can be kept running when

Figure 7.2: *Graphic of the mOSU production facility*

one of the filters is loaded. Particle deposition is then happening in the second filter. Two cleaning mechanisms are applied to each filter, a dry pulsed cleaning (valves R1-R10) and a wet cleaning (valves B1-B5) mechanism. Prior to cleaning the deposited particles can be passivated by a controlled addition of oxygen (synthetic air) into the setup (S1-S3). The collection of material takes place without additional valves in a plastic bag inside bag housing, which is held on the same pressure as the chamber. The filter outlet is again connected to the gas recirculation setup, where the closed loop begins again.

Figure 7.4 shows a picture and a model of the production facility. In the following sections, the major parts of the setup are described in detail.

7.1.1 Gas supply & reconditioning

As concluded in chapter 4.3, for non-nitride forming metals nitrogen appears to be by far the most efficient carrier gas. The material selected for the operational testing of the pilot plant containing two mOSU units is copper. Therefore a nitrogen supply has been adapted to the setup. Nevertheless, other gas compositions such as e.g. argon can be applied easily. In order to prevent oxygen contamination, the process is evacuated prior to synthesis and refilled with the carrier gas twice. To that end a vacuum pump (2) (Trivac D65B,Oerlikon Leybold Vacuum GmbH, Cologne, Germany) in connection with a roots pump (1) (Ruvac WA 501, Oerlikon Leybold Vacuum GmbH) is used to evacuate the setup to a pressure of 1 mbar. Afterwards the system is filled with the carrier gas (purified nitrogen from the house supply) to atmospheric pressure, which is the working pressure. During synthesis, the roots pump is used to recirculate the carrier gas in the closed loop of mOSU and filter. To prevent the system from overheating, the gas is cooled in front of the roots pump by a gas cooling unit. The recirculating amount of gas can be adjusted by a valve (G12) attached to a roots pump-by-pass. From valve R5 or G13, a small portion of the product flow can be sampled from the process. This requires however the same amount of gas to be added (via G1,G5 or G6).

The total gas flow entering the mOSU units is measured by a differential pressure transducer, which measures the differential pressure over an orifice (40 mm). Figure 7.5 depicts the differential pressure over the orifice in dependence of the carrier gas flow rate, in open and closed circuit mode. The differential pressure increases exponentially with the applied gas flow, which makes the carrier gas flow easily adjustable in the desired flow range of approximately 50 l/min per electrode pair.

The gas flow enters the mOSU units by using a gas distribution system, which ensures the equal distribution of gas to each electrode pair in the mOSU units. Principally it is separated for one mOSU in three distributors of which two are equal. These two carrier gas distributors (figure 7.6a) are made of a

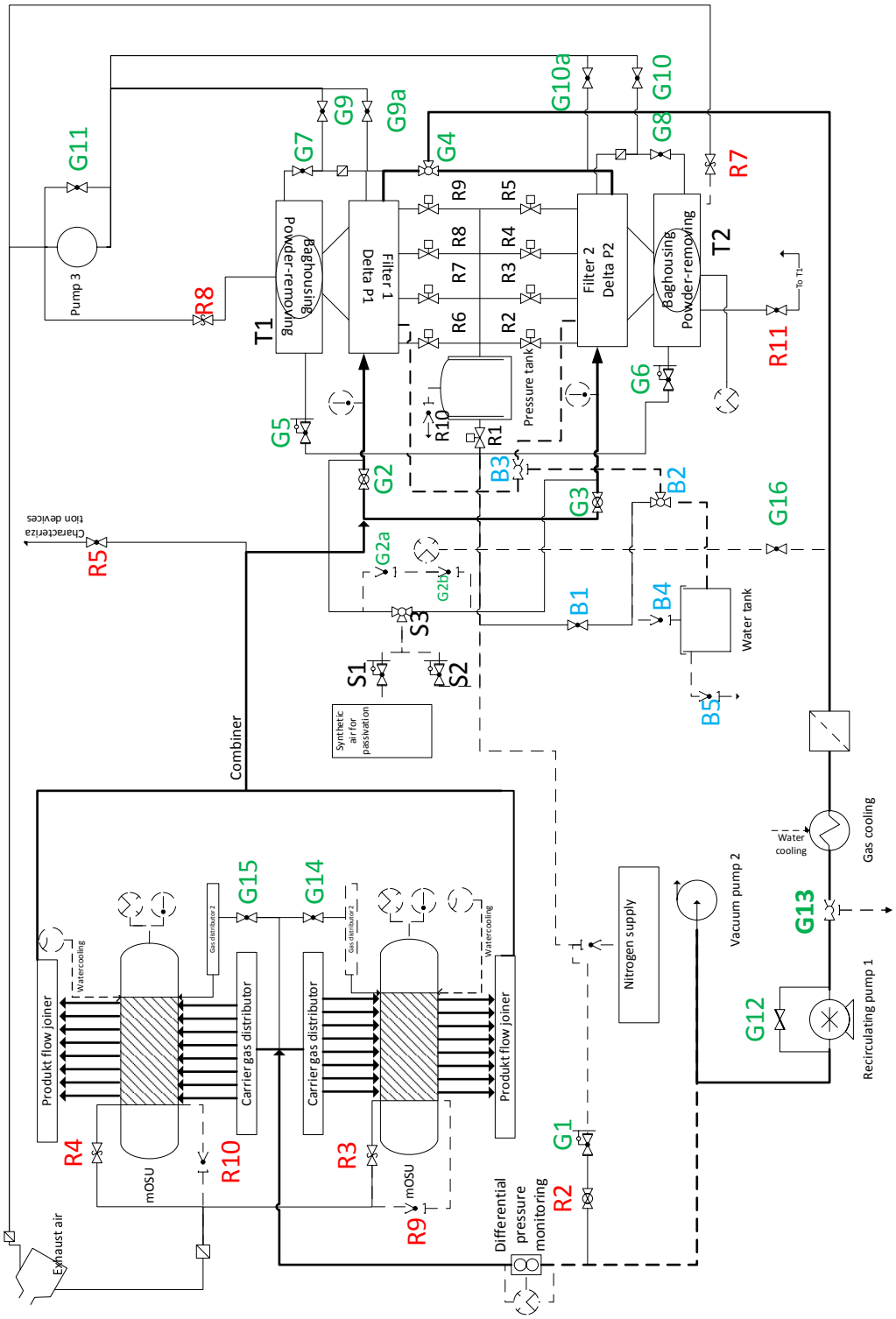

Figure 7.3: *Schematic of the pilot plant, with G1-16 valves for standard operation, R1-11 valves for emergency, dry cleaning or measurement, B1-5 valves for wet cleaning and S1-3 valves for passivation*

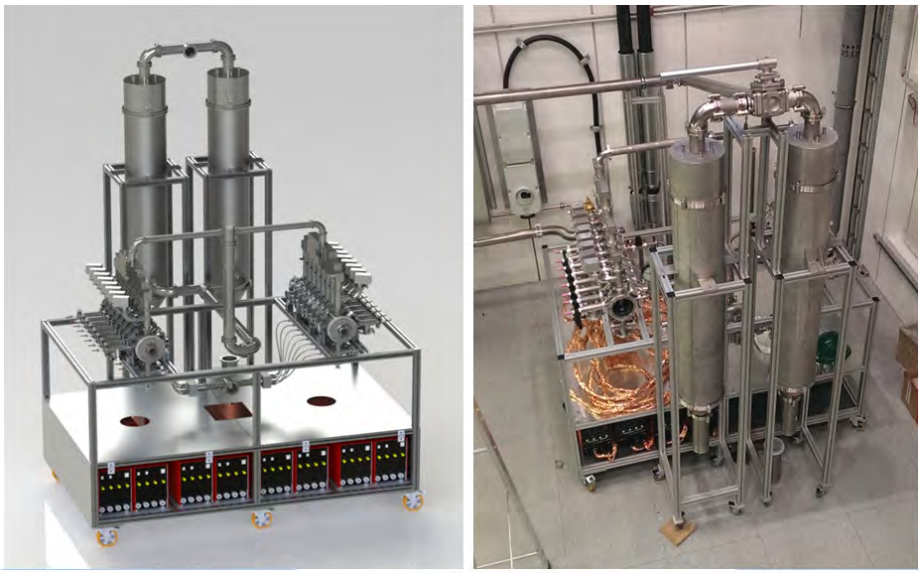

Figure 7.4: *Model (left) and picture of the production facility (right)*

chamber with an ISO-KF-40 inlet on the one side and four ISO-KF-16 ports at the other side, which are directly connected to the gas inlets at the bottom of each electrode pair. The carrier gas distributors are responsible for the main axial gas flow (Q_1). The third and smaller cathode flow distributor (figure 7.6b) is made of a chamber with an ISO-KF-40 inlet on the one side and eight Swagelok (6mm) outlets on the other side, which are connected to the gas inlets at the cathode ISO-KF-40 T-piece. Here, the smaller cross gas flow (Q_2), which can be adjusted by valve (G14 and G15) is applied. Both kind of distributors base on the same principal, which is an even distribution of gas due to a sudden increase pressure drop due to a diameter constriction.

Figure 7.6 shows a CFD simulation of the gas velocity through the carrier gas distributor (axial flow (Q_1), figure 7.6a) and the cathode flow distributor (cross flow (Q_2), figure 7.6b) (performed with Solid Works Flow Simulation). It shows that the total gas flow is distributed equally to the eight electrode pairs by both distributors, which is confirmed by the calculated values for each electrode pair. The mean gas flow through the carrier gas distributor is with 40.18 l/min (standard deviation of 1.13 l/min) and 3.04 l/min (standard deviation of 0.21 l/min) for the cathode flow distributor in a good range (Total flow 320 l/min for 8 electrode pairs). The pressure drop over the cathode flow distributor is calculated to be 0.8 mbar at a total flow of 24.3 l/min and 3.7 mbar at a total flow of 321.4 l/min for the two carrier gas distributors. Hence, the gas is evenly distributed with still acceptable pressure drops to each electrode pair, where the particle formation process takes place.

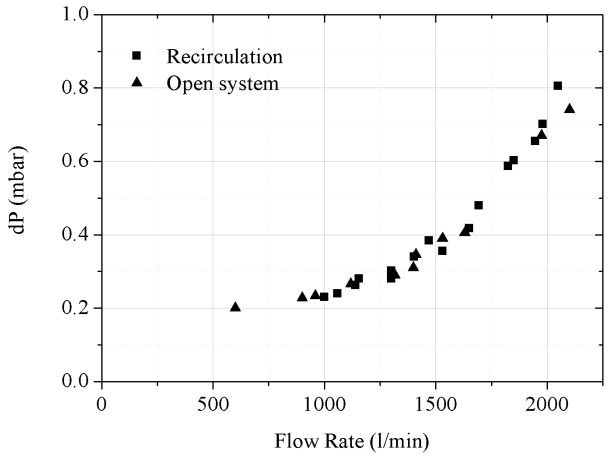

Figure 7.5: *Differential pressure in dependence of the carrier gas flow for two different operational modes*

7.1.2 multiple Optimal Single Unit (mOSU) for nanoparticle synthesis

The mOSU is the heart of the production facility. In the mOSU the production of nanoparticles takes place due to the eightfold parallel evaporation of the metal anode inside the crucible. The technical drawing of the mOSU housing is shown in the appendix (B.5). It is based on the proven OSU design with a water-cooled double walled DN ISO-K 160 chamber and six KF 40 ports arranged circumferentially, eight times in row with a core-to-core distance of 90 mm. The arrangement inside the chamber is similar to the one of the latest OSU (chapter 4.2 , figure 4.11), but 8 times in a row. Eight transferred arcs can be ignited in one chamber between the electrode pairs. There is no separating wall between the electrode pairs, but each electrode pair has its own gas inlet and outlet, power supply, electrode feeder, etc. It is basically the same process as in the OSU, but here eight times in one housing. Figure 7.7 shows an image of the inner mOSU setup with the latest crucible design 7. It shows eight tungsten rod cathodes entering the chamber from the left, the graphite crucible anodes filled with copper shots and the graphite hoods through which the produced aerosol leaves the reactor. There are also other ISO KF-40 parts visible, of which some are used as a view port, to adapt pressure or temperature monitoring devices or other measurement equipment.

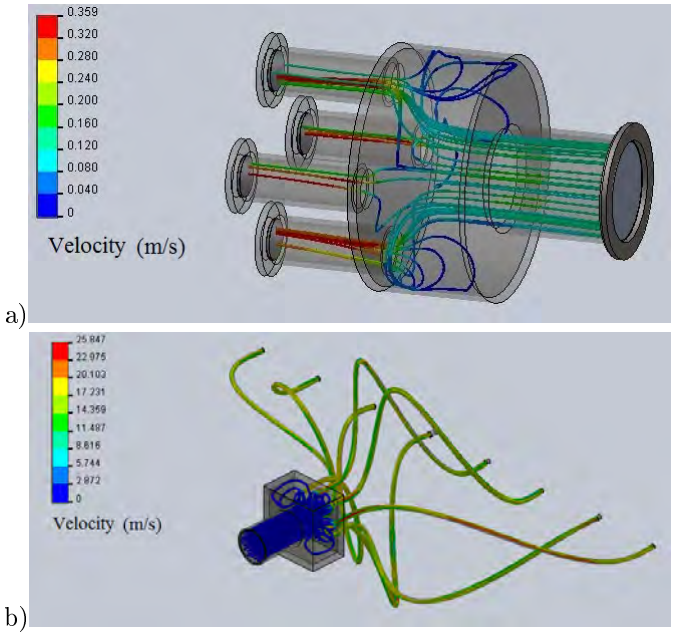

Figure 7.6: *CFD simulation of the gas flow velocity through the a) carrier gas distributor and b) the cathode flow distributor*

7.1.3 Filtration unit for particle collection

A major part of the production facility is the filtration unit. Here, particles are separated from the gas phase and collected. The filtration unit has been developed in cooperation with the Karlsruher Institute of Technology (KIT) and the Institute of Energy and Environmental Technology (IUTA). The goal has been to construct a device which separates the metal nanoparticles from the gas phase with a relatively low pressure drop ($<$ 50 mbar) even at high gas velocities and particle loadings. The collection of particles and cleaning of the filter cartridges should be easily performable. Both, wet as well as dry pulse cleaning is to be added in order to collect the nanoparticles in form of powder or dispersion and also allowing the filter and its housing to be wet cleaned. A main focus has been put on safety-relevant aspects, as the filtration unit is the place where the user of this device comes in contact with the product. Special requirements have thereby taken into account, as metal nanoparticles are produced with this facility, which tend to be self inflammable or even explosive under critical circumstances.

The optimal parameters for the production of metal nanoparticles for a single OSU are summarized in table 4.2 (chapter 4.4) leading to the long term production rates shown in figure 4.29. As the production facility consists of two mOSUs, the filtration unit has been designed for the parallel operation of 16 OSUs. Furthermore, as the production rate and parameters vary strongly of

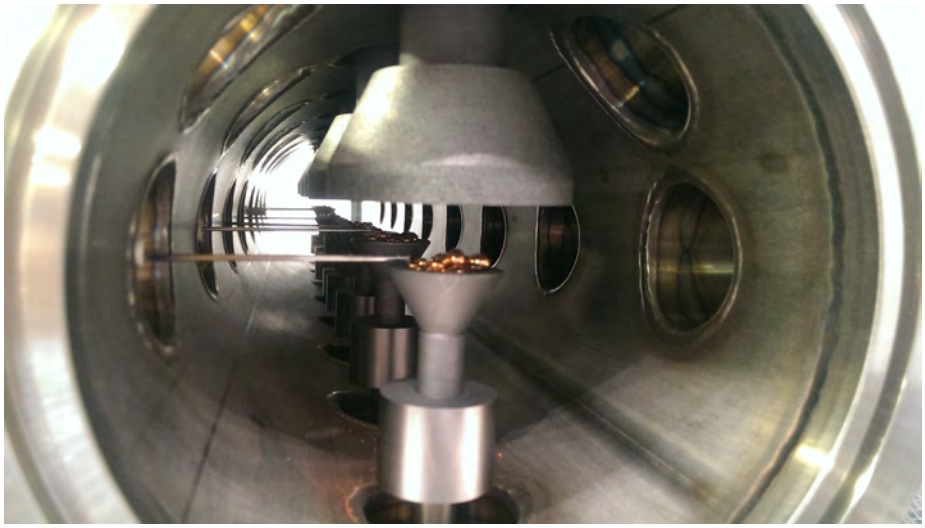

Figure 7.7: *Inner setup of the mOSU*

each material, the filter unit has been designed for copper. Copper is relatively easy to handle, its production rate is the second highest of all tested metals and the process parameters are standard. Furthermore copper is not self inflammable or explosive, at least not at a particle size of 80 nm, which results with the optimal process conditions. Anyway, the design of the filter unit allows rapid changes so also other metals can be used.

The basic idea is to use two filters, so the process can be kept running and does not have to be stopped for filter regeneration. During production, one filter can be regenerated while the particles are deposited in the second one. Figure 7.8 shows a schematic of the filter unit. The particles in the aerosol are transported to the filter unit from the mOSUs and enter filter 1 or filter 2 depending on the inlet valves (G2, G3, G4) position. Inside the filter, particles are separated from the carrier gas by deposition on 4 filter cartridges.

The filter media of the cartridges is a PTFE material (Gore Sinbran Filtration Products, W.L.Gore & Associates GmbH, Putzbrunn, Germany). It has been selected as it has shown a better cleaning performance than metal filters especially for dry-pulse cleaning. The increased surface conductivity reduces static charge effects. Four filter cartridges are arranged in each filter to increase the filtration surface and thereby decrease the surface velocity of the carrier gas, as it would lead to a highly compact cake, which is difficult to clean from the filter cartridges. The filter cartridges are cylindrically shaped with a diameter of 5 cm and a length of 1m. This leads to a filtration surface of 0.16 m^2 per filter cartridge and a filtration surface of 0.64 m^2 per filter housing (4 cartridges). Are the mOSUs operated by the determined optimal flow conditions for e.g. copper (43 l/min per electrode pair) the total gas flow of 688 l/min creates a

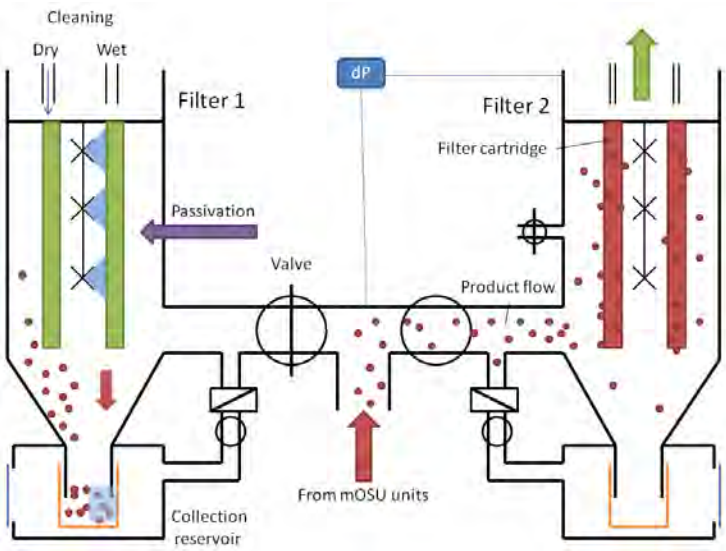

Figure 7.8: *Schematic of the filter unit*

filter face velocity of 1.8 cm/s, which is under a critical filter face velocity of 2 cm/s. Above the critical value of 2 cm/s cleaning becomes much more difficult due to denser cakes at higher velocities. The pressure drop over the filter unit is measured during deposition to monitor the filter loading. Is a maximum pressure drop (approx. 50 mbar) reached, the inlet valves are switched, so that the filter can be regenerated and particle deposition takes place in the second filter.

Filter regeneration is done by either dry-pulse or wet cleaning. Cleaning is always done on filter units, which have been cut off from the main production loop. Figure 7.9 depicts the inner filter setup for cleaning purposes. It is basically an ISO-K-250 O-Ring, which carries the four filter cartridges and the wet cleaning system.

For wet cleaning, the cleaning liquid, e.g. distilled water, is led through Swagelok pipes to the top of the O-ring, where it is separated into four streams, which run through the O-ring down alongside the filter cartridges. The liquid is distributed inside the filter by several Swagelok pipes and crossings and enters the system through multiple nozzles, which spray the liquid conically into the filter housing, ideally washing all particles from the filter and the housing wall down into the collection reservoir. The product resulting from the wet cleaning with distilled water is a non-stable dispersion, of which the copper content depends on the liquid amount used for cleaning. But also dispersants like e.g. ethanol can be used for cleaning. The amount of dispersant can be kept low due to the small throughput of the nozzles. The dispersion can be stabilized and used for different applications afterwards.

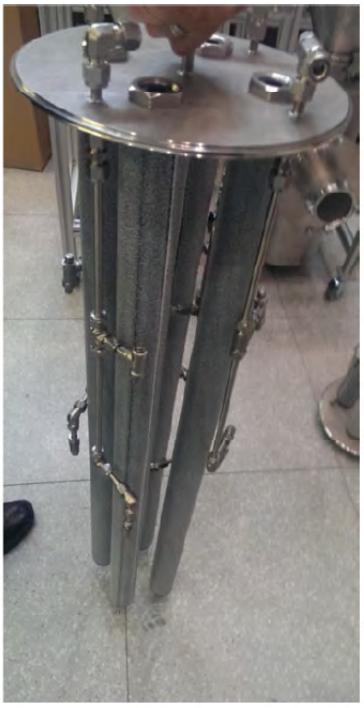

Figure 7.9: *Picture of the inner filter setup including filter cartridges and cleaning setup*

If a powder is desired as a product instead of a dispersion, the filter cartridges can also be cleaned by dry pulsed cleaning. Over each filter cartridge inlet (above the O-ring) a cleaning rod is arranged. The cleaning rod is a rod with a diameter of 16 mm, which is arranged roughly 2 cm above the filter cartridge outlet. At the top of the rod, a nozzle is arranged to increase the pulse peak pressure. The cleaning rods are connected to a pressure tank, each one separated by an electromagnetic valve (R2-R9). If a valve opens (opening time 0.1-0.5 s), part of the pressure tank gas (nitrogen) is pushed trough the valve and the cleaning rod including nozzle, leading to a gas pulse entering the specific filter cartridge. The pulse results in a short expansion of the filter releasing the filter cake from the filter surface, so that it falls down towards the reservoir due to gravity. The sedimentation of the nanoparticles to the bottom of the filter might take several minutes, because of their low effective density. This has to be taken into account before reopening the filter to the production loop.

The choice of the regeneration mode depends mainly on the desired product. As metal nanoparticles can ignite when coming in contact with oxygen, the wet cleaning mode might be beneficial in terms of safety. It also prevents the dust formation and hence minimizes the risk of inhalation. To minimize the risk of exothermic reactions due to surface reactions of the produced particles e.g.

oxidization, passivation has to be performed prior to cleaning. Especially before dry pulse cleaning, it has to be ensured that the particles are passivated with an oxide layer before distributed in the filter housing by the cleaning pulse. In principle no oxygen should be present in the housing, but even small amounts of oxygen might cause severe reactions on distributed pure metal nanoparticles in the gas phase. Also reactions with metal nanoparticle and liquids are possible. Passivation is done by entering a defined mass flow of synthetic air (0.05 to 0.5 l/min) diluted with nitrogen (1 to 10 l/min) into the process for some time. This setup allows a passivation with less than 1000 ppm oxygen. The air streams through the filter cartridges as does the process gas to ensure a good contact of oxygen and particles. The oxygen concentration is slowly increased until the atmospheric level of oxygen is reached in the filter. To prevent the reaction of still unpassivated material, the filter housing can be evacuated and flushed with nitrogen before the actual cleaning procedure.

Independent from the regeneration mode, the product is collected at the bottom of the filter housing. A new bagging approach to collect and store the produced powder after filtration has been developed, which does not separate the filter from the collection reservoir that strictly. In commercial nanoparticle filtration plants, the powder removed from the filter cartridges is at first collected inside the filter housing, before it is guided through a gate of two valves into a reservoir, in which the particles are collected and stored. The separation of the reservoir and the filter housing is necessary to prevent contamination of the filter, as it is usually connected to the rest of the production facility. It also allows filter cleaning at different pressure levels and reduces the risk of powder exposure at failure events. However, it appears that there are no suitable valves for the separating gate, when working with metal nanoparticles. Vacuum-tight ball or slide valves will get damaged when in frequent contact to particulate material. After just a few cycles, the valves tend to clog as the fine particles permeate between the sealing surfaces. An exchange or maintenance of these valves is very expensive. The industry has therefore invented valves, in which the sealing O-ring is not in direct contact with the valve body (ball, slide, etc.) during operation. For sealing, the O-ring is inflated and pressed against the valve body. This procedure reduces the abrasion of the valve body significantly, but at the cost of vacuum tightness. Nevertheless, the tightness of the process is crucial, when working with metal nanoparticles due to their pyrophoric nature.

The idea of the new bagging approach is to eschew the vacuum valves between the filter housing and the reservoir, so that the removed particles from the filter directly sediment into the reservoir, where they may be encapsulated in polymer bags. The vacuum tightness is thereby guaranteed by the standard vacuum components in which the collection procedure takes place. If pulse jet cleaning is performed, it has to be ensured that the pressure pulse, as well as

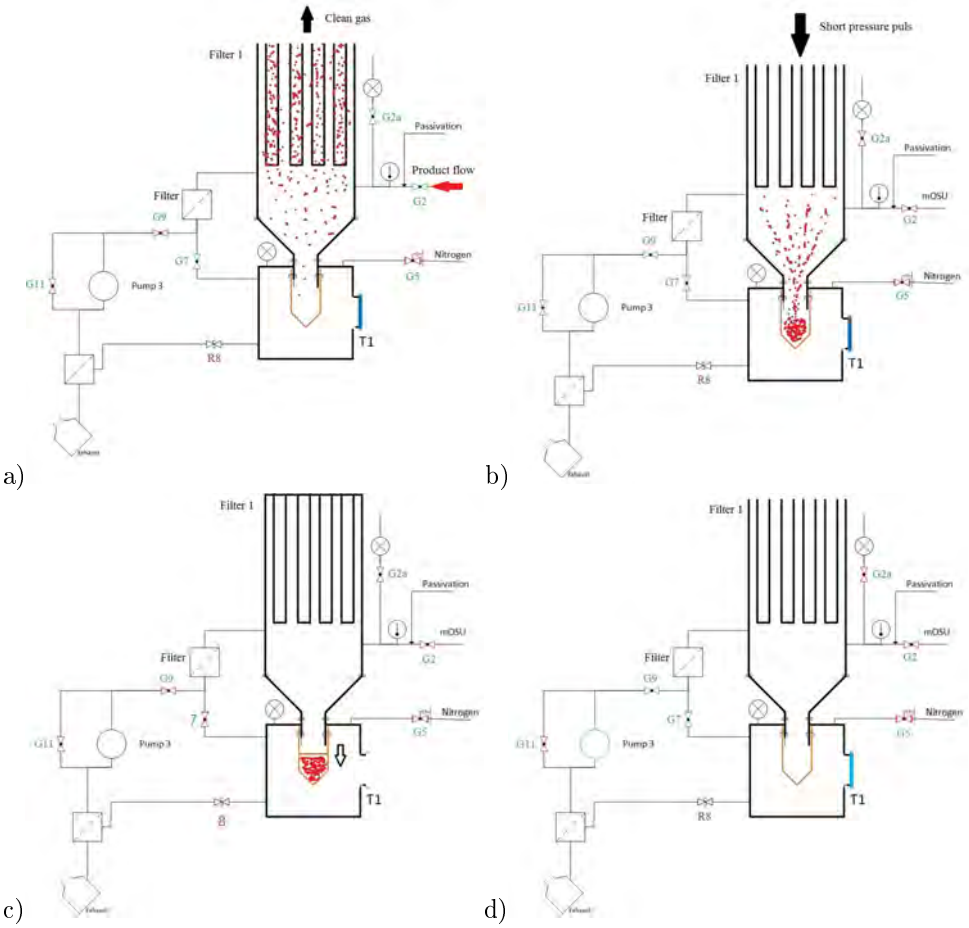

Figure 7.10: *Schematic of the valve-less bagging and collection procedure showing the process during a) filtration, b) cleaning, c) bagging and d) purging*

the additional amount of gas, are led out of the process and do not disrupt the particle collection in the reservoir. The setup of powder collection is depicted in figure 7.10. Here, only the handling of the powder after pulse jet cleaning is discussed, but the procedure for wet cleaning is similar. The numbering of the valves corresponds to the one in the main setup flow chart (figure 7.3). For the sake of generality, the procedure is here discussed for filter 1, but is of course also applicable for filter 2. Only the valves relevant to the bagging process are depicted in figure 7.10. As can be seen, there are no valves between the filter housing and the collection bag (indicated in brown line). The bag is actually a tubular film, which is fixed to a pipe. Several bags can be formed from the film by dragging it down and creating two weld seams above the collected particles. The first weld seam seals the bag with the particles, while the second one acts as a new bottom of the tubular film and hence a new bag.

Figure 7.10a shows the valve positions during filtration in the filter housing. Valves G2 and G2a are process valves and open. Valve G7 is open to keep the pressure in the filter housing and the bagging chamber at the same level in order to avoid deformation of the thin collection bag. The filter in front of valve G7 keeps particles from entering the bagging chamber. Its particle loading should be low as no permanent gas flow runs in that line. Anyway, the loading is checked frequently to keep the differential pressure as low as possible.

By closing the process valves G2 and G2a and starting the cleaning procedure (R-Valves, Figure 7.3), particles are removed from the filter elements and sediment towards the bagging chamber (Figure 7.10b). Valves G9 and G11 are additionally opened before cleaning so that the excess gas, which enters the process during dry-pulse jet cleaning, may exit the housing. This exit could also be realized via the inlet valve G2, but as particles might need to be passivated before cleaning, the additional outlet is needed.

Passivation is not depicted in figure 7.10. It can be done between filtration (a) and cleaning (b), while the particles still remain on the filter elements. The passivating gas enters the filter unit via the passivation line and leaves the unit through the open valves G9 and G11.

Once all particles have settled, all valves are closed. Hatch T1 is then opened and the bag with particles is welded shut and removed by the procedure described above (Figure 7.10c). Since the bagging chamber has to be opened to remove the bag filled with particles, it will be exposed to ambient air.

Due to its housing being filled with air, the bagging chamber has to be evacuated and filled with inert gas to get rid of the oxygen (Figure 7.10d). This is done by pump P1, with valve G7 and G9 being open. To keep the pressure difference over the bag at a minimum, the filter is only evacuated slowly. The filter housing and bagging housing are then carefully filled with inert gas (valve G5) and ready to be used for deposition again.

7.2 Nanoparticle production by the mOSU

Figure 7.11 shows an image of one of the two mOSU units of the production facility during production. Through the eight view-ports, the green light (excited copper atoms) from the eight running arcs is visible. The arcs run stable and show no kind of disruptive interactions with each other. The filtration procedure works also sufficiently. Particles are cleaned by pressure pulse cleaning and drop into the bag. There has been no measurable pressure difference between collection and bagging chamber at any time. The sealing of the bag is easy to perform so that particles (powder) can be removed from the filter unit.

A very important part of the reactor and process design has been its ability to cope with the heat development during processing. Figure 7.12 shows

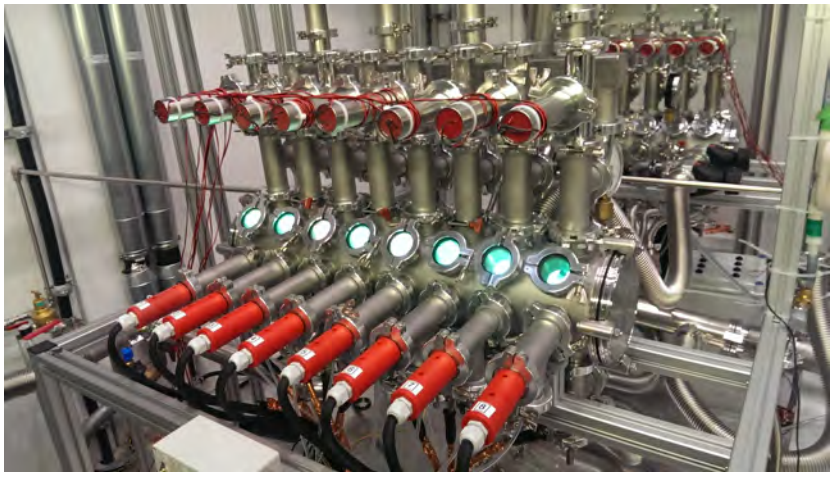

Figure 7.11: *mOSU during production of copper nanoparticles*

the heat development of the process during production at several measurement points. As most of the production facility consist of stainless steel temperatures in the three digit range are noncritical. However, the sealing (O-rings) between the vacuum connections are a made of a PFC material called "Viton", which has a thermal stability of up to 200°C. As can be seen, the maximum reached temperature during production (after 90 minutes) is roughly 100°C, which is measured at the product flow joiners (not cooled) just above the reactor chamber. The reactor chamber itself is water-cooled and stays therefore on a constant temperature level of 21°C. It appears that the temperatures reach an almost stable value after 45 minutes of processing. The product flow combiner is arranged behind the two product flow joiners and combines the product flow of the two mOSUs. The aerosol heats the combiner up to 55°C. The filter inlet is heated up to 50°C, the filter housing of the processed filter heats up to 40°C. The actual gas temperature at that point is assumed to be higher and needs to be evaluated for better understanding of the filtration principle. The second filter housing stays at its initial temperature of 21°C as no gas flow is applied here. The welding generators, which are stored quite closely together show a small increase in temperature (23°C), which is negligible. These results show that the design of the production facility and the selective reactor and gas cooling is working sufficient. The temperature does not exceed any critical values, in contrast the heated process walls might reduce thermophoretic losses of the product.

In order to determine the scalability of the process, the production rate (PR_{total}) and the specific electricity consumption (SEC) are measured for different numbers of running arcs. This is shown in Figure 7.13. As depicted, the production rate increases almost linearly with the number of electrode pairs.

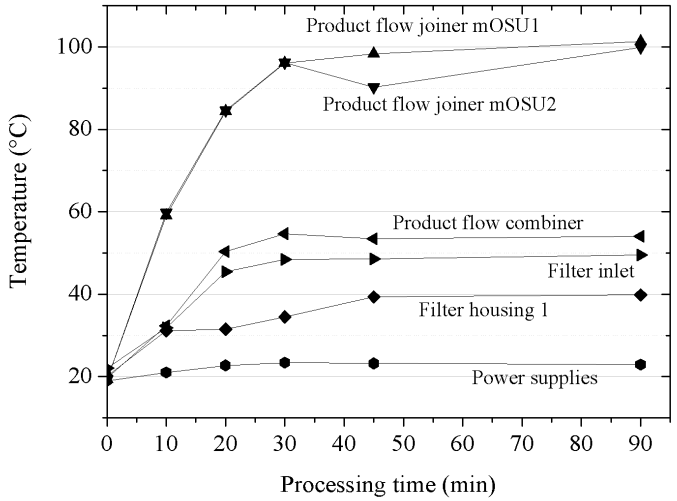

Figure 7.12: *Heat development of the production facility measured at different points*

When one electrode pair is used, a copper nanoparticle production rate of 3.6 g/h is reached. Five electrode pairs in parallel production lead to a production rate of roughly 23 g/h, 10 electrode pairs to 48 g/h. Due to a failure of one electrode pair only 15 electrode pairs could be used as a maximum number of parallel running electrode pairs. With this 15 electrode pairs a maximum production rate of 69 g/h is measured. Small deviations from the linear scaling behavior are a result of changing process conditions, e.g. changing electrode distances due to evaporation and re-feeding of the crucible.

This variation is also visible, when calculating the production rate of each electrode pair. Each electrode pair produces 4.17 g/h ± 0.48 g/h. The OSU delivers with the same parameters (optimal parameters) a mean production rate of 4.1 g/h (see figure 4.29 in chapter 4.5), which is in very good agreement with the scaled up results and hence an indication that the scale-up approach is working. The specific electricity consumption stays almost constant (170 kWh/kg), which is again in good agreement with the lab scale version of the process. The power for pumps etc. are not included in that value, but as only one pump and one cooling method are applied, the overall energy consumption in terms of kWh/kg is expected to be decreasing in comparison to the lab-scale version.

Figure 7.14 shows the number size distribution of the produced copper particles by the production facility as a function of the number of used arcs. The number concentration (arbitrary unit) is shown normalized on the number concentration of the maximum concentration, as the dilution factor of the dilution

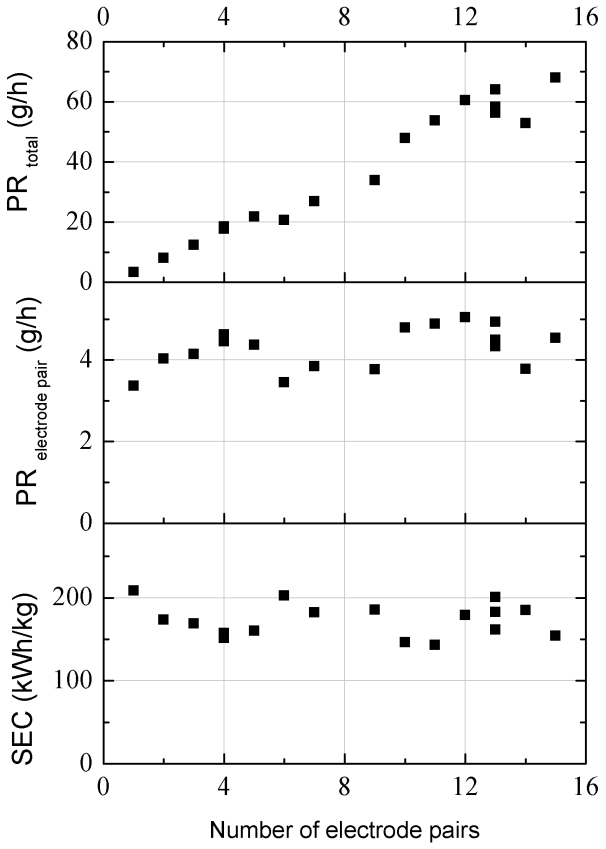

Figure 7.13: *Production rate (PRtotal), production rate per electrode pair (PRelectrode pair) and specific electricity consumption for copper nanoparticle arc synthesis with different numbers of electrode pairs*

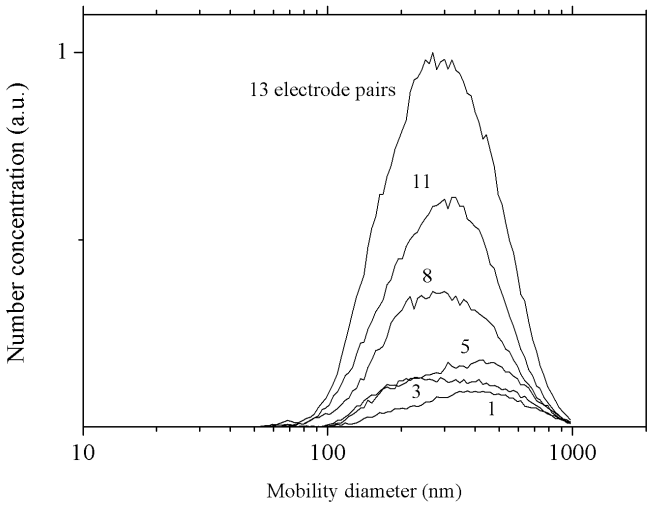

Figure 7.14: *Number size distribution of copper nanoparticles produced by the production facility with varying number of arcs (Total gas flow remains constant)*

system used for this measurement could not be estimated accurately. As depicted, the number concentration increases with the number of electrode pairs. This is a very important result, as the increase of production rate (figure 7.13) needs to be achieved by an increase of number concentration and not particle size. It appears that the number concentration increases almost linearly with the number of electrode pairs.

The number size distribution are broad (gsd 1.53-1.59), which has also been observed for the single OSU unit. The determined mean mobility diameters vary in the range from 271-312 nm, which is sufficiently constant. This value is however twice as big as the determined mobility diameter of the OSU (144 nm). The mobility diameter expresses the agglomerate size of the produced particles and its increase may therefore be reasoned by the increased production and agglomeration rate, when multiple arcs are used. SEM images of the produced agglomerates (13 electrode pairs) shown in figure 7.15 confirm the production of rather large agglomerates, consisting of plenty of primary particles. The residence time of the particles produced in the mOSU is with approximately three seconds 40% shorter than the one of the OSU produced particles, which should result in a decreased agglomeration. It appears that the heat development of the multiple arcs favor the agglomeration.

The primary particle size of the produced copper particles is with 79 nm (BET measurements) slightly smaller than of the OSU (83 nm). The decreased particle size is a result of an increased gas flow per electrode pair. Due to the recirculation system, higher gas flows are applied ($Q_1 \sim 70$ l/min). Smaller

Table 7.2: *Production rate and primary particle size of different metal nanoparticles synthesized by the process. Aluminium synthesized with argon as carrier gas, the other metals with nitrogen. *Estimated for 16 electrode pairs on basis of the production rate of a single OSU (Table 4.3).*

Material	$PR_{single}(g/h)$	$d_P(nm)$	$PR\,(g/day)*$
Copper	4.17	89	1601
Silver	0.9	98	346
Zinc	22.3	180	8563
Aluminium	0.03	9	11.5

particles can be adjusted down to 14 nm with this process by varying the carrier gas composition, applied power or gas flow (see chapter 5). The size reduction is of course on the expense of the production rate. Nevertheless, the scale-up approach is independent of those parameters, so that even increased production rates of smaller particles can be realized. The quality of the produced particles in terms of composition and oxidization seem to be conform to the quality of the OSU.

Concluding the upper results, it can be said that the scale-up approach presented in this study is feasible. A scale-up of production rate of copper nanoparticles has been achieved, while maintaining the primary particle size approximately constant. The scale-up is realized by an increase of number and not the size of nanoparticles. This knowledge allows furthermore an estimation of the production rates of other metals, which have been investigated before with the OSU. The estimation is based on the long term production rates of the OSU (see table 4.3 in chapter 4) and is summarized in Table 7.2. Assuming a production 24 h/day, 1.6 kg of copper nanoparticles with a mean size of 79 nm can be produced. For zinc, this value is with 8.6 kg/day even higher, due its higher vapor pressure. In a nitrogen atmosphere zinc evaporates even at low input power (375 W) intensely, leading to particle sizes out of the nano range. In nitrogen, the production of copper exceeds the one of silver. With the present process 0.35 kg/day silver nanoparticles can be produced. The particle size of silver is with 98 nm still in the nano range. For aluminum, argon has to be used as carrier gas, as it is a nitride forming metal. The use of argon decreases the particle size as well as production rate significantly. 11.5 g/day of 9 nm aluminum nanoparticles can be produced with the present setup. These values are based on the goal of a maximized production rate. The setup allows indeed also the detailed adjustment of particle sizes for all metals.

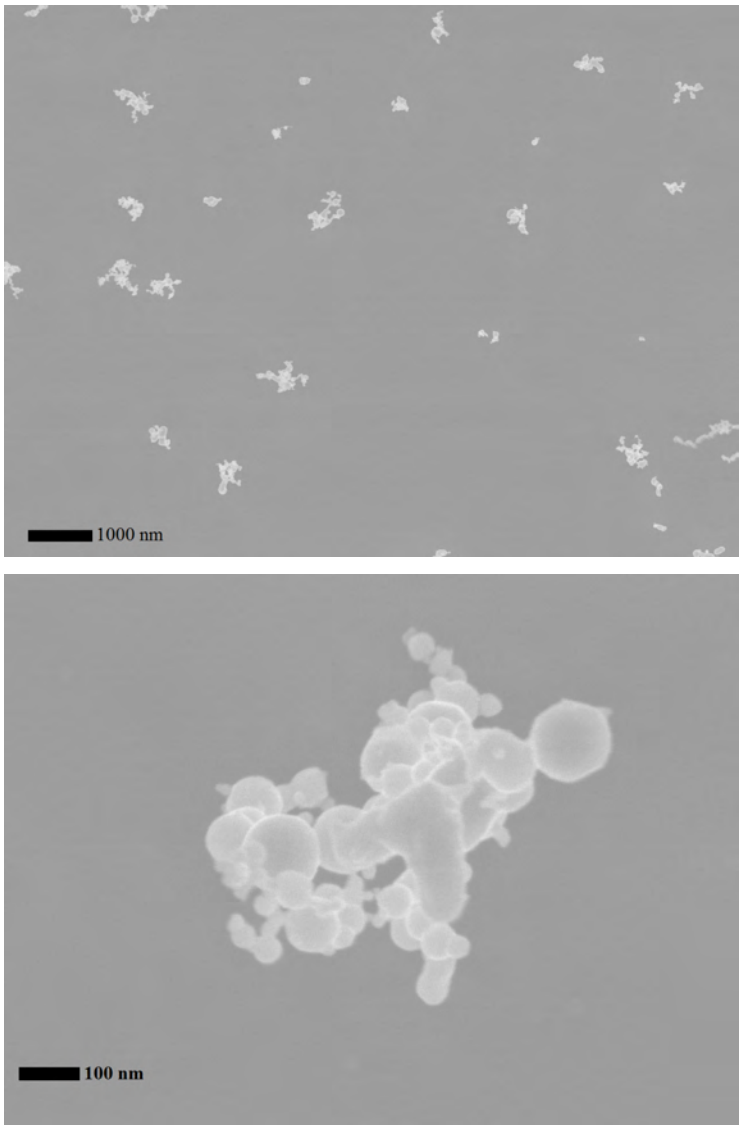

Figure 7.15: *SEM images of produced copper nanoparticles with 13 electrode pairs in the production facility*

Chapter 8

Copper nanoparticle ink prepared from gas-phase synthesized nanoparticles

This chapter presents an application of the nanoparticles produced by the previously described production facility. The application is a printable conductive ink, in this case prepared from copper nanoparticles from the gas phase. Copper inks are already used for ink-jet printing of conductive patterns [68,168]. There are many attempts to produce copper inks [150], however production processes of large quantities of copper nanoparticles at low cost, but high quality for inks are rare [90]. Most of the processes base on chemically controlled reduction of copper precursors and are carried out in the liquid phase. The synthesis in the liquid phase has of course the advantage of directly adding dispersants to the liquid in which the particle formation appears, in order to have it directly stabilized to prevent agglomeration and sedimentation. It further favors a good quality ink due to the absence of oxygen in the liquid phase and hence copper oxide on the surface of the particles. Nevertheless, as the process described in this thesis shows a high output of copper nanopowder, conductive nano-inks from gas phase produced particles are of interest, when they can be brought in dispersion without too much oxygen contamination. The ink then contains only the dispersants and the copper particles without any residual chemicals e.g. from the precursors used in copper nanoparticle production. This chapter reports about the dispersion and printing of a copper nano-ink, produced using the particles from the production facility developed in this work. Films are printed by different techniques, evaluated in terms of electrical conductivity (specific resistivity) and compared to nano-inks produced via wet chemical routes.

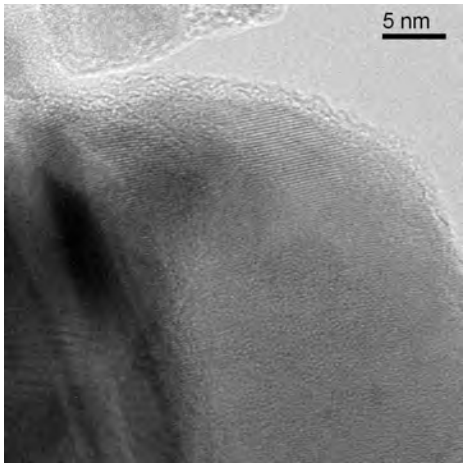

Figure 8.1: *Copper nanoparticle after contact with ambient air*

8.1 Copper nanoparticle ink preparation

This section describes the preparation of the copper nanoparticle ink. The copper nanoparticles have been produced with the setup described in the previous chapter. The mean size of the primary particles is approximately 80 nm. The particles have not been passivated after synthesis, but they obtain an oxide layer, when removing the copper powder from the filter unit. As can be recognized in figure 8.1, the oxide layer on the produced copper nanoparticles is roughly 2 nm.

For this investigation usually dispersions containing 5 g of nanopowder are produced. It has been found that a copper content of 40 wt.% shows good behavior during dispersion, stability of the dispersion and electrical conductivity of the ink. Different main dispersants have been investigated, but some are unsuitable for copper dispersion or lead only to short-term stability of the dispersion and quite fast sedimentation of copper particles. Other dispersants lead to quite stable dispersions, but do not show any electrical conductivity after printing. For the ink produced here, ethanol is used as main dispersant (30 wt.%), with isobutanol (15 wt.%) and glycerol (15 wt.%). This mixture results in a stable dispersion even for weeks and indicates good electrical properties when printed, as shown in the following section. The copper nanopowder and its dispersants are mill grinded by a swing mill (MM400, Retsch GmbH, Haan, Germany) with zirconia beats (0.3 mm) for 3 hours to break soft agglomerates and create a stable dispersion. The specific milling energy is $5.4 \cdot 10^5$ kJ/kg.

The stabilized dispersion is afterwards printed on a glass substrate either by a spin coater (Spin 150, SPS Europe, Putten, Netherlands) or a hand coater. The film is thereby varied depending on the rotating speed of the spin coater. Film thicknesses of 500 to 1000 nm have been adjusted. The hand coater delivers

a film thickness of 500 nm. The ink can be dried at room temperature or on a hot plate to accelerate the drying process. Some printed films have furthermore been sintered in a vacuum furnace for 2 hours at different temperatures (100 to 300 °C) to investigate the influence of sintering on the electrical resistivity. The electrical resistance ($R_\mathrm{f}[\Omega_\square]$) has been measured by the four point probe method using a parameter analyzer (Keithley 4200 SCS, Keithley Instruments Inc, Germering, Germany). The resistivity ($\rho_\mathrm{r}[\Omega\mathrm{cm}]$) is than calculated when multiplying the the resistance R_m with the film thickness l_f, which is determined by a profilometer in advance (Ambios XP-200, Ambios Technology Inc., Santa Cruz, CA, USA):

$$\rho_\mathrm{r} = R_\mathrm{f} l_\mathrm{f} \tag{8.1}$$

8.2 Performance of the printed conductive films prepared from the copper nanoparticle ink

The produced ink is easily distributed on the substrate by the spin or hand coater and completely dried on a hot plate after 5 minutes. Figure 8.2 shows the thicknesses of the printed films on a glass substrate by spin coating and the hand coater and its influence on the electrical resistivity. The hand coater delivers a film thickness of approx. 570 nm. The film is therefore 14% thicker as the manufacture information indicates. With the spin coater film thicknesses between 500 and 1000 nm are realized. It appears that the resistivity depends on the film thickness although it should theoretically be independent of the thickness and a material constant. It ranges from 0.3 Ωcm at a film thickness of 510 nm to $1.7 \cdot 10^{-3}$ Ωcm at a film thickness of 950 nm. The dependence of the film thickness on the resistivity might be a consequence of inhomogeneities in the printed film, such as boundary surface effects or cracks in the printed film, which become less influential with increasing film thickness [72,118].

The electrical resistivity of copper as bulk material at room temperature is $1.7 \cdot 10^{-6}$ Ωcm, hence a factor of 1000 less, than the printed film. In order to improve the resistivity of the printed films, sintering is applied by a vacuum furnace to the sample with the film thickness of 510 nm for 2 hours at three different temperatures. The result is depicted in figure 8.3. The resistivity significantly decreases with the applied sintering temperature. Already at a sintering temperature of 100°C, the resistivity is decreased by factor of 6. At 200°C the resistivity is with $6 \cdot 10^{-5}$ Ωcm even reduced by factor of 5000 and only 30 times larger than the resistivity of the bulk copper. The SEM images clearly show a more homogenous structure and film after sintering, which improves the conductivity. The value of $6 \cdot 10^{-5}$ Ωcm is in the order of magnitude of printed copper patterns by other researchers via the wet chemical route after

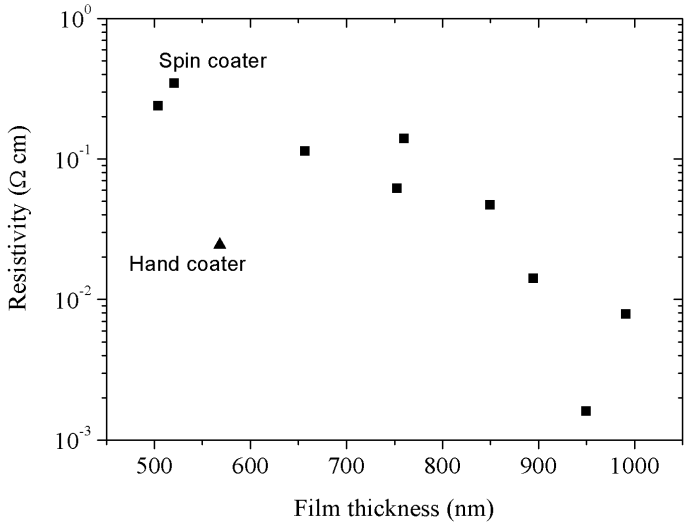

Figure 8.2: *Electrical resistivity of printed copper film in dependency of the film thickness*

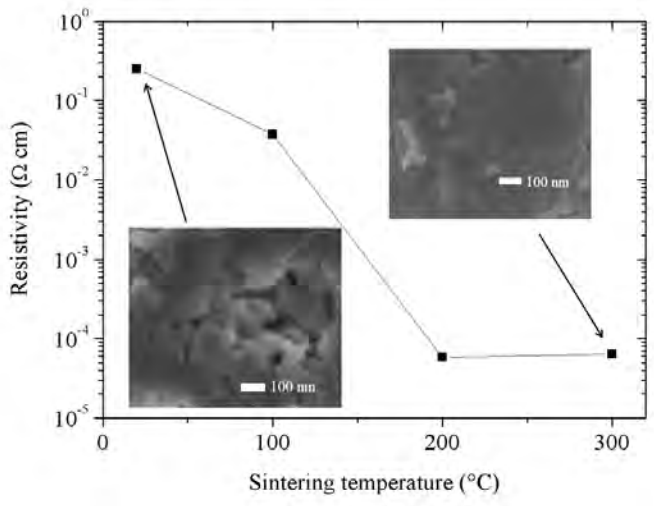

Figure 8.3: *Resistivity of printed copper ink depending on sintering temperature using initial film thickness of 510 nm*

Table 8.1: *Comparison of the electrical resistivity of the printed films to literature data.*

Author	Particle size	Film thickness	Sintering	Resistivity
Haynes et al. [160]	bulk copper	-	-	$1.7 \cdot 10^{-6}\,\Omega$cm
Kang et al. [72]	10 nm	3736 nm	at 200°C	$3.6 \cdot 10^{-6}\,\Omega$cm
	10 nm	10926 nm	at 200°C	$7.9 \cdot 10^{-6}\,\Omega$cm
Lee et al. [90]	55 nm	-	at 200°C	$3.6 \cdot 10^{-6}\,\Omega$cm
Jeong et al. [70]	60 nm	-	at 275°C	$1.1 \cdot 10^{-5}\,\Omega$cm
Park et al. [119]	45 nm	800 nm	at 350°C	$1.7 \cdot 10^{-5}\,\Omega$cm
This work	80 nm	500 nm	at 300°C	$6 \cdot 10^{-5}\,\Omega$cm

sintering [70, 119]. Table 8.1 compares the electrical resistivity of printed films from literature data and this work. As the table indicates, there are several parameters, which effect the resistivity of the printed films. It appears that the use of smaller particles in an ink decreases the resistivity of a printed film strongly. Furthermore, an increased film thickness seems to improve the conductivity, which also has been found in this work. Sintering has been applied by all researches in order to optimize the resistivity of the printed films. Beside the shown parameters, also the oxide layer on the particles, the dispersant, the copper content in the ink and the printing technique influence the resistivity strongly.

Beside the conductivity of the printed films itself, the long-term stability of the conductivity is very important, as it dictates the lifetime of the printed structures or devices. Figure 8.4 shows the resistivity of the printed copper ink, sintered and not sintered over a duration of 180 days. The resistivity of the printed films has increased for the not sintered film by factor of 4 after 180 days. For the sintered film the resistivity has increased by factor of 2.8 to a value of $2 \cdot 10^{-4}\,\Omega$cm, so that it still can be seen as an electrical conductor [64].

Generally one can conclude that copper ink prepared from gas-phase produced particles is competitive to inks produced in the liquid phase in terms of resistivity of the printed layer and long-term stability of the resistivity. The resistivity of the films printed in this work might be improved, when sintering is applied to the sample with the film thickness of 950 nm. As this has not been a major goal of this thesis, further optimization in order to come to a smaller resistivity should be carried out in the future. Further improvement of the conductivity can probably also be achieved by minimizing the oxygen contamination of the copper powder and therefore the oxide layer on the particles. This can be done by e.g. creating the dispersion inside a glove box. Furthermore, an ink consisting of smaller particles might decrease the resistivity further, due to the larger surface of the particles and therefore better inter-particle connections.

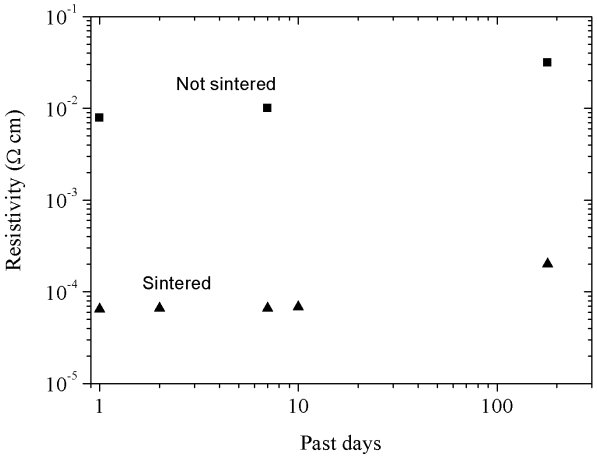

Figure 8.4: *Resistivity of the printed copper ink, initially sintered and not sintered over a duration of 180days*

Chapter 9

Conclusions

In this work a metal nanoparticle production process is developed, with the goal of scaling up the production rate of metal nanoparticles and at the same time keeping the specific electricity consumption low. Several aspects of the production process are investigated, namely the optimization of particle synthesis, the formation and characterization of nanoparticles in the gas phase and the scale-up behavior of the process.

A versatile, efficient and sustainable production process for metal nanoparticle synthesis is developed. The basic process is the transferred arc synthesis: a gas phase process in which metal nanoparticles are formed due to the evaporation of a bulk material and following condensation, nucleation, coagulation and sintering. No chemical precursors are used. The transferred arc is ignited between a tungsten rod cathode and a graphite crucible anode, which carries the material to be evaporated. The process takes place inside a reactor chamber, which allows beside the attachment of the process dependent connections (power, gas flow, material feeding) further adjustment of measurement equipment or monitoring devices. The reactor chamber and all kind of connections are built of standard vacuum components, to ensure good quality and handability of the production. The process has received intense optimization in terms of production rate (g/h) of metal nanoparticles, specific electricity consumption (kWh/kg) and primary particle size (nm). Different electrode positions and forms (crucible design) are investigated in combination with varying gas flow directions. In order to increase the evaporation rate, a crucible with a reduced middle part is found to be beneficial due to the reduced heat losses. A graphite hood arranged atop of the crucible reduces the particle losses and thereby increases the production rate significantly. It is found that a main gas flow (20 to 50 l/min) from the bottom streaming alongside the crucible, in combination with a smaller cross gas flow (0 to 3 l/min) coming from the side, streaming along the tungsten rod cathode results in an increased production rate. Furthermore, the

influence of the carrier gas composition is investigated. For non-nitride forming metals, nitrogen is by far the most efficient carrier gas, which appears to be a result of increased thermal, decreased electrical conductivity and a bubble formation effect inside the melt. Another influencing parameter is the applied electric current (power). The production rate increases significantly with the applied current. However, this increase in production rate goes along with an increase in primary particle size, which limits the scale-up of production rate by the power input, as a maximal particle size of 100 nm is given. A dedicated feeding mechanism is developed to feed material into the crucible and restore the evaporated amount during production. With the feeding mechanisms process runs of up to 8 hours have been achieved.

A novel online monitoring procedure to determine the primary particle size of the formed particles online via parallel SMPS and ELPI measurement is found. It bases on a fitting procedure of the two size distributions obtained by ELPI and SMPS. The fitting parameter is thereby the effective density of the measured aerosol agglomerates. An equation is found to calculate the mass mobility exponent of agglomerates on the basis of the determined effective density, which allows a direct estimation of the primary particle size. The determined particle sizes are confirmed by TEM measurements. In addition, a proximity sampling technique is used to determine the primary particle size ex-situ close to the arc, in order to gain further information about the particle formation process. It is found that the sampling technique is capable of measuring the primary particle size during growth in a transferred arc process. According to this, copper nanoparticles achieve their final size already 2 cm distant from the arc. Already at the closest possible measurement position, which is specified by the electrode distance, particles have reached 49% of their final size. The large amount of evaporated material due to the arc leads to a supersaturation and hence nucleation even at relatively high temperatures.

In order to understand the formation process of the particles in the present process, sintering parameters (activation energy and sinter kinetic constant) of the metals worked with in this study are determined. The sintering parameters describe the effect of sintering due to grain boundary, surface and volume diffusion. They are obtained based on a fitting procedure of experimental data from a tandem-DMA setup combined with a sintering furnace. It appears that there is a general activation energy needed to start the sintering process, as the activation energies of the single metals does not differ that strongly. The sinter kinetic constant shows a congruence with the metals density, which influences the heat capacity of the metal. The sintering parameters are afterwards used in a simple model based on CFD data of the present process to describe the formation of metal nanoparticles. The model describes the formation of nanoparticles in terms of particles size due to nucleation, coagulation, agglomeration and sinter-

ing. The particle sizes predicted by the model underestimate the experimentally determined values slightly, which is found to be a consequence of a decreased temperature profile in the model. The evolution of particle size however appears to be described well by the model.

A production facility has been built to scale-up the production rate of metal nanoparticles. The scale-up principle is thereby the parallelization of multiple transferred arcs in one housing (mOSU). The production facility consists of a production area (two mOSUs), a filtration unit and a gas reconditioning area and is built for large scale nanoparticle production. It is shown that the scale-up approach of multiple transferred arc synthesis is working. The production rate multiplies with the number of running arcs, while the primary particle size remains almost constant. The increase in production rate results therefore from an increase in particle number concentration. Copper nanoparticles with a mean primary particle size of 79 nm have been produced with a production rate of 69 g/h. The main goal of this work, which is the scale-up of metal nanoparticles is hence achieved. As the production facility shows a good predictability, further production rates of other metals are estimated, as the production rate of the single transferred arc (OSU) for the respective metal is known.

In order to show an application of the produced particles, a conductive copper ink is formed by dispersing produced copper nanoparticles. The ink is therefore made from gas phase produced particles. It is printed on a glass substrate by hand or spin coating. The electrical resistivity of the printed films is dependent of the film thickness, which might be a consequence of the inhomogeneities of the printed film. Sintered films at 300°C show strongly decreased electrical resistivities, which are approximately 30 times higher than the resistivity of bulk copper and comparable to copper inks produced in the liquid phase. The printed films retain their electrical properties even for months, so it can be expected that these copper inks with further optimization and investigation can become a real alternative to the commercially available inks.

Bibliography

[1] G. Allen, C. Sioutas, P. Koutrakis, R. Reiss, F. W. Lurmann, and P. T. Roberts. Evaluation of the teom method for measurement of ambient particulate mass in urban areas. *Journal of the Air and Waste Management Association*, 47(6):682–689, 1997.

[2] M. D. Allen and O. G. Raabe. Slip correction measurements for aerosol particles of doublet and triangular triplet aggregates of spheres. *Journal of Aerosol Science*, 16(1):57–67, 1985.

[3] A. Anders. Tracking down the origin of arc plasma science-ii. early continuous discharges. *IEEE Transactions on Plasma Science*, 31(5):1060–1069, 2003.

[4] R. J. Anthony, D. J. Rowe, M. Stein, J. Yang, and U. Kortshagen. Routes to achieving high quantum yield luminescence from gas-phase-produced silicon nanocrystals. *Advanced Functional Materials*, 21(21):4042–4046, 2011.

[5] O. I. Arabi-Katbi, S. E. Pratsinis, P. W. Morrison, and C. M. Megaridis. Monitoring the flame synthesis of tio2 particles by in-situ ftir spectroscopy and thermophoretic sampling. *Combustion and Flame*, 124(4):560–572, 2001.

[6] G. P. Ayers, M. D. Keywood, and J. L. Gras. Teom vs. manual gravimetric methods for determination of pm2.5 aerosol mass concentrations. *Atmospheric Environment*, 33(22):3717–3721, 1999.

[7] P. A. Baron and K. Willeke. *Aerosol measurement: Principles, techniques, and applications.* Wiley, New York, 2 edition, 2001.

[8] Bertelsmann. Chronik 2013 kalender: Wissensmedia.

[9] Borm, P. J. A., D. Robbins, S. Haubold, T. Kuhlbusch, H. Fissan, K. Donaldson, R. Schins, V. Stone, W. Kreyling, J. Lademann, J. Krutmann, D. Warheit, and E. Oberdorster. The potential risks of nanomaterials: a review carried out for ecetoc. *Particle and Fibre Toxicology*, 3(1):11, 2006.

[10] M.I Boules, J. Jurewicz, and J. Guo. Induction plasma synthesis of nanopowders. patentnumber 8013269 b2.

[11] J. R. Brenner, J. B. L. Harkness, M. B. Knickelbein, G. K. Krumdick, and C. L. Marshall. Microwave plasma synthesis of carbon-supported ultrafine metal particles. *Nanostructured Materials*, 8(1):1–17, 1997.

[12] S. Brunauer, P. H. Emmett, and E. Teller. Adsorption of gases in multimolecular layers. *Journal of the American Chemical Society*, 60(2):309–319, 1938.

[13] H. Burtscher. Physical characterization of particulate emissions from diesel engines: A review. *Journal of Aerosol Science*, 36(7):896–932, 2005.

[14] C. Celik, T. Addona, M.I Boulos, G. Chen, and H.J Davis. Method and transferred arc plasma system for production of fine and ultrafine powders. patentnumber 6379419b1.

[15] D.-R Chen, D. Y. H. Pui, D. Hummes, H. Fissan, F. R. Quant, and G. J. Sem. Design and evaluation of a nanometer aerosol differential mobility analyzer (nano-dma). *Journal of Aerosol Science*, 29(5-6):497–509, 1998.

[16] J. Chen, G. Lu, L. Zhu, and R. C. Flagan. A simple and versatile mini-arc plasma source for nanocrystal synthesis. *Journal of Nanoparticle Research*, 9(2):203–213, 2007.

[17] X. Chen and S. S. Mao. Titanium dioxide nanomaterials: Synthesis, properties, modifications, and applications. *Chemical Reviews*, 107(7):2891–2959, 2007.

[18] K. Cho and P. Biswas. A geometrical sintering model (gsm) to predict surface area change. *Journal of Aerosol Science*, 37(10):1378–1387, 2006.

[19] K. Cho and P. Biswas. Sintering rates for pristine and doped titanium dioxide determined using a tandem differential mobility analyzer system. *Aerosol Science and Technology*, 40(5):309–319, 2006.

[20] M. Choi, J. Cho, J. Lee, and H.W. Kim. Measurements of silica aggregate particle growth using light scattering and thermophoretic sampling in a coflow diffusion flame. *Journal of Nanoparticle Research*, 1(2):169–183, 1999.

[21] J. C. Chow. Measurement methods to determine compliance with ambient air quality standards for suspended particles. *Journal of the Air and Waste Management Association*, 45(5):320–382, 1995.

[22] A. Chung, D. P. Y. Chang, M. J. Kleeman, K. D. Perry, T. A. Cahill, D. Dutcher, E. M. McDougall, and K. Stroud. Comparison of real-time instruments used to monitor airborne particulate matter. *Journal of the Air and Waste Management Association*, 51(1):109–120, 2001.

[23] W. S. Coblenz. The physics and chemistry of the sintering of silicon. *Journal of Materials Science*, 25(6):2754–2764, 1990.

[24] J. J. Cole, E.-C. Lin, C. R. Barry, and H. O. Jacobs. Continuous nanoparticle generation and assembly by atmospheric pressure arc discharge. *Applied Physics Letters*, 95(11):113101, 2009.

[25] S. Cozzens, R. Cortes, O. Soumonni, and T. Woodson. Nanotechnology and the millennium development goals: water, energy, and agri-food. *Journal of Nanoparticle Research*, 15(11), 2013.

[26] Y. Cressault, R. Hannachi, Ph Teulet, A. Gleizes, J-P Gonnet, and J-Y Battandier. Influence of metallic vapours on the properties of air thermal plasmas. *Plasma Sources Science and Technology*, 17(3):035016, 2008.

[27] M.-C Daniel and D. Astruc. Gold nanoparticles: Assembly, supramolecular chemistry, quantum-size-related properties, and applications toward biology, catalysis, and nanotechnology. *Chemical Reviews*, 104(1):293–346, 2004.

[28] H. Davy. On some chemical agencies of electricity: Bakerian lecture of 1807. *Phil. Trans. Roy. Soc.*, (97):1–56, 1807.

[29] R. A. Dobbins and C. M. Megaridis. Morphology of flame-generated soot as determined by thermophoretic sampling. *Langmuir*, 3(2):254–259, 1987.

[30] J. A. Eastman, S. U. S. Choi, S. Li, W. Yu, and L. J. Thompson. Anomalously increased effective thermal conductivities of ethylene glycol-based nanofluids containing copper nanoparticles. *Applied Physics Letters*, 78(6):718–720, 2001.

[31] M. L. Eggersdorfer, A. J. Gröhn, C. M. Sorensen, P. H. McMurry, and S. E. Pratsinis. Mass-mobility characterization of flame-made zro 2 aerosols: Primary particle diameter and extent of aggregation. *Journal of Colloid And Interface Science*, 387(1):12–23, 2012.

[32] K. Etemadi and E. Pfender. Impact of anode evaporation on the anode region of a high-intensity argon arc. *Plasma Chemistry and Plasma Processing*, 5(2):175–182, 1985.

[33] P. Fauchais. Understanding plasma spraying. *Journal of Physics D: Applied Physics*, 37(9):R86–R108, 2004.

[34] P. Fauchais and A. Vardelle. Thermal plasmas. *IEEE Transactions on Plasma Science*, 25(6):1258–1280, 1997.

[35] F. Faupel, W. Frank, M.P. Macht, H. Mehrer, V. Naundorf, K. Rätzke, H. Schober, S. Sharma, and H. Teichler. Diffusion in metallic glasses and supercooled melts. *Reviews of Modern Physics*, 75(1):237–280, 2003.

[36] D. L. Feldheim and C. A. Foss. *Metal nanoparticles: Synthesis, characterization, and applications.* Marcel Dekker, New York, 2002.

[37] H. Fissan, D. Hummes, F. Stratmann, P. Büscher, S. Neumann, D. Y. H. Pui, and D. Chen. Experimental comparison of four differential mobility analyzers for nanometer aerosol measurements. *Aerosol Science and Technology*, 24(1):1–13, 1996.

[38] H. Förster. *Synthese und Beschichtung metallischer Nanopartikel in der Gasphase.* PhD thesis, University of Erlangen, 2013.

[39] H. Förster, C. Wolfrum, and W. Peukert. Experimental study of metal nanoparticle synthesis by an arc evaporation/condensation process. *Journal of Nanoparticle Research*, 14(7):926–941, 2012.

[40] S. K. Friedlander. *Smoke, dust, and haze: Fundamentals of aerosol dynamics.* Oxford University Press, New York, 2. edition, 2000.

[41] O. Fukumasa, T. Fujiwara, Sakuta T, Fujiama H, and Adachi K. Rapid synthesis of ferrite particles from powder mixtures using thermal plasma processing. *Thin Solid Films*, 435(1-2):33–38, 2003.

[42] B. Fultz and James M. Howe. *Transmission electron microscopy and diffractometry of materials.* Springer, Berlin and New York, 3. edition, 2008.

[43] S. Furukawa, T. Amakawa, and K. Adachi. Effects of copper vapor on heat transfer from atmospheric nitrogen plasma to a molten metal anode. *Plasma Chemistry and Plasma Processing*, 22(1):85–104, 2002.

[44] D. Gautam, M. Engenhorst, C. Schilling, G. Schierning, R. Schmechel, and M. Winterer. Thermoelectric properties of pulsed current sintered nanocrystalline al-doped zno by chemical vapour synthesis. *J. Mater. Chem. A*, 3(1):189–197, 2014.

[45] R. M. German. *Sintering theory and practice.* Wiley, New York, 1996.

[46] S. L. Girshick and C.-P Chiu. Homogeneous nucleation of particles from the vapor phase in thermal plasma synthesis. *Plasma Chemistry and Plasma Processing*, 9(3):355–369, 1989.

[47] H.R. Griem. *Plasma spectroscopy*. McGraw-Hill, New York, 1964.

[48] J. Haidar. Non-equilibrium modelling of transferred arcs. *Journal of Physics D: Applied Physics*, 32(3):263–272, 1999.

[49] J. Haidar. Synthesis of al nanopowders in an anodic arc. *Plasma Chemistry and Plasma Processing*, 29(4):307–319, 2009.

[50] R. M. Harrison, M. Jones, and G. Collins. Measurements of the physical properties of particles in the urban atmosphere. *Atmospheric Environment*, 33(2):309–321, 1999.

[51] K. He, F. Yang, Y. Ma, Q. Zhang, X. Yao, C. K. Chan, S. Cadle, T. Chan, and P. Mulawa. The characteristics of pm2.5 in beijing, china. *Atmospheric Environment*, 35(29):4959–4970, 2001.

[52] J. Heberlein. New approaches in thermal plasma technology. *Pure and Applied Chemistry*, 74(3):327–335, 2002.

[53] J. Heberlein, O. Postel, S. Girshick, P. McMurry, W. Gerberich, D. Iordanoglou, F. Di Fonzo, D. Neumann, A. Gidwani, M. Fan, and N. Tymiak. Thermal plasma deposition of nanophase hard coatings. *Surface and Coatings Technology*, 142-144:265–271, 2001.

[54] C. Helsper, W. Mölter, and P. Haller. Representative dilution of aerosols by a factor of 10,000. *Journal of Aerosol Science*, 21(1):637–640, 1990.

[55] M. Heurlin, M. H. Magnusson, D. Lindgren, M. Ek, L. R. Wallenberg, K. Deppert, and L. Samuelson. Continuous gas-phase synthesis of nanowires with tunable properties. *Nature*, 492(7427):90–94, 2012.

[56] L. M. Hildemann, G. R. Markowski, and G. R. Cass. Chemical composition of emissions from urban sources of fine organic aerosol. *Environmental Science & Technology*, 25(4):744–759, 1991.

[57] W. C. Hinds. *Aerosol technology: Properties, behavior, and measurement of airborne particles*. Wiley, New York, 2. edition, 1999.

[58] P. H. Hoet, I. Brüske-Hohlfeld, and O. V. Salata. Nanoparticles – known and unknown health risks. *Journal of Nanobiotechnology*, 2(1):12, 2004.

[59] R.E. Honig and D.A. Kramer. Vapor pressure data for the solid and liquid elements. *RCA Review*, (30):285–305, 1969.

[60] E. Hontañón, J. M. Palomares, M. Stein, X. Guo, R. Engeln, H. Nirschl, and F. E. Kruis. The transition from spark to arc discharge and its implications with respect to nanoparticle production. *Journal of Nanoparticle Research*, 15(9), 2013.

[61] G. L. Hornyak. *Introduction to nanoscience and nanotechnology.* Taylor & Francis, Boca Raton, 2009.

[62] J. Hu, T. W. Odom, and C. M. Lieber. Chemistry and physics in one dimension: Synthesis and properties of nanowires and nanotubes. *Accounts of Chemical Research*, 32(5):435–445, 1999.

[63] D. Hummes, S. Neumann, H. Fissan, D. R. Chen, D. Y. H. Pui, F. R. Quant, and G. J. Sem. Nanometer differential mobility analyzer (nanodma): Experimental evaluation and performance verification. *Journal of Aerosol Science*, 27(1):135–136, 1996.

[64] S. Hunklinger. *Festkörperphysik.* Oldenbourg, München, 2. edition, 2009.

[65] A. J. Hurd and W. L. Flower. In situ growth and structure of fractal silica aggregates in a flame. *Journal of Colloid And Interface Science*, 122(1):178–192, 1988.

[66] P. K. Jain, X. Huang, I. H. El-Sayed, and M. A. El-Sayed. Review of some interesting surface plasmon resonance-enhanced properties of noble metal nanoparticles and their applications to biosystems. *Plasmonics*, 2(3):107–118, 2007.

[67] P. K. Jain, X. Huang, I. H. El-Sayed, and M. A. El-Sayed. Noble metals on the nanoscale: Optical and photothermal properties and some applications in imaging, sensing, biology, and medicine. *Accounts of Chemical Research*, 41(12):1578–1586, 2008.

[68] S. Jang, Y. Seo, J. Choi, T. Kim, J. Cho, S. Kim, and D. Kim. Sintering of inkjet printed copper nanoparticles for flexible electronics. *Scripta Materialia*, 62(5):258–261, 2010.

[69] G. Janzen. *Plasmatechnik: Grundlagen, Anwendungen, Diagnostik.* Hüthig Buch Verlag, Heidelberg, 1992.

[70] S. Jeong, K. Woo, D. Kim, S. Lim, J. S. Kim, H. Shin, Y. Xia, and J. Moon. Controlling the thickness of the surface oxide layer on cu nanoparticles for the fabrication of conductive structures by ink-jet printing. *Advanced Functional Materials*, 18(5):679–686, 2008.

[71] S. B. Jerez, Y. Zhang, J. W. McClure, L. Jacobson, A. Heber, J. Koziel, S. Hoff, and D. Beasley. Comparison of total suspended particulate concentration using tapered element oscillating microbalance and a tsp sampler. In *Proceedings of the Air and Waste Management Association's Annual Meeting and Exhibition : Proc. A Waste Manage. Assoc. Annu. Meet.*

Exhib, Proceedings of the A and WMA's 97th Annual Conference and Exhibition; Sustainable Development: Gearing Up for the Challenge, pages 2059–2070, Indianapolis and IN, 2004.

[72] J. S. Kang, H. S. Kim, J. Ryu, H. Thomas, S. Jang, and J. W. Joung. Inkjet printed electronics using copper nanoparticle ink. *Journal of Materials Science: Materials in Electronics*, 21(11):1213–1220, 2010.

[73] M. N. A. Karlsson, K. Deppert, L. S. Karlsson, M. H. Magnusson, J.-O Malm, and N. S. Srinivasan. Compaction of agglomerates of aerosol nanoparticles: A compilation of experimental data. *Journal of Nanoparticle Research*, 7(1):43–49, 2005.

[74] P. B. Keady, F. R. Quant, and G. J. Sem. Automated differential mobility particle sizer. *Aerosols*, pages 71–74, 1984.

[75] J. Keskinen, K. Pietarinen, and M. Lehtimäki. Electrical low pressure impactor. *Journal of Aerosol Science*, 23(4):353–360, 1992.

[76] H. S. Kim, Ho Lee, Kyu-Sung Han, Jin-Ho Kim, Min-Sang Song, Min-Sik Park, Jai-Young Lee, and Jeung-Ku Kang. Hydrogen storage in ni nanoparticle-dispersed multiwalled carbon nanotubes. *The Journal of Physical Chemistry B*, 109(18):8983–8986, 2005.

[77] S. C. Kim, J. Wang, M. S. Emery, W. G. Shin, G. W. Mulholland, and D. Y. H. Pui. Structural property effect of nanoparticle agglomerates on particle penetration through fibrous filter. *Aerosol Science and Technology*, 43(4):344–355, 2009.

[78] C. Knieke, M. Sommer, and W. Peukert. Identifying the apparent and true grinding limit. *Powder Technology*, 195(1):25–30, 2009.

[79] E. O. Knutson and K. T. Whitby. Aerosol classification by electric mobility: apparatus, theory, and applications. *Journal of Aerosol Science*, 6(6):443–451, 1975.

[80] N. Kobayashi, Y. Kawakami, K. Kamada, J.-G Li, R. Ye, T. Watanabe, and T. Ishigaki. Spherical submicron-size copper powders coagulated from a vapor phase in rf induction thermal plasma. *Thin Solid Films*, 516(13):4402–4406, 2008.

[81] W. Koch and S. K. Friedlander. The effect of particle coalescence on the surface area of a coagulating aerosol. *Journal of Aerosol Science*, 20(8):891–894, 1989.

[82] W. Koch and S. K. Friedlander. The effect of particle coalescence on the surface area of a coagulating aerosol. *Journal of Colloid And Interface Science*, 140(2):419–427, 1990.

[83] W. Koch, H. Lödding, W. Mölter, and F. Munziger. Verdünnungssystem für die messung hochkonzentrierter aerosole mit optischen partikelzählern. *Staub-Reinhaltung der Luft*, (48):341–344, 1988.

[84] U. Kortshagen. Nonthermal plasma synthesis of semiconductor nanocrystals. *Journal of Physics D: Applied Physics*, 42(11):113001, 2009.

[85] Ü.Ö. Köylü, C.S. McEnally, D.E. Rosner, and L.D. Pfefferle. Simultaneous measurements of soot volume fraction and particle size / microstructure in flames using a thermophoretic sampling technique. *Combustion and Flame*, 110(4):494–507, 1997.

[86] F. E. Kruis. *Particle Formation in a Laser-heated Aerosol Reactor: Application to Silicon and Silicon nitride Synthesis*. PhD thesis, 1993.

[87] F. E. Kruis, K. A. Kusters, S. E. Pratsinis, and B. Scarlett. A simple model for the evolution of the characteristics of aggregate particles undergoing coagulation and sintering. *Aerosol Science and Technology*, 19(4):514–526, 1993.

[88] Kuhlbusch, T. A. J., C. Asbach, H. Fissan, D. Göhler, and M. Stintz. Nanoparticle exposure at nanotechnology workplaces: A review. *Particle and Fibre Toxicology*, 8(1):22, 2011.

[89] J.-G. Lee, P. Li, C.-J. Choi, and X.-L. Dong. Synthesis of mn–al alloy nanoparticles by plasma arc discharge. *Thin Solid Films*, 519(1):81–85, 2010.

[90] Y. Lee, J-R. Choi, K. J. Lee, N. E. Stott, and D. Kim. Large-scale synthesis of copper nanoparticles by chemically controlled reduction for applications of inkjet-printed electronics. *Nanotechnology*, 19(41):415604, 2008.

[91] U. Leonhardt. Optical metamaterials: Invisibility cup. *Nature Photonics*, 1(4):207–208, 2007.

[92] L. Li, D.-R Chen, and P.-J Tsai. Use of an electrical aerosol detector (ead) for nanoparticle size distribution measurement. *Journal of Nanoparticle Research*, 11(1):111–120, 2009.

[93] J.-W. Lim, M.-S. Kim, N. R. Munirathnam, M.-T. Le, M. Uchikoshi, K. Mimura, M. Isshiki, H.-C. Kwon, and G.-S. Choi. Effect of ar/ar-h2 plasma arc melting on cu purification. *Mater Trans (MATERIALS TRANSACTIONS)*, 49(8):1826–1829, 2008.

[94] B. Y. H. Liu and D. Y. H. Pui. Electrical neutralization of aerosols. *Journal of Aerosol Science*, 5(5):465–472, 1974.

[95] B. Y. H. Liu, K. T. Whitby, and D. Y. H. Pui. A portable electrical analyzer for size distribution measurement of submicron aerosols. *Journal of the Air Pollution Control Association*, 24(11):1067–1072, 1974.

[96] M. S. Liu, Lin, Mark C. C., C. Y. Tsai, and C. C. Wang. Enhancement of thermal conductivity with cu for nanofluids using chemical reduction method. *International Journal of Heat and Mass Transfer*, 49(17-18):3028–3033, 2006.

[97] X. Luo, A. Morrin, A. J. Killard, and M. R. Smyth. Application of nanoparticles in electrochemical sensors and biosensors. *Electroanalysis*, 18(4):319–326, 2006.

[98] J. Lyyränen, J. Jokiniemi, E. I. Kauppinen, U. Backman, and H. Vesala. Comparison of different dilution methods for measuring diesel particle emissions. *Aerosol Science and Technology*, 38(1):12–23, 2004.

[99] J. Ma, T. H. Fletcher, and B. W. Webb. Thermophoretic sampling of coal-derived soot particles during devolatilization. *Energy & Fuels*, 9(5):802–808, 1995.

[100] E. Mack, G.G. Osterhof, Kraner, and H.M. Vapor pressure of copper oxide and of copper. *J Am Chem Soc*, (45):617–623, 1923.

[101] W. Mahoney and Andres R.P. Aerosol synthesis of nanoscale clusters using atmospheric arc evaporation. *Materials Science and Engineering A*, 204(1-2):160–164, 1995.

[102] W. Mahoney, Andres R.P., and M.D Kempe. Aerosol synthesis of metal and metal oxide, nitride and carbide nanoparticles using arc evaporation source. *MRS Proceedings*, 400:65–70, 1996.

[103] M. M. Maricq and N. Xu. The effective density and fractal dimension of soot particles from premixed flames and motor vehicle exhaust. *Journal of Aerosol Science*, 35(10):1251–1274, 2004.

[104] D. Mariotti and R. M. Sankaran. Microplasmas for nanomaterials synthesis. *Journal of Physics D: Applied Physics*, 43(32):323001, 2010.

[105] M. Marjamäki, J. Keskinen, D.-R Chen, and D. Y. H. Pui. Performance evaluation of the electrical low-pressure impactor (elpi). *Journal of Aerosol Science*, 31(2):249–261, 2000.

[106] M. Marjamaki, A. Virtanen, M. Moisio, and J. Keskinen. Modification of electrical low pressure impactor for particles below 30 nm. *Journal of Aerosol Science*, 30(1):393–394, 1999.

[107] P. H. McMurry. A review of atmospheric aerosol measurements. *Atmospheric Environment*, 34(12-14):1959–1999, 2000.

[108] M. Meseth, P. Ziolkowski, G. Schierning, R. Theissmann, N. Petermann, H. Wiggers, N. Benson, and R. Schmechel. The realization of a pn-diode using only silicon nanoparticles. *Scripta Materialia*, 67(3):265–268, 2012.

[109] B. Mewes and J. M. Seitzman. Soot volume fraction and particle size measurements with laser-induced incandescence. *Applied Optics*, 36(3):709, 1997.

[110] P. Migowski and J. Dupont. Catalytic applications of metal nanoparticles in imidazolium ionic liquids. *Chemistry - A European Journal*, 13(1):32–39, 2007.

[111] S. M. Moghimi. Nanomedicine: current status and future prospects. *The FASEB Journal*, 19(3):311–330, 2005.

[112] M. Mohseni, B. Ramezanzadeh, H. Yari, and M. Moazzami. The role of nanotechnology in automotive industries. In *New Advances in Vehicular Technology*, volume Carmo (Hg.) 2012.

[113] R.J Munz, T. Addona, and A.C da Cruz. Application of transferred arcs to the production of nanoparticles. *Pure and Applied Chemistry*, 71:1889–1897, 1999.

[114] A. B. Murphy. Demixing in free-burning arcs. *Physical Review E - Statistical Physics, Plasmas, Fluids, and Related Interdisciplinary Topics*, 55(6B):7473–7494, 1996.

[115] A. B. Murphy. The effects of metal vapour in arc welding. *Journal of Physics D: Applied Physics*, 43(43):434001, 2010.

[116] A. B. Murphy, M. Tanaka, S. Tashiro, T. Sato, and J. J. Lowke. A computational investigation of the effectiveness of different shielding gas mixtures for arc welding. *Journal of Physics D: Applied Physics*, 42(11):115205, 2009.

[117] K. Nakaso, M. Shimada, K. Okuyama, and K. Deppert. Evaluation of the change in the morphology of gold nanoparticles during sintering. *Journal of Aerosol Science*, 33(7):1061–1074, 2002.

[118] K. Norrman, A. Ghanbari-Siahkali, and N. B. Larsen. 6 studies of spin-coated polymer films. *Annual Reports Section C*, 101:174, 2005.

[119] B. K. Park, D. Kim, S. Jeong, J. Moon, and J. S. Kim. Direct writing of copper conductive patterns by ink-jet printing. *Thin Solid Films*, 515(19):7706–7711, 2007.

[120] H. Patashnick and E. G. Rupprecht. Continuous pm-10 measurements using the tapered element oscillating microbalance. *Journal of the Air and Waste Management Association*, 41(8):1079–1083, 1991.

[121] N. Petermann, N. Stein, G. Schierning, R. Theissmann, B. Stoib, M. S. Brandt, C. Hecht, C. Schulz, and H. Wiggers. Plasma synthesis of nanostructures for improved thermoelectric properties. *Journal of Physics D: Applied Physics*, 44(17):174034, 2011.

[122] V.V. Petrov. *Announcements on galvano-voltaic experiments, Con ducted by the Professor of Physics Vasilii Petrov, Located at St. Petersburg's Medical and Surgical Academy (in Russian)*. St. Petersburg, 1803.

[123] E. Pfender. Thermal plasma technology: Where do we stand and where are we going? *Plasma Chemistry and Plasma Processing*, 19(1):1–31, 1999.

[124] F. R. Quant, R. C. Flagan, and K. D. Horton. Implementation of a scanning mobility particle sizer (smps). *Journal of Aerosol Science*, 24(1):83–84, 1995.

[125] M. N. Rahaman. *Ceramic processing and sintering*, volume 23 of *Materials engineering*. M. Dekker, New York, 2. edition, 2003.

[126] M. Rai, A. Yadav, and A. Gade. Silver nanoparticles as a new generation of antimicrobials. *Biotechnology Advances*, 27(1):76–83, 2009.

[127] Y.P Raizer. *Gas discharge physics*. Springer, Berlin, 1997.

[128] M. A. Ramírez-Argáez, C. González-Rivera, and G. Trápaga. Mathematical modeling of high intensity electric arcs burning in different atmospheres. *ISIJ International*, 49(6):796–803, 2009.

[129] J. Ristimäki, A. Virtanen, M. Marjamäki, A. Rostedt, and J. Keskinen. On-line measurement of size distribution and effective density of submicron aerosol particles. *Journal of Aerosol Science*, 33(11):1541–1557, 2002.

[130] A. Rostedt, M. Marjamäki, and J. Keskinen. Modification of the elpi to measure mean particle effective density in real-time. *Journal of Aerosol Science*, 40(9):823–831, 2009.

[131] C. Roth, G. A. Ferron, E. Karg, B. Lentner, G. Schumann, S. Takenaka, and J. Heyder. Generation of ultrafine particles by spark discharging. *Aerosol Science and Technology*, 38(3):228–235, 2004.

[132] P. Roth and A.V. Filippov. In situ ultrafine particle sizing by a combination of pulsed laser heatup and particle thermal emission. *Journal of Aerosol Science*, 27(1):95–104, 1996.

[133] M. Rouenhoff. *Synthesis of monodisperse FePt Nanoparticles by Pulsed Laser Ablation.* PhD thesis, Universität Duisburg-Essen, Duisburg, 31.10.2013.

[134] E. Ruppecht, M. Meyer, and H. Patashnick. The tapered element oscillating microbalance as a tool for measuring ambient particulate concentrations in real time. *Journal of Aerosol Science*, 23(1):635–638, 1992.

[135] J. J. Schauer, W. F. Rogge, L. M. Hildemann, M. A. Mazurek, G. R. Cass, and B. R.T. Simoneit. Source apportionment of airborne particulate matter using organic compounds as tracers. *Atmospheric Environment*, 30(22):3837–3855, 1996.

[136] H.-J. Schmid, Belal A.-Z., C. A., and W. Peukert. Evolution of the fractal dimension for simultaneous coagulation and sintering. *Chemical Engineering Science*, 61(1):293–305, 2006.

[137] C. Schulz, B.F. Kock, M. Hofmann, H. Michelsen, S. Will, B. Bougie, R. Suntz, and G. Smallwood. Laser-induced incandescence: recent trends and current questions. *Applied Physics B*, 83(3):333–354, 2006.

[138] A. Schutze, J.Y Jeong, S.E Babayan, Jaeyoung Park, G.S Selwyn, and R.F Hicks. The atmospheric-pressure plasma jet: a review and comparison to other plasma sources. *IEEE Transactions on Plasma Science*, 26(6):1685–1694, 1998.

[139] M. Seipenbusch, A. P. Weber, A. Schiel, and G. Kasper. Influence of the gas atmosphere on restructuring and sintering kinetics of nickel and platinum aerosol nanoparticle agglomerates. *Journal of Aerosol Science*, 34(12):1699–1709, 2003.

[140] J.-H. Seo and B.-G. Hong. Thermal plasma synthesis of nano-sized powders. *Nucl Eng Technol (Nuclear Engineering and Technology)*, 44(1):9–20, 2012.

[141] S. Sharma, M.-P. Macht, and V. Naundorf. Impurity-diffusion investigations in amorphous ti60ni40. *Physical Review B*, 49(10):6655–6666, 1994.

[142] M.-G Shin and D.-W Park. Synthesis of copper nanopowders by transferred arc and non-transferred arc plasma systems. *Journal of Optoelectronics and Advanced Materials*, 12(3):528–534, 2010.

[143] T. A. Sipkens, R. Mansmann, K. J. Daun, N. Petermann, J. T. Titantah, M. Karttunen, H. Wiggers, T. Dreier, and C. Schulz. In situ nanoparticle size measurements of gas-borne silicon nanoparticles by time-resolved laser-induced incandescence. *Applied Physics B*, 116(3):623–636, 2014.

[144] C. M. Sorensen. The mobility of fractal aggregates: A review. *Aerosol Science and Technology*, 45(7):765–779, 2011.

[145] M. Stein, D. Kiesler, and F. E. Kruis. Adjustment and online determination of primary particle size in transferred arc synthesis of copper nanoparticles. *Aerosol Science and Technology*, 47(11):1276–1284, 2013.

[146] M. Stein, D. Kiesler, and F. E. Kruis. Effect of carrier gas composition on transferred arc metal nanoparticle synthesis. *Journal of Nanoparticle Research*, 15(1), 2013.

[147] M. R. Stolzenburg and P. H. McMurry. An ultrafine aerosol condensation nucleus counter. *Aerosol Science and Technology*, 14(1):48–65, 1991.

[148] N. S. Tabrizi, M. Ullmann, V. A. Vons, U. Lafont, and A. Schmidt-Ott. Generation of nanoparticles by spark discharge. *Journal of Nanoparticle Research*, 11(2):315–332, 2009.

[149] K. Tanaka, K. Ishizaki, S. Yumoto, T. Egashira, and M. Uda. Production of ultra-fine silicon powder by the arc plasma method. *Journal of Materials Science*, 22(6):2192–2198, 1987.

[150] X.-F. Tang, Z.-G. Yang, and W.-J. Wang. A simple way of preparing high-concentration and high-purity nano copper colloid for conductive ink in inkjet printing technology. *Colloids and Surfaces A: Physicochemical and Engineering Aspects*, 360(1-3):99–104, 2010.

[151] C. Tendero, C. Tixier, P. Tristant, J. Desmaison, and P. Leprince. Atmospheric pressure plasmas: A review. *SPECTROCHIM ACTA B (Spectrochimica Acta Part B: Atomic Spectroscopy)*, 61(1):2–30, 2006.

[152] M. Uda, S. Ohno, and T. Hoshi. Process for production fine metal particles. patentnumber 4376740.

[153] Van der Wal, R. L., T. M. Ticich, and A. Brock Stephens. Can soot primary particle size be determined using laser-induced incandescence? *Combustion and Flame*, 116(1-2):291–296, 1999.

[154] C. van Gulijk, J. C. M. Marijnissen, M. Makkee, J. A. Moulijn, and A. Schmidt-Ott. Measuring diesel soot with a scanning mobility particle sizer and an electrical low-pressure impactor: Performance assessment

with a model for fractal-like agglomerates. *Journal of Aerosol Science*, 35(5):633–655, 2004.

[155] A. Virtanen, J. Ristimäki, and J. Keskinen. Method for measuring effective density and fractal dimension of aerosol agglomerates. *Aerosol Science and Technology*, 38(5):437–446, 2004.

[156] D. Vollath. Plasma synthesis of nanopowders. *Journal of Nanoparticle Research*, 10(S1):39–57, 2008.

[157] L. Waldmann and K.H. Schmitt. Thermophoresis and diffusiophoresis of aerosol. In *Aerosol Science, Academic Press, London*, pages 163–194.

[158] J. C. F. Wang, B. F. Kee, D. W. Linkins, and R. W. Lynch. Real-time total mass analysis of particulate in the stack of an industrial power plant. *Journal of the Air Pollution Control Association*, 33(12):1172–1176, 1983.

[159] S. C. Wang and R. C. Flagan. Scanning electrical mobility spectrometer. *Aerosol Science and Technology*, 13(2):230–240, 1990.

[160] R.C. Weast. *CRC Handbook of Chemistry and Physics*. CRC Press, Boca Raton, 2. edition, 1980.

[161] A. P. Weber, M. Seipenbusch, and G. Kasper. Application of aerosol techniques to study the catalytic formation of methane on gasborne nickel nanoparticles. *The Journal of Physical Chemistry A*, 105(39):8958–8963, 2001.

[162] K. Wegner, B. Schimmöller, B. Thiebaut, C. Fernandez, and T. N. Rao. Pilot plants for industrial nanoparticle production by flame spray pyrolysis. *KONA Powder and Particle Journal*, 29(0):251–265, 2011.

[163] Z. Wei, T. Xia, J. Ma, J. Dai, W. Feng, Q. Wang, and P. Yan. Growth mechanism of cu nanopowders prepared by anodic arc plasma. *Transactions of Nonferrous Metals Society of China (English Edition)*, 16:168–172, 2006.

[164] K. T. Whitby and W.E Clark. Electrical aerosol particle counting and size distribution measuring system for the 0.015 to 1.0 microm size range. *Tellus*, (13):573–586, 1966.

[165] A. Wiedensohler and H. J. Fissan. Aerosol charging in high purity gases. *Journal of Aerosol Science*, 19(7):867–870, 1988.

[166] K. Willeke. Temperature dependence of particle slip in a gaseous medium. *Journal of Aerosol Science*, 7(5):381–387, 1976.

[167] T. Witten and L. Sander. Diffusion-limited aggregation, a kinetic critical phenomenon. *Physical Review Letters*, 47(19):1400–1403, 1981.

[168] K. Woo, C. Bae, Y. Jeong, D. Kim, and J. Moon. Inkjet-printed cu source/drain electrodes for solution-deposited thin film transistors. *Journal of Materials Chemistry*, 20(19):3877, 2010.

List of Figures

List of Tables

Appendix A

Abbreviations

Acronym

BET	Brunauer-Emmett-Teller
CD	Crucible design
CFD	Computational fluid dynamics
CPC	Condensation particle counter
DMA	Differential mobility analyzer
DMPS	Differential mobility particle sizer
EDX	Energy-dispersive X-ray spectroscopy
ELPI	Electrical low pressure impactor
ESP	Electrostatic precipitator
ICP-MS	Inductively coupled plasma mass spectrometry
LII	Light induced incandescence
LTE	Local thermal equilibrium
mOSU	Multiple optimal single unit (8 OSUs)
OSU	Optimal single unit for nanoparticle production by transferred arc
PR	Production rate
Re	Reynolds number
SEC	Specific electricity consumption

SEM	Scanning electron microscopy
SMPS	Scanning mobility particle sizer
SSA	Specific surface area
TEOM	Tapered element oscillating microbalance
TEM	Transmission electron microscopy
TIG	Tungsten inert gas welding
XRD	X-ray diffraction

Abbreviations

a	Particle surface are (m^2)
a_f	Particle surface of fully sintered spherical particle (m^2)
a_m	Area of one adsorbed gas molecule (BET) (m^2)
c	Pre-exponential sintering parameter (s/Km^3or s/Km^4)
C_C	Cunningham slip correction factor
C_d	Drag coefficient
d	Diameter (m)
d_a	Aerodynamic diameter (m)
d_e	Equivalent diameter (m)
d_{hkl}	Spacing between diffracting planes (XRD) (m)
d_m	Equivalent mobility diameter (m)
d_p	Particle diameter (m)
d_s	Stokes diameter (m)
D_f	Fractal dimension of an agglomerate
D_{fm}	Mass mobility exponent
E	Electric field (V/m)
E_a	Activation energy for sintering (J/mol)
E_{ch}	Charging efficiency of particle d_m(A m^3)

f	Frequency (1/s)
F_{d}	Drag force (N)
F_{e}	Electric field force (N)
g	Thickness of one filtration layer (m)
$\triangle\, G$	Change of free energy (J)
$\triangle\, G_{\mathrm{v}}$	Change of free energy due to the formation of new volume (J)
$\triangle\, G_{\mathrm{s}}$	Change of free energy due to the formation of new surface (J)
h	Constant relating to the heat of adsorption and condensation (BET)
I	Nucleation rate ($1/\mathrm{m}^3\mathrm{s}$)
I_i	Measured current of the i-th impactor stage (ELPI) (A)
k	Boltzmann constant (J/K)
l	Diameter of the nozzle (ELPI) (m)
l_{s}	Sampling distance from center (Thermophoretic sampling) (m)
l_{f}	Film thickness (m)
m	Mass or mass load (kg)
m_{aggl}	Agglomerate mass (kg)
M_{m}	Molar mass (kg/mol)
n_1	Monomer concentration (m^{-3})
n_i	Number of atoms in a formed nucleus
n_{p}	Number of primary particles in an agglomerate
N	Particle number concentration (m^{-3})
p_1	Partial pressure of condensing species (Pa)
p_{d}	Equilibrium vapor pressure above a drop of diameter d_P (Pa)
p_{s}	Saturation vapor pressure (Pa)
$\triangle\, p$	Pressure drop (Pa)
P	Penetration factor for particle filtration
P_0	Vapor pressure of the adsorbate gas (BET) (Pa)

P_e	Equilibrium experimental pressure (BET) (Pa)
Q_1	Main carrier gas flow (l/min)
Q_2	Quench carrier gas flow (l/min)
r	Radius of a formed cluster (m)
r_n^*	Critical cluster radius (m)
R	Gas constant (J/mol K)
R_f	Resistance (Ω)
S	Supersaturation
Stk	Stokes number
t	Time (s)
T	Temperature (K)
v	Particle volume (m^3)
V_0	Volume of the adsorbed gas per gram of adsorbant (BET) (m^3)
$V_{0\mathrm{m}}$	Volume of the adsorbate monolayer per gram adsorbent (BET) (m^3)
V_m	Molar volume (m^3/mol)
W	Dilution factor
x	Velocity of a sphere or particle (m/s)
x_c	Average velocity of the carrier gas (ELPI) (m/s)
x_t	Settling velocity of a sphere (m/s)
x_th	Thermophoretic velocity (m/s)
X	Dynamic shape factor
Z_p	Electrical mobility (m^2/Vs)
α_s	Sampling angle (Thermophoretic sampling) (°)
β	Collision frequency (m^3/s)
λ	Mean free path (m)
γ	Fraction of particles that are collected in one filter layer (%)

η	Gas viscosity (Pa s)
ρ_{b}	Bulk density (kg/m^3)
ρ_{g}	Gas density (kg/m^3)
ρ_{p}	Particle density (kg/m^3)
σ	Surface tension (J/m^2)
τ_{s}	Characteristic sintering time (s)
θ_{hkl}	Incident angle (XRD) ($^\circ$)

Appendix B

Technical drawings

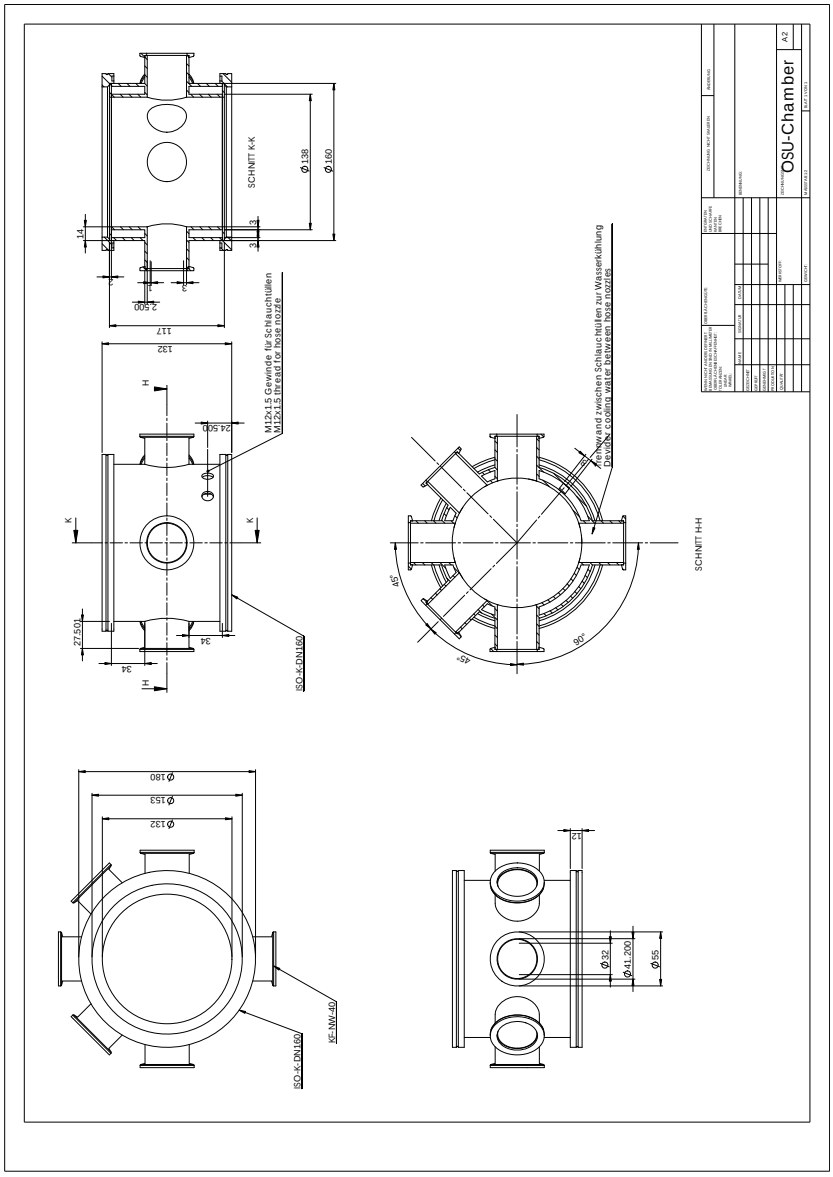

Figure B.1: *Technical drawing of the OSU housing*

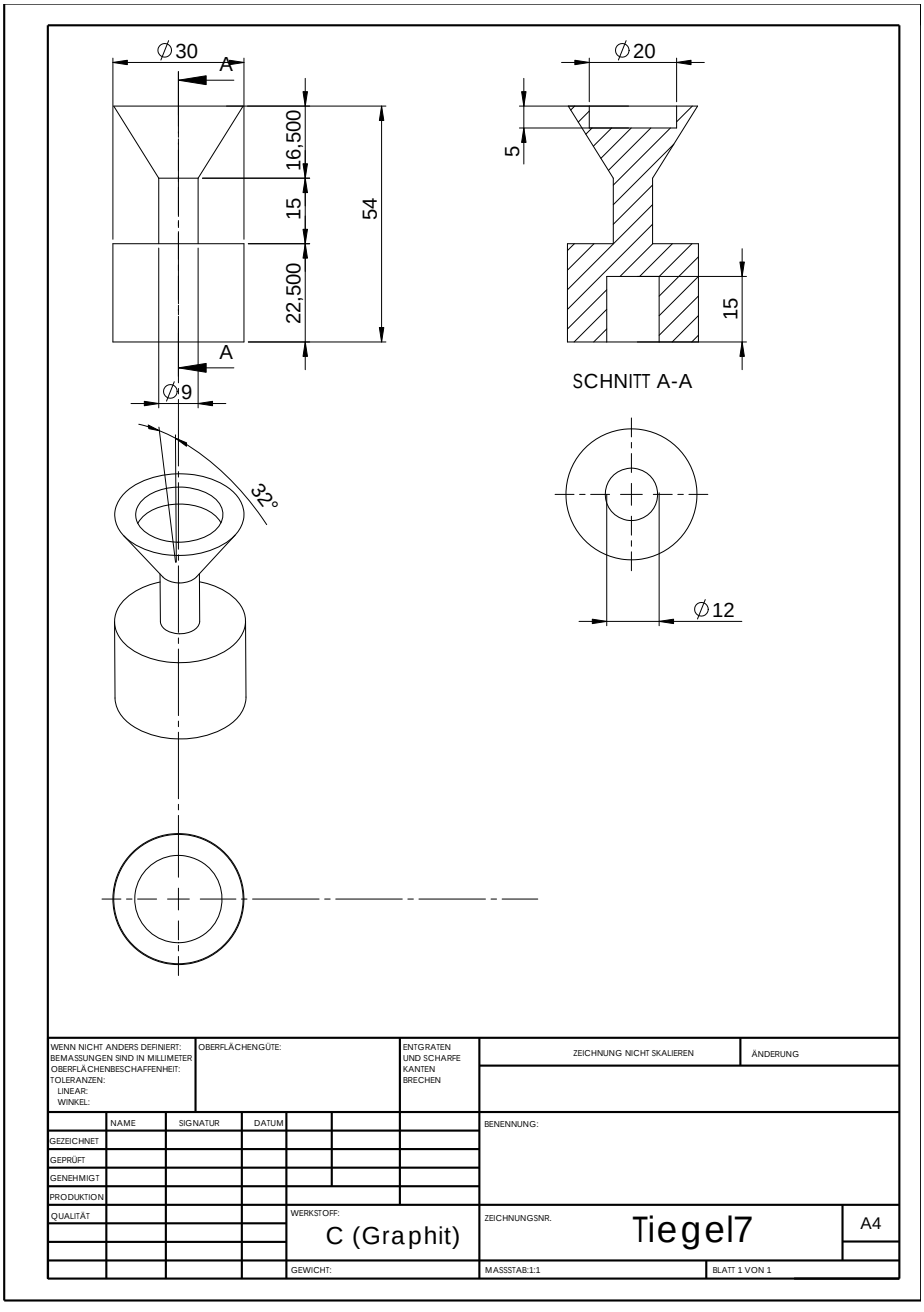

Figure B.2: *Technical drawing of the crucible*

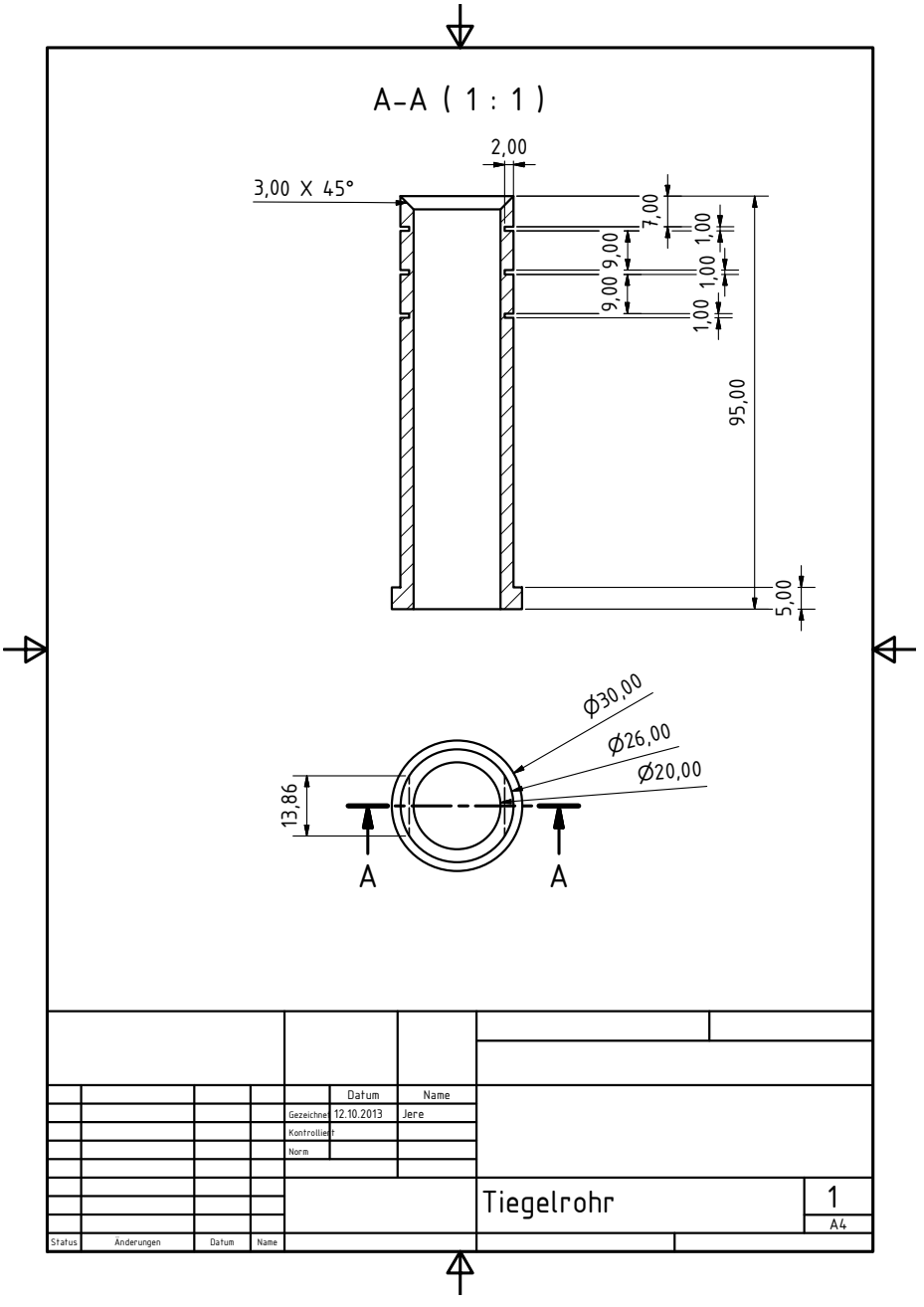

Figure B.3: *Technical drawing of the crucible pipe*

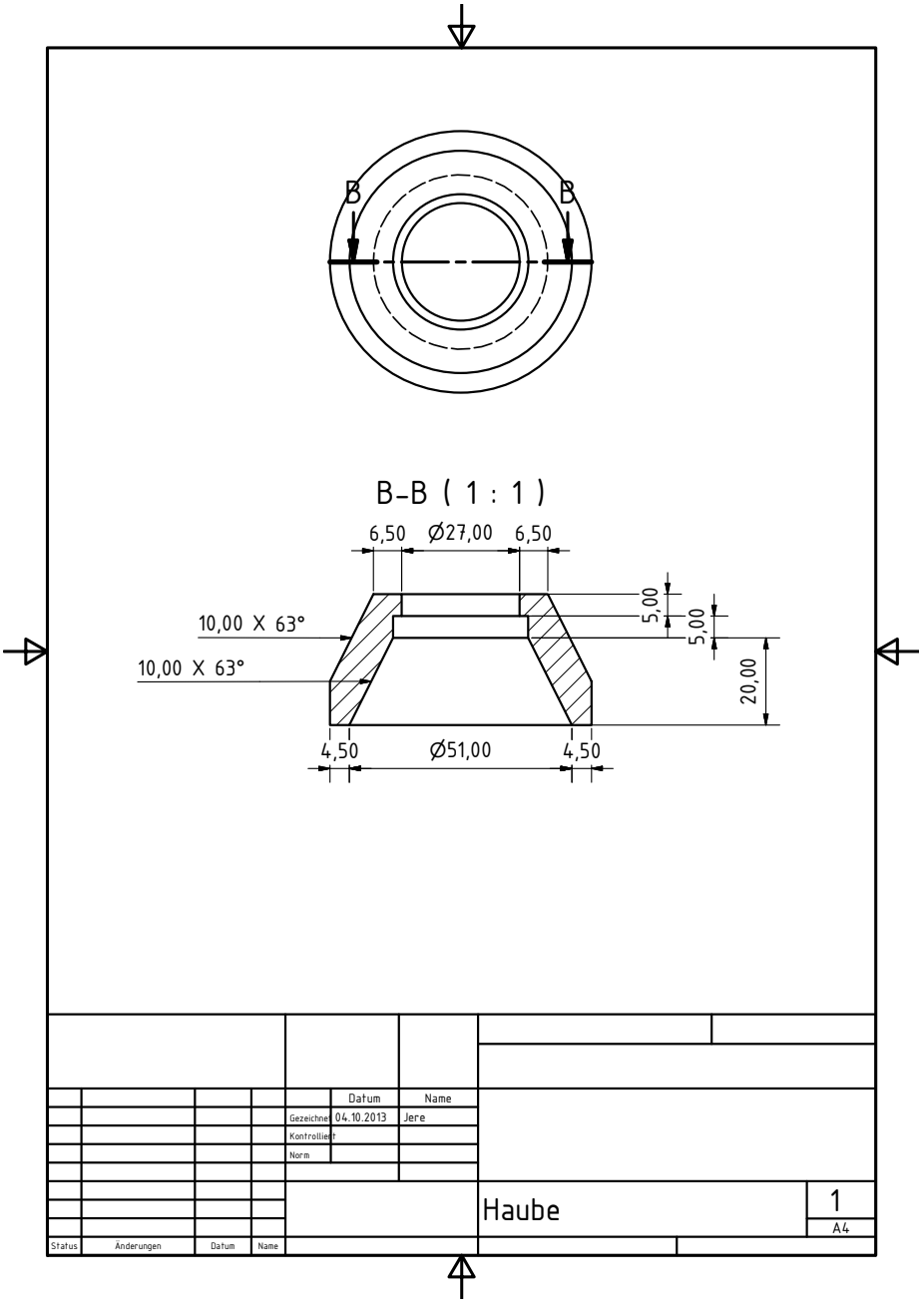

Figure B.4: *Technical drawing of the crucible hood*

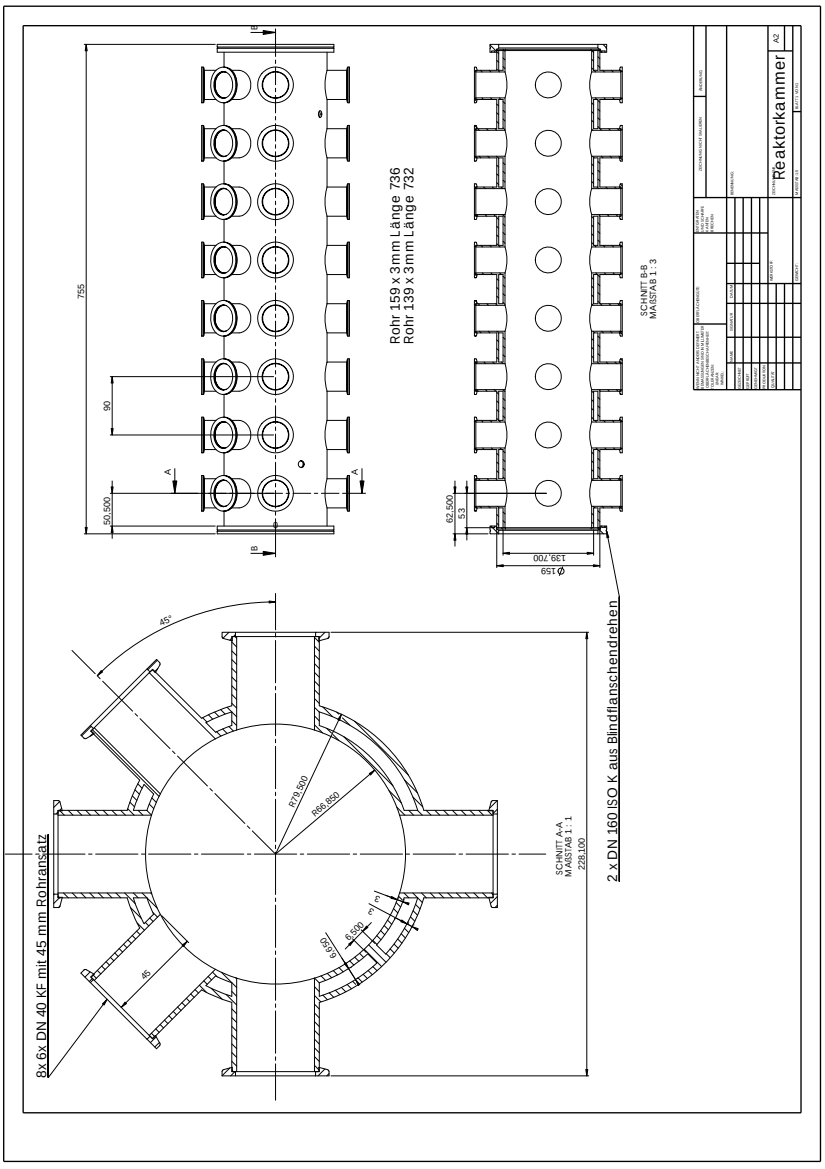

Figure B.5: *Technical drawing of the mOSU reactor housing*

Appendix C

Curriculum Vitae

Matthias Stein was born on April 5th, 1986 in Mülheim an der Ruhr, Germany.

1999-2005 Completion of Secondary School (German Abitur), Luisenschule Gymnasium an den Buchen, Mülheim an der Ruhr, Germany

2006-2009 Bachelor of Science (B.Sc.) majoring in Nanoengineering, University of Duisburg - Essen, Germany. During the study program he collaborated in a bachelor project with the company Federal Mogul Corp. with the goal of improving the tribological characteristics of surfaces by the addition of gas-phase produced TiC particles. In his bachelor thesis he investigated the performance of an aerodynamic lens system for high flow rates.

2009-2011 Master of Science (M.Sc.) majoring in Nanoengineering, University of Duisburg - Essen, Germany. Focusing on Nano-Process-Technology, he visited the University of Minnesota in Minneapolis in order to investigate the effects of electrode position and hydrogen gas flow on silicon nanocrystals for photovoltaic purposes. His master thesis was a feasibility study of in-flight nanorod formation in the Au-SiH_4 system to form silicon nanorods in the gas-phase.

2012 VDE Award 2012, awarded for an excellent diploma (M.Sc.) and Master thesis.

2011-2015 Scientific Assistant (conferral of a doctorate), University of Duisburg - Essen, Germany.

Appendix D

Publications

Part of the work described in this thesis also appear in:

Filed Patent:

- M. Stein, J. Geiss, F.E. Kruis (2014) Lichtbogenreaktor und Verfahren zur Herstellung von Nanopartikeln. German patent number 102014220817-3

Publications:

- M. Stein, D. Kiesler, F.E. Kruis (2013) Effect of carrier gas composition on transferred arc metal nanoparticle synthesis. *Journal of Nanoparticle Research* 15:1400
- M. Stein, D. Kiesler, F.E. Kruis (2013) Adjustment and online determination of primary particle size in transferred arc synthesis of copper nanoparticles. *Aerosol Science and Technology* 47:1276-1284
- E. Hontanon , J.M. Palomares, M. Stein , X. Guo, R. Engeln, H. Nirschl, F.E. Kruis (2013) The transition from spark to arc discharge and its implications with respect to nanoparticle production. *Journal of Nanoparticle Research* 15:1957
- Parts of chapter 5 and 7 will be submitted separately

Conference contributions:

- M. Stein, M. Rouenhoff, D. Kiesler, F.E. Kruis (2012) Up-scaling Metal Nanoparticle Production by Means of Arc Discharge. High-Tech Plasma Processes 2012, Bologna, Italy.

- M. Stein, F.E. Kruis (2012) Scaling-up of metal nanoparticle synthesis by means of multiple arc discharge. PARTEC 2012, Nürnberg, Germany.
- M. Stein, D. Kiesler, F.E. Kruis (2013) Adjustment and online determination of primary particle size in transferred arc synthesis. AICHE 2013, San Francisco, USA.
- M. Stein (2014) Development of an arc discharge process for metal nanoparticle synthesis. BUONAPART-E Summerschool, Valencia, Spain
- M. Stein, F.E. Kruis (2014) Scale-up and online validation of metal nanoparticle production. MRS Fall Meeting 2014, Boston, USA
- M. Stein, F.E. Kruis (2015) Scale-up of metal nanoparticle production. Nanotech 2015, Washington DC, USA.
- M. Stein, F.E. Kruis (2015) Hoch-skalierte Produktionsanlage zur Herstellung metallischer Nanopartikel. 29. Palas ATS, Karlsruhe, Deutschland.